Navigation for UAVs Using Signals of Opportunity

By

Masud Al Aziz

Submitted to the graduate degree program in Department of Electrical Engineering and Computer Science and the Graduate Faculty of the University of Kansas in partial fulfillment of the requirements for the degree of Doctor of Philosophy

Committee members

Dr. Christopher Allen, Chairperson

Dr. Shannon Blunt

Dr. Rongqing Hui

Dr. Heechul Yun

Dr. Shawn Keshmiri

Date defended: December 4th, 2015

The Dissertation Committee for Masud Al Aziz certifies
that this is the approved version of the following dissertation :

Navigation for UAVs Using Signals of Opportunity

Dr. Christopher Allen, Chairperson

Date approved: _____

Abstract

The reliance of Unmanned Aerial Vehicles (UAVs) on Global Navigation Satellite System (GNSS) for autonomous operation represents a significant vulnerability to their reliable and secure operation due to signal interference, both incidental (e.g. terrain shadowing, ionospheric scintillation) and malicious (e.g. jamming, spoofing). An accurate and reliable alternative UAV navigation system is proposed that exploits Signals of Opportunity (SOP) thus offering superior signal strength and spatial diversity compared to satellite signals. Given prior knowledge of the transmitter's position and signal characteristics, the proposed technique utilizes triangulation to estimate the receiver's position. Dual antenna interferometry provides the received signals' Angle of Arrival (AoA) required for triangulation. Reliance on precise knowledge of the antenna system's orientation is removed by combining AoAs from different transmitters to obtain a differential Angles of Arrival (dAoAs). Analysis, simulation, and ground-based experimental techniques are used to characterize system performance; a path to miniaturized system integration is also presented. Results from these ground-based experiments show that when the received signal-to-noise ratio (SNR) is above about 45 dB (typically in within 30 km of the transmitters), the proposed method estimates the receiver's position uncertainty range from less than 20 m to about 60 m with an update rate of 10 Hz.

Acknowledgements

I would like to thank my Advisor, Dr. Christopher Allen for guiding me through the whole process. I would also like to thank my honorable committee members for their valuable guidance. Finally, I would like to thank my parents and my wife for supporting me during the whole period.

Contents

List of Figures

List of Tables

Chapter 1

Introduction

1.1 Overview

The Unmanned Aerial Vehicle (UAV) is becoming popular for various military and non-military activities, such as policing, traffic monitoring, surveillance of pipelines, salvage operations, border patroling, and fire-fighting ([1]-[3]). Moreover, the UAVs are being employed in various research fields that are hazardous for manned aerial vehicle, such as remote sensing of ice sheets in remote places of arctic and antarctica ([4]-[5]). UAVs are also being engaged in various military applications, such as Intelligence, Surveillance, Reconnaissance (ISR), and combat operations ([6]-[7]).

Satellite-based navigation, such as Global Positioning System (GPS) has been widely used for navigation of UAVs. GPS is a navigation system that receives signals from the satellites to estimate the position of the receiver. The signals contain timing and ranging information that are used to calculate the receiver's position. However, the strength of the received satellite signal is low due to attenuation through space for long period of time. Moreover, the signals from satellites are susceptible to detrimental interferences, such as jamming and spoofing. The interferences can result in aborting the mission or even hijacking of the UAVs ([8]-[9]).

In this dissertation, a Navigation Via Signals of Opportunity (NAVSOP) technique has been proposed for the navigation of UAVs. Signals of Opportunity (SOP) are signals that are transmitted for purposes other than navigation [10]. SOP includes AM band signals, FM band signals, NTSC television broadcasting signals, and wireless communication signals etc. SOP signals are advantageous over satellite signals in terms of Received Signal Strength (RSS) and indoor availability. However, SOPs do not contain timing information. Therefore, this dissertation proposes a triangulation technique to estimate position of the receiver based on the Angle of Arrival (AoA) of the incoming signals from transmitters at known positions. The triangulation technique for position estimate has been applied in celestial tracking [11]. While the accuracy of celestial technique is coarse due to the large distance between observer and the celestial object, useful position accuracies can be obtained by exploiting SOPs from regional transmitters. Moreover, the triangulation technique in [11] requires accurate knowledge about the position of the receiver with respect to absolute north. The dissertation proposes a differential AoA (dAoA) technique to remove the dependency of accurate knowledge of the receiver's heading with respect to absolute north. Therefore, the proposed technique does not depend on heading knowledge that reduces cost and inaccuracy. First, the navigation system measures AoAs from 2 spatially separated transmitters at known positions. The AoAs are referenced to the receiving antenna system geometry whose orientation is unknown relative to the position of the transmitters. Therefore, a differential Angle of Arrival (dAoA) concept is used to remove the reference of the orientation of the antenna system. Applying triangulation with the known positions of the two transmitters and the dAoA leads to the formation of a circle of possible receiver positions. To appropriately pinpoint the receiver's position from the loci of points, another circle is formed from another pair of spatially different transmitters. The intersection of the two circles determines the position of the receiver.

A prototype of the system is demonstrated using the FM band (88 MHz- 108 MHz) signals. This dissertation proposes an accurate, low-cost, reliable, and easy to implement navigation system for UAVs as a backup to GPS system. The position accuracy of the GPS is between 3 meters and 5

meters with an update rate of 10 Hz. The accuracy and update rate of the proposed navigation system should be comparable. Moreover, the received satellite signal strength is low and thus GPS signal can be subjected to spoofing and jamming. The proposed system is based on SOP where the received signal strength is high. Therefore, the system is less prone to spoofing and jamming compared to GPS.

1.2 Scope

The proposed concept is simple and robust and thus is appropriate for other applications, such as indoor and underground navigation where signals from satellite is unavailable, navigation using signals other than RF beacons (e.g. optical or acoustic beacons), or navigation in meadia where RF signal propagation is not possible (e.g. underwater, ice, or sand etc.). The received signal strength from satellite is extremely low or unavailable inside buildings (arenas, office spaces, warehouses, hospitals, hangers, and homes etc.) and underground (e.g. caves, mines, bunkers, and tunnels etc.) and thus GPS navigation is not an option. In these situations, purpose-built fixed frequecny narrowband (or Continuous Wave - CW) beacons can be installed at known positions to serve as navigation aids. The operating space can be coupled with 3-D definitions and thus enabling efficient navigation inside the space. In absence of 3-D definitions of the operating space, other sensors, such as Google's Project Tango Tablet can be installed on the platform and thus can enable exploration and discovery of the spaces that have been equipped with these beacons.

The beacons could be simple RF transmitters (operating in an ISM - Industrial, Scientific, and Medical band), existing WiFi nodes, or optical emitters, such as Light Emitting Diodes (LEDs) that are distinctive based on the color of emitted light (visible or infrared), polarization (e.g. linear vertical, right-handed circular), or on the nature of an applied modulation (e.g. on/off modulation at a subcarrier frequency in the Hz or kHz). Alternatively, acoustic signals (e.g. from purpose-built fixed frequency narrowband ultrasonic emitters) can be used instead of electromagnetic signals

(e.g. RF, microwave, optical) in which case, an array of acoustic transducers (e.g. microphones) replace the receive antenna array. Operation in the accoustic realm requires knowledge of propagation velocity of the medium (something that the system can measure in situ).

Migration from the use of RF signals to acoustic or optical signals expands the potential operating class to include underwater operation (including freshwater or seawater), thus enabling precise underwater navigation derived from installed purpose-built fixed-frequency acoustic emitters. Moreover, operations in other media, such as mud, sand, ice, or living tissue is possible with the proposed concept.

1.3 Organization

This dissertation is organized as follows. Chapter 2 presents a brief literature review of the navigation techniques applied for UAV navigation. The theory, working principle of the proposed system, and simulation results are described in Chapters 3 and 4. Measurement results will be provided in chapter 5. Chapter 6 will conclude the dissertation and comment on the scope of future work.

Chapter 2

Literature review

In this section, a brief overview of different navigation techniques for UAVs is presented. Various methods have been proposed for the navigation of UAVs, such as Long Range Navigation (LORAN) [12], Inertial Navigation System (INS) ([19]-[27]), Global Positioning System (GPS) ([28]-[32]), a fusion of INS/GPS system ([33]-[56]), vision-aided navigation system ([57]-[74]), and Navigation Via Signals of Opportunities (NAVSOP) ([80], [83]-[84]). In general, the navigation techniques are divided into two categories, such as active navigation and passive navigation. The active navigation system works on two-way communications, i.e. both the transmitter and the receiver transmit as well as receive the signals. On the contrary, the passive navigation system receives the signal from the transmitter but the receiver does not transmit any signal. Thus passive navigation system consumes less power and can maintain covert position. The timing and ranging information is not required in the case of having accurate knowledge about positions of the transmitters. The passive navigation system includes GPS, NAVSOP, and INS etc. The active system is not used in cases where the receiver position must be kept secret, such as in military covert operation. However, the active navigation system is simpler to implement in terms of compuational loads and thus is more suitable for public services, such as policing and fire-fighting.

Based on the navigation technique, the navigation systems can be further divided into two cat-

egories, such as incremental systems and absolute systems. In the incremental navigation system, such as INS, the initial position of the receiver is a known priori and then the receiver position is updated based on the intial position, elapsed time, and incremental displacements of the receiver. The accuracy of the position estimate is a function of the initial position, accuracy and precision of the incremental displacements. On the other side, the absolute navigation system, such as GPS tracks the receiver position without any prior knowledge. Therefore, the absolute navigation system is more suitable than an incremental navigation system that anticipates a partial service interruption.

The goal of this chapter is to present a brief overview of the traditional navigation systems that are used for navigation of UAVs.

2.1 LORAN

The Long Range Navigation (LORAN) is a hyperbolic navigation system that determines the position of the receiver by receiving radio signals from fixed position radio beacons [12]. A LORAN system includes land-based facilities, receiver, and appropriate charts. The land-based facility consists of a chain of three or more land-based transmitting sections that are separated by hundreds of miles. All of the transmitters operate on the same frequency of 100 kHz [12]. One of the transmitters is called the master station whereas, the other transmitters are denoted as secondary stations. The master and the secondary stations transmit signals at precise time intervals. The receiver measures the time difference that the signal takes from a master-slave pair to arrive at the receiver. The time difference is a measure of the range between the master-slave pair transmitters and the receiver. The locus of points that have the same time difference from a master-slave transmitting pairs constitute a hyperbola. The intersection of three or more hyperbolas determine the position of the receiver. However, the absolute accuracy of the LORAN system is between 185 meters to 463 meters [12]. Therefore, LORAN does not meet the required accuracy of this project.

2.2 Celestial tracking

Celestial navigation estimates the position of the receiver by observing identified stars, identified planets, the sun, and the moon [13]. Celestial navigation is widely used to determine the latitude and longitude of a ship vessel at a specific time through the use of observations of altitudes of celestial bodies [14]. Distant stars are the sources of electromagnetic radiation and thus provide the opportunity to obtain position estimate of a receiver. The position of the receiver is determined by observing distant stars with a sextant, star charts, and a chronometer [15]. The chart-based approach, developed in the last century by Sumner and St.-Hilaire, translates each celestial altitude observation into a line of position (LOP) on the surface of the Earth. In principle, a series of observations defines a group of intersecting LOPs and this intersection represents the position of the observer. The celestial object is tracked by a telescope and the telescope must be pointed to the star accurately. However, a telescope is not portable in a compact system and a precise measurement setup is necessary to obtain an accurate position estimate. Moreover, the method is applicable at night with a clear sky. Therefore, celestial navigation tracking is suitable for position estimate of base stations that will be utilized as LORAN or other base stations.

2.3 Object tracking

The object tracking algorithm is an incremental navigation system that detects an object in successive images [15]. The method requires knowledge about the initital position of the receiver and updates the receiver's change in position in time. The position estimate is updated in real-time from features in the image, such as points, straight edges, and ellipses using a 3-D model of the object [16]. Moreover, the algorithm does not require object identification. However, the system needs accurate calibration that is hard to achieve and time consuming.

2.4 Satellite tracking

In satellite tracking based navigation system, the geolocation information of the receiver is obtained by tracking a satellite using a telescope for absolute navigation [17]. The satellite navigation system works on optical visibility of the satellite with the telescope and does not require satellite transmission. However, both object and satellite tracking systems are dependent on the visibility and thus are not suitable for all-weather conditions.

2.5 Gravimetry

The gravimetry method is an absolute navigation system. In this system, the position of the receiver is estimated by measuring the local gravity and then compare with a database of highly accurate gravitional corrections [17]. However, gravimetry equipment is not portable in a compact system, such as in a GPS. Besides, the accuracy of the technique is too coarse.

2.6 Public-service SAR

A public-service Systhetic Aperture Radar (SAR) provides conventional SAR imaging as well as broadband communication and geo-location services [18]. The receiver is equipped with antennas that communicate with the SAR. The receiver requests the SAR with an ID in a coded message and the SAR provides the geolocation of the receiver. The SAR possess an accurate pre-recorded map of the scene around the receiver and thus provides an accurate location of the receiver on the pre-stored map. However, the accuracy of the navigation system depends on the number of requests received from the receivers and a higher number of requests results in lower accuracy.

2.7 INS

The INS employs accelerometers for measuring the acceleration and gyroscopes to measure the angular rotation of the UAV ([19]-[23]). The accelerometer measures the acceleration of the UAV along an axis. Integrating the acceleration provides the velocity of the UAV. Moreover, integrating the acceleration twice provides the change of position of the UAV along the axis. Therefore, the current position of the UAV is deduced from prior knowledge of direction of flight and initial position of the UAV. Moreover, the gyroscope provides an output proportional to the angle of rotation that the UAV experiences [19]. Besides, the INS navigation system requires knowledge of initial position and orientation of the UAV. The information is provided by a GPS and a magnetometer. A magnetometer is a sensor that is employed to find the magnetic north[20]. However, the earth's magnetic field is influenced by external sources and misalignment of magnetometer due to the earth's weak magnetic field strength. A novel magnetometer calibration technique was utilized to counter this issue by rotating the receiver from magnetic east to west along three axes [21]. Thus, the receiver gets exposed to maximum and minimum magnetic field amplitudes. The bias term is then calculated from this maximum and minimum magnetic field amplitudes and is used to correct the magnetometer readings.

The INS based navigation system comprises of three modules, such as an attitude estimator, a position and velocity estimator, and a mission management module [22]. The attitude estimator calculates the angular velocity of the UAV. The position and velocity estimator calculates the acceleration and position of the UAV. The autonomous navigation is performed in the mission management unit based on pre-programmed mission data. The core of the INS is called the Inertial Measurement Unit (IMU). The INS can determine position, orientation, and angular velocity from the IMU readings and elapsed time. However, INS sensors have a bias accumulation during the integration of the acceleration process and this leads to error accumulation over time [23]. The error in position estimate can go from 0.01 m to higher than 0.25 m in 10 seconds of operation [24]. Therefore, the measurement accuracy of the INS sensors becomes coarser over time.

Besides, INS with a low bias drift and a high accuracy is expensive and robust [25]. Therefore, Micro Electro-Mechanical System (MEMS) technology has been exploited to make compact INS system for mobile and handheld systems [26]. Additionally, MEMS INS is low-cost, reliable, and consumes low power compared to the traditional INS [27].

2.8 GPS

Satellite navigation system is low-cost and more accurate than INS [28]. Independent satellite systems have been developed by various countries, such as Global Positioning System (GPS) by USA, Galileo by Europe, Global Navigation Satellite System (GLONASS) by Russia, BeiDou Navigation Satellite System (BDS) by China, Doppler Orbitography and Radio (DORIS) by France, Indian Regional Navigation Satellite System (IRNSS) by India, and Quazi Zenith Satellite System (QZSS) by Japan. All of the satellite systems are collectively known as Global Navigation Satellite System (GNSS) [29]. The GPS navigation system utilizes the concept of Time-Of-Arrival (TOA) ranging to determine the position of the user [30]. In this system, each satellite is equipped with a clock that is synchronized with other satellites in the constellation. Each satellite transmits a ranging signal with a particular code and contains accurate timing information about the time of signal transmission [31]. The positioning system is based on one-way ranging technique. The timing information is retrieved from the signal in the receiver and then scaled by the speed of light to calculate the distance between the transmitter and the receiver as shown in the Equation (2.1),

$$D = ct \tag{2.1}$$

where D is the distance between the transmitter and the receiver, c is the speed of light in air, and t is the time difference between transmitting and receiving of the signal. Each pair of satellite-receiver position constitutes a sphere with the range equal to the distance between the transmitter and the receiver. The receiver receives additional signals from two other satellites and thus constitutes 3 spheres that are intersecting each other. The intersection point of all of the 3 spheres

determines the position of the receiver. The basic concept of the GPS is shown in Fig. 2.1.

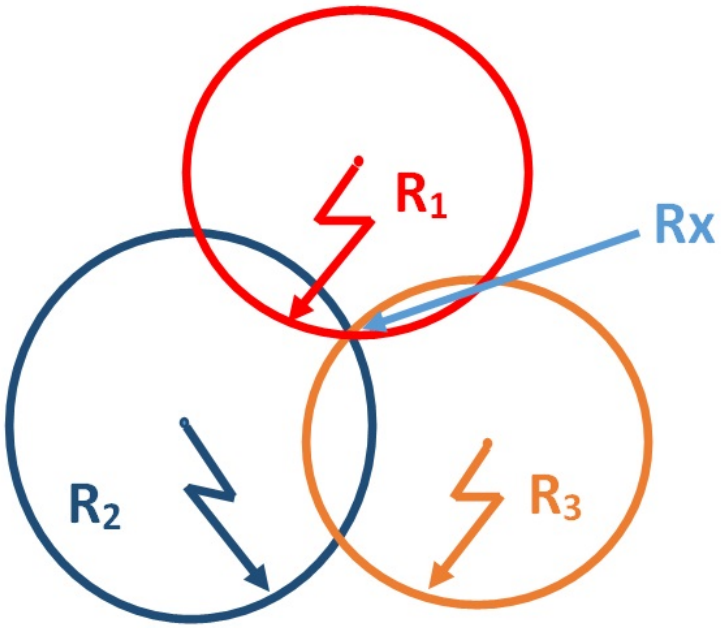

Figure 2.1: GPS working principle (reproduced from [26]).

It is assumed that both of the receiver and the satellite clocks are synchronized and thus 3 spheres provide accurate position estimate. However, the receiver clock and the satellite clocks are not synchronized accurately and thus it introduces an ambiguity in the position estimate. Therefore, the receiver receives a fourth signal from another satellite and thus provides itself 4 spheres to estimate the position of the receiver. The inclusion of the fourth satellite signal removes the receiver's clock dependency and the ambiguity. The receiver then generates non-closed form equations to solve the intersection point of the 4 spheres and the intersection point is the receiver position [32].

2.9 GPS/INS fusion navigation system

GPS/GNSS is a global, all-weather positioning system that is capable of providing three dimensional co-ordinates and time synchronization to Co-ordinated Universal Time (UTC) scale. However, the GPS satellite signal is susceptible to multipath, atmospheric errors, clock drifts, obstacles,

and signal jamming [33]. The satellite signal experiences disturbance in the troposphere and ionosphere and thus results in delay. Moreover, the received signal from the satellite system faces objects on the path and gets reflected. Thus the received signal gets delayed before reaching the receiver. Therefore, there are two signals at the receiver with a time delay and this phenomenon is called multipath. Moreover, a slight error in satellite clock system results in an error of the position estimate due to the long distance between the satellite system and the receiver [34]. Furthermore, the satellite signal experiences difficulty in reaching the receiver in case of bad weather, interferencs, jamming, and spoofing. Spoofing is the phenomenon that occurs when a strong local signal is employed to take control of the navigation of the UAV [35]. Therefore, a fusion of GPS receiver and INS is widely used in the UAV navigation system [36]. The position estimate from the GPS receiver is compared to a pre-stored position of a point on the ground and the difference is used to correct the INS error. The most common method of INS/GPS fusion is the Kalman filter [37]. A Kalman filter is a recursive filter that predicts the unknown variable of a system from noisy environment. The filter works in two stages. In the first stage, a prediction of the current state is produced from the physical model with some uncertainty. Then after the first measurement, the measured data is compared to the predicted data and the predicted data is updated with a weighted average. The Complementary Kalman filter (CKF) is the linear Kalman filter that accepts linear error model and has coarse accuracy. On the other hand, Extended Kalman Filter (EKF) accepts non-linear error model and provides fine accuracy [38]. However, the computational load in the EKF is higher than CKF and thus the estimate of the unknown variable in EKF is more divergent than that of CKF [39].

In the GPS/INS fusion algorithm, the position co-ordinates from the GPS receiver are used to correct the bias accumulation of the INS sensor. An INS algortihm is employed to find the position of the receiver. The position estimate is then compared with the position estimate obtained by GPS. The difference of the two estimates is defined as error and the error is then sent to the INS input to correct the IMU reading [40]. To further improve the INS measurements, a strapdown

algorithm is exercised in GPS/INS fusion system. In this configuration, the sensors are strapped to the UAVs and lightweight digital computers are used as angular rate sensors [41]. The strapdown algorithm computes the INS orientation from the angular rate sensors. The orientation is then utilized to convert measured acceleration into navigation co-ordinate frame. The strapdown algorithm correctly estimates the gravity acceleration and provides more accuracy during the integration process. MEMS based Strapdown Inertial Navigation System (SINS) with GPS fusion was investigated and an attitude updating algorithm was applied with MEMS SINS/GPS fusion [42]. The horizontal positional error was reported to be less than 0.5 m whereas, the attitude error was reported to be less than 1^{O}. A barometer was employed with SINS/GPS fusion and Kalman filter algorithm of GPS/SINS/BARO integration was tested in ([43]-[44]). The horizontal and vertical errors were reported to be less than 1 m and 1.4 m respectively.

The GPS and INS systems are complementary to each other in some aspects. The INS system provides fine accuracy in short term and coarse accuracy in long-term position estimate [45]. Therefore, the accuracy of the INS system is time-dependent and external aid is required for long-term operation. On the contrary, GPS provides accurate position estimate over long-term period and thus the performance of GPS is time-invariant. However, the GPS signal availability is subject to interference, noise, and spoofing. Therefore, a backup navigation system is essential for GPS system. Besides, the INS can provide position estimate, velocity, and angular information of the UAV but the GPS cannot provide angular information. Depending on the requirements of interaction between the INS and GPS, the integration of GPS and INS can be of different types, such as uncoupled integration, Loosely Coupled (LC) integration, Tightly Coupled (TC) integration, and deep/ultra-tight integration [31].

In the uncoupled integration mode, the two systems work independently and provide two different solutions. The GPS data is considered to be more accurate and the information is used to correct the INS data without considering the cause of INS drift. In the case of a GPS outage, the

navigation is provided solely by the INS.

In the LC integration, the raw measurement results obtained by GPS is first processed using a KF block. The INS measurement result is obtained in the IMU block. Then the processed GPS navigation results are combined with INS measurement results using another KF block. The difference between the INS and the GPS measurement results is then used to correct the INS measurement and is fed back to the IMU unit. The LC scheme is shown in Fig. 2.2.

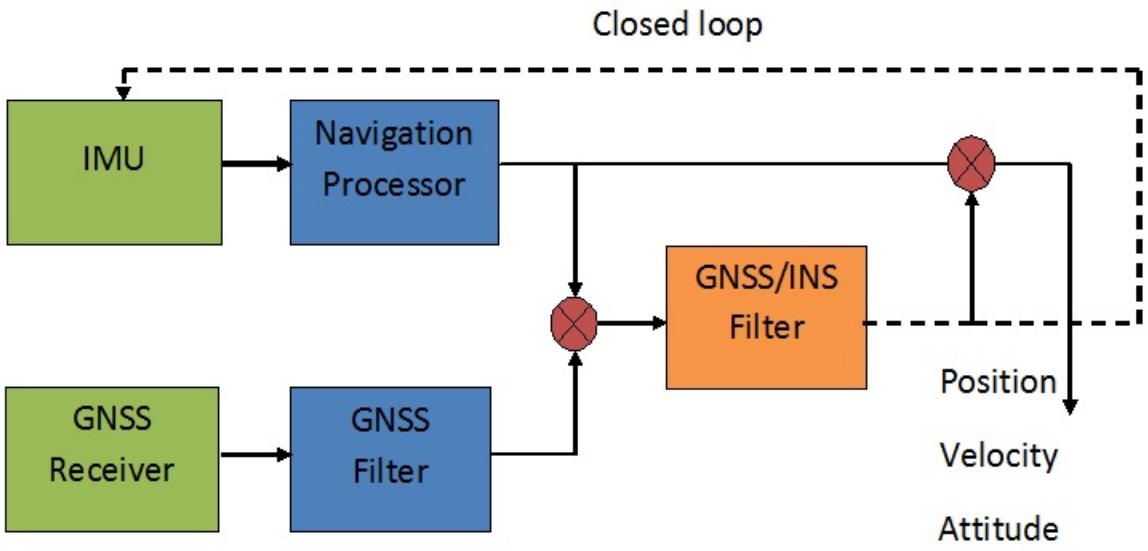

Figure 2.2: Loosely coupled scheme (reproduced from [31]).

The LC scheme, shown in Fig. 2.2, is a closed loop configuration where the estimated INS errors are sent back to the IMU block. Another configuration is the open loop where the INS error is not fed back to the IMU unit. Therefore, the INS errors accrued over time and results in a large error in position estimation. Thus the closed loop configuration is more suitable for INS/GPS integrated system.

In the TC configuration, the GPS raw data is first combined with the INS data. The raw GPS

data is not processed in a KF block as in LC configuration. Instead, the raw GPS data is combined with INS data using a KF block. The TC configuration is shown in Fig. 2.3.

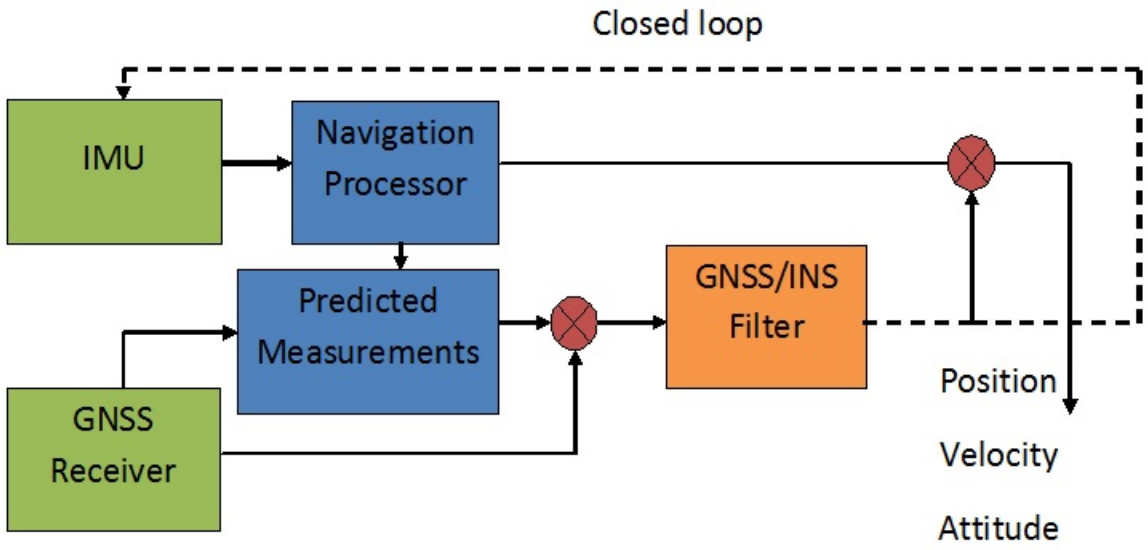

Figure 2.3: Tightly coupled scheme (reproduced from [31]).

In the TC configuration, the raw GPS measurement results are combined with the INS and thus results in a large centralized filter. The LC configuration employs two filters in two stages and yields faster processing time. However, the process noise is added twice in the two filters in LC configuration as opposed to TC configuration where process noise is added once.

The GPS/INS fusion has been studied with an Adaptive Kalman Filter (AKF) algorithm in [46]. The dynamic noise properties of the UAV changes with the UAV motion characteristics and an AKF algorithm models the dynamic noise more accurately than classical Kalman Filter (KF) algorithm. The AKF algorithm firstly attains the definite measurements' variances-covariances and residuals. Then the initial mathematical model is changed with the values and recursive iterative equations of the KF are obtained. Finally, the complexity of the AKF is examined through error analysis of residuals and suitable AKF is chosen [46].

A multi-UAV cooperative positioning technique has been proposed in [47]. The proposed method is based on Delauny triangulation. The technique is applicable to the scenerio of multi-UAV flight path. Three other UAVs are used as reference for the receiver UAV as opposed to the three satellites in the GPS system. The ranging between the UAVs are updated through the wireless network. The location of a UAV in a multi-UAV cooperative environment is calculated from the relative ranges between them at known locations. Moreover, due to the large size, limited accuracy, and satellite visibility requirement of GPS system, a unique triangulation system is proposed in [48]. The proposed system employs both ultra-sound signals and radio freuqnecy signals.

2.10 VHF Omnidirectional Range

VHF Omnidirectional Range (VOR) has been proposed as a backup for the navigation of the UAV [49]. The VOR is a short range radio navigation system that requires fixed ground radio beacons (108 MHz - 117.95 MHz) [50]. A VOR ground station transmits an omni-directional master signal. Moreover, a directional signal is propagated from a phased antenna array that is installed at the ground station. Both the signals are received by the receiver and the phase difference of the two signals is calculated. The angle to the UAV from the base station is determined from the phase difference of the two signals [51]. Various researches have been conducted and resulted in different VOR systems, such as Doppler VOR, precision multilobe VOR, and the precesion Doppler VOR [52]. Besides, different techniques, such as Digital Terrain Systems (DTS) and Terrain Contour Matching (TERCOM) have been proposed for navigation system ([53]-[55]). In DTS system, the receiver records the height information along the flightpath and compares the data with a pre-stored digital map to localize the receiver [53]. The TERCOM system measures the flight terrain profile and compares with a pre-stored digital map to estimate the position [54]. The proposed technique in [55] exploits input image sequence to reconstruct a 3-D terrain map through stereopsis. A Digital Elevation Map (DEM) is pre-stored to the system and the constructed terrain map is matched with

the pre-stored DEM to find the airplane's position. Moreover, the DEM is utilized directly in the observation model of an EKF to localize the UAV position [56]. However, the accuracy of the VOR technology is reported to be 90 m [52]. Therefore, the accuracy of VOR is coarse for navigation of UAVs where finer accuracy is required.

2.11 Vision-aided navigation system

The INS navigation provides accurate position estimate for short-term period. The INS can be combined with a GPS for accurate position estimation that is independent of elapsed time. However, GPS signal is not available for indoor localization. Image aided navigation system has been proposed for indoor navigation where the GPS signal is unavailable. The navigation system exploits the sensor images to navigate. Two main approaches have been proposed for indoor localization, such as creating a network of receivers or emitters placed in known locations and dead-reckoning methods with sensors placed only on person of interest [57]. A light-matching technique has been proposed that utilizes the perceived change in the illumination of indoor lights at known positions [57]. All the light bulb positions are pre-installed on the system irrespective of on/off stage and thus the system does not require any illumination calibration. The initial position of the receiver is a known priori and then the receiver updates the location by getting illuminated from a light bulb at known position. In [58], the UAV body is fixed with three laser beams and the laser is shooting to the ground. Then the laser dots are captured with a camera and a computer vision algorithm. The position of the laser dots provides position estimation and the orientation of the UAV. A navigation system that comprises of IMU, a downlooking mono-camera, and a laser range finder has been proposed in [59]. In this setup, the IMU sensor and vision sensors' measurement is fed to the state estimator block. The result is then fed back to the path plan and sensors to update the position estimate. The laser range finder is employed to path plan. This system reduces computational load and thus eliminates offline post-processing of the data. Moreover, a simple visual navigation system has been proposed that is based on "record and replay". During the record or mapping phase,

the UAV is guided along the path to be traversed later and the navigation algorithm recognizes and tracks the path features in an image from the on-board camera [60]. The map consists of a sequence of straight lines that is characterized by the length. In the replay phase, the starting position of the UAV is a known priori and then the UAV traverses a segment of the path from pre-stored values.

Simultaneous Localization and Mapping (SLAM) technique has been adapted in vision-based navigation system ([61]-[63]). SLAM was originally employed for robots to find its position and the position of other landmarks [63]. SLAM was realized through an EKF that used the range between the robot and the landmark as observation data. However, the DEM provides higher resolution map than SLAM and thus SLAM is suitable in case of DEM unavailability [64]. Moreover, an approach based on a single sensor, such as a monocular camera was proposed in vision-based navigation [65]. The system employs monocular camera, DEM and utilizes general Bayesian tracking approach. Besides, vision-based navigation system has been combined with GPS/INS fusion system for accurate position estimation and detection of obstacles [66]. Unlike DEM and terrain matching, an approach was proposed in [67] that extracts object-level features, such as roads, rivers, villages et al. from real-time aerial imagery with data of Geographic Information System (GIS). Moreover, the proposed method adopts GIS as refence data and thus the storage requirement is low. The possibility of using geo-referenced satellite or aerial images for UAV navigation has been explored in [68] with a potential to provide drift-free navigation solution. Besides, a machine vision-aided navigation method based on image stiching to build real-time ground panaromic image has been proposed in [69]. In the proposed method, Visual C++ is applied to form complete visual/GPS/INS integrated navigation simulation system. A new image matching algorithm that is based on multi-scale segmentation is proposed in [70]. In the proposed method, first stable image objects were extracted that contain valuable statistical information. Next, shape features and curves were extracted followed by similar traiangles. At the end, the real time images were created with the centroids of matched objects.

Vision-aided navigation has been employed to find the UAV height in conjunction to GPS/INS fusion [71]. In the proposed method, an adaptive Kalman filter was designed with GPS/INS/Optic flow integration. Optic flow detects the motion of visual features as a result of rotational or angular movement [72]. The phenomenon measures the relative range of objects by differentiating higher angular motion from closer objects and lower angular motion from distant objects. In ([73]-[74]), a Signal Localization and Mapping (SLAM) technique has been proposed that can create a map of an unknown area and localize its position on the map simultaneously.

Vision-aided navigation system does not provide a stable performance irrespective of weather and visibility. The accuracy of the system depends on the visibility condition and thus excludes itself as a suitable candidate for a standalone navigation system.

2.12 Terestrial positioning and timing system

The concept of a Terestrial Positioning and Timing System (TPTS) has been proposed in [75]. The TPTS provides Position, Navigation, and Timing (PNT) service in the case of a GPS outage. The system is based on Code Division Multiple Access (CDMA) and Time Division Multiple Access (TDMA) signal structure. A TPTS consists of two building blocks, such as ground segment and airborne segment. The ground segment consists of multiple ground stations that are synchronized to each other and equipped with transmission devices. The airborne segment contains omnidirectional antenna and the receiver. The proposed concept of TPTS will require additional ground station setup and thus does not provide a cost-effective solution in the case of a GPS outage. Besides, the position accuracy of the system is 80 m and thus the accuracy of the position estimate is not comparable to GPS [75].

2.13 Received Signal Strength based navigation

The Received Signal Strength (RSS) based navigation is a range-based navigation technique ([76]-[78]). The technique utilizes Received Signal Strength Indicator (RSSI) to estimate the distance to known landmarks. First, the received signal strengths with respect to landmarks at various locations are recorded. Then the location of the receiver is calculated by finding the best fit data of the received signal strengths [77]. The RSS based navigation technique is based on the Friis Transmission equation that is presented by Equation (2.2).

$$P_r = P_t G_t G_r (\frac{\lambda}{4\pi R})^2 \tag{2.2}$$

It is shown in the Equation (2.2) that the received power strength is a function of distance between the emitter and the receiver that can be modeled by a free-space path loss. The free-space path loss must be calibrated to create environment-independent model and this calibration is robust, difficult, and time consuming. The achievable accuracy of this technique is reported to be 1.2 m for 8 - 18 beacons in 100 m^2 [79]. However, the received signal's power decreases with increasing range. A decrease in received signal strength results in a decreased SNR that affects localization accuracy. Therefore, RSS based navigation is not a suitable candidate for UAV navigation.

2.14 Navigation Via Signals of Opportunity

Signals of Opportunity (SOP) are signals that are transmitted from ground-based or space-based transmitters for purposes other than navigation, such as AM/FM radio signals, TV broadcasting signals, and GSM/CDMA/WiFi signals [18]. Navigation Via Signals of Opportunity (NAVSOP) is a navigation technique that exploits SOP and thus eliminates the need for a separate infrastructure for the sole purpose of navigation [80]. Moreover, the SOP provides higher signal strength compared to satellite transmitted signal. Therefore, NAVSOP is more suitable for indoor navigation. However, NAVSOP faces some challenges, such as unsynchronized transmission of signals

from the transmitters, unknown transmit time, and different signal structure for SOP at different frequency bands.

NAVSOP has been proposed as a technique for indoor navigation where the GPS signal is unavailable[80]. Different SOP exploitation techniques have been proposed, such as Time of Arrival (TOA), Time Difference of Arrival (TDOA), and Angle of Arrival (AoA).

2.14.1 Time of Arrival

In the TOA measurement, the time that the signal takes from the source to the receiver is a known priori [81]. The receiver sends a signal to the transmitter and the transmitter responds back to the receiver with a signal. The receiver then calculates the time between sending the signal from the receiver and receiving the response to the receiver. The time represents two way propagation delay between the transmitter and the receiver. Therefore, the elapsed time is halved and this corresponds to the distance between the transmitter and the receiver. Moreover, the processing and response delay of the transmitter and the receiver are calculated and then subtracted from the total time. Then the total elapsed time is multiplicated by the speed of light to find the distance between the transmitter and the receiver. This range calculation results in a circle (2-dimensions) or a sphere (3-dimensions). The procedure is repeated with two more receivers that results in two more circles or spheres. The intersection of the three circles/spheres provide the position of the receiver.

2.14.2 Time Difference of Arrival

The TDOA method calculates the location from hyperbolic positioning [82]. In the TDOA measurement, the time difference is calculated either by the arrival time of two signals at the receiver or by the arrival time of a single signal into two receivers [18]. In the former case, the transmitted signals must be synchronized whereas, in the later case, the bias at the two receivers is a known priori. Different navigation techniques that are based on TDOA are proposed in ([83]-[84]).

Both of the TOA and TDOA methods utilize geometric relationship that is based on distances or distance differences between transmitter and the receiver. Moreover, both the methods calculate distance from the arrival time of a signal at two or more receivers. The SOP transmitters are asynchronized and thus the distance cannot be calculated from the arrival time of two signals at one receiver. The TOA employs the transit time between transmitter and receiver to find distance. On the contrary, the TDOA method calculates location from the differences of the arrival times measured on pairs of transmission paths between the transmitter and the receiver [82]. Both TOA and TDOA work on the time-of-flight (TOF) principle of distance measurement and transit time is multiplicated by the speed of light to find the distance. In TOA, the points of intersection of circles or spheres are determined to estimate the position whereas, in TDOA, the intersection points of hyperbolas or hyperboloids are calculated to determine the position. However, both TOA and TDOA methods require multiple receivers at seperate positions. Therefore, TOA and TDOA are not suitable candidate for UAV navigation using SOP. A navigation technique using SOP without any timing information has been proposed in [85]. The technique has been named as carrier phase measurements. In the carrier phase measurements, the change in phase of the received signal is monitored. The trajectory of the platform is then inferred based on the expected phase behaviour measured by a stationary receiver. However, the carrier phase measurement technique accuracy increases with the increased number of measurements taken from different transmitters. Therefore, the technique is more applicable to relatively stationary objects, such as indoor navigation using smartphone.

2.14.3 Angle of Arrival

The Angle of Arrival (AoA) algorithm employs the phase difference of the received signals at closely spaced antenna elements of an antenna array. The spacing between the antenna elements are kept to be less than $\frac{\lambda}{2}$, where λ is the wavelength corresponding to the free space wave velocity. The spacing of less than $\frac{\lambda}{2}$ restricts the phase difference between the received signals to be less than π and thus eliminates any ambiguity in calculating the AoA of the incoming signal. How-

ever, the accuracy of the position estimate is finer with larger spacing between antenna elements. Therefore, a compromise is made between antenna spacing and accuracy of the position estimate.

AoA finding algorithms are categorized into three main categories, such as conventional spectral-based or quadratic type, subspace spectral-based, and statistical methods ([86]-[90]). The quadratic type algorithms obtain DOA of the incoming signal as location of peaks in the spectrum [88]. The Barlett and Capon's Minimum Variance Distortion Response (MVDR) method are examples of quadratic or conventional spectral-based techniques. The delay-and-sum or Barlett is the simplest AoA finding method that is based on the classical beamforming techniques [86]. However, the delay-and-sum method suffers from poor resolution and cannot resolve two signal sources that are separated by a distance smaller than the beamwidth of the antenna array [86]. Capon's Maximum Likelihood (ML) method solves the MVDR of an antenna array such that it maximizes SNR and improves resolution. ML technique seeks for the parameter values that will most likely produce the observed distribution [87]. The quadratic type algorithms are simple to implement, computationally less extensive than other techniques, and requires low power consumption. However, the beamforming ot quadratic techniques suffer from poor resolutions.

Subspace-based methods, such as MUSIC (Multiple Signal Classification) and ESPIRIT (Estimation of Signal Parameters Via Rotational Invariance Techniques) offer finer resolution. MUSIC is a super-resolution direction finding technique that provides an estimation of the number of signals arrived and their direction of arrival [91]. The MUSIC algorithm decomposes the matrix of the received signals from different directions into two matrices, such as the signal matrix and the noise matrix. However, the MUSIC algorithm requires extensive computation and thus storage requirement is high. On the contrary, ESPIRIT algorithm creates two sub arrays that are derived from original array with a translation invariance structure and then explores the rotational invariance property in the signal subspace [92]. Thus the ESPIRIT does not need extensive search throughout all possible steering vectors. Therefore, computational complexity and storage requirement is less

in ESPIRIT compared to MUSIC [89].

The conventional quadratic antenna array requires a large antenna array and suffers from poor resolution. On the other hand, subspace-based methods employs extensive computational complexity and requires high storage. Therefore, this dissertation proposes an interferometry technique for navigation using SOP. The proposed algorithm requires only two elements antenna array and thus overcomes the limitation of larger antenna array size in conventional quadratic techniques. Moreover, the interferometry technique eliminates the need for extensive computational complexity and thus is preferable than subspace-based techniques. Besides, The proposed AoA finding interferometry algorithm does not require multiple receivers at different locations like TOA or TDOA. The synchronization of the transmitters are not required as in TOA. Besides. all of the discussed navigation techniques require knowledge about the absolute position of the receiver with respect to absolute north. The proposed solution employs differential AoAs to remove the dependency on external devices for accurate knowledge of the receiver position with respect to absolute north. The theory of the proposed navigation system is presented and discussed in the next chapter.

A comparison of the accuracies of different navigation techniques is summarized in the table 2.1.

Table 2.1: Comparison of accuracies of various navigation techniques

Navigation technique	**Accuracy**
LORAN	185 m - 463 m [26]
Celestial navigation	1 nautical mile or 1852 m [14]
Object tracking	30 m - 50 m [93]
Satellite tracking	800 m [94]
Gravimetry	10 m (height accuracy) [95]
Public-service SAR	-
INS	0.01 m to beyond 0.25 m in 10 seconds [24]
GPS	3 m - 5 m [41]
GPS/INS fusion	3 m [36]
Vision aided navigation	1.4 m [43]
VOR	90 m [63]
TPTS	80 m [75]
RSS	1.2 m for 8 - 18 beacons in 100 m^2 [79]
NAVSOP	-

Chapter 3

Theory

3.1 System description

This dissertation proposes a small, light-weight, low-power, and multichannel radio based on Navigation Via Signals of Opportunity (NAVSOP) technique for the navigation of UAVs. SOP includes a variety of signals, such as AM band radio signals, FM band radio signals, TV broadcasting signals, and GSM/CDMA/WiFi signals. The proposed navigation technique receives signals from ground-based commercially-licensed broadcast transmitters and analyzes the signals to estimate the position of the receiver. The FM band radio signals are chosen to be the SOP in this proposed navigation system. FM radio band signals are between 88 MHz and 108 MHz with a 200 kHz separation between the channels. Therefore, different Tx signals in the FM frequency bands can be spectrally isolated. Moreover, for US operations, FCC maintains a public database containing the frequency, transmit power, and transmit tower longitude/latitude information for each broadcaster. Metropolitan areas have many (>10) 'very strong' FM signal sources, such as 17 very strong (80+ dBu) or extremely strong (100+ dBu) signals can be received in the FM band in the Kansas City, Missouri Metropolitan area.

The proposed multichannel radio receiver consists of two modules, such as a sensor module and a

signal processing module. The sensor module is composed of at least two receiver channels that collects radio signals from nearby transmitters. The signal processing module contains a database (an ephemeris of sorts) of transmitter parameters (frequecny, power level, and position of transmitting antennas), and a computing device for signal and data analysis. A brief overview of each of the modules is provided in the next two sections.

3.1.1 Sensor module

The sensor module electrically couples the direction finding system to the RF signal environment [97]. The sensor system is an array of antennas that consists of two or more antenna elements. The spatially separated antenna array elements receive the transmitted signals from the transmitters at known positions. Then the received signal is fed to the signal processing module. Mostly, in an interferometric system, two vertical monopole or dipole antenna elements are used to measure the phase difference of the received signals at the two antenna elements. A vertical monopole or dipole antenna element exhibits an omni-directional pattern in the azimuth plane and thus makes the antenna array equally sensitive to signals arriving from any angles on the azimuth direction. The induced voltage in a matched antenna is given by the Equation (3.1)

$$V(t) = V_m sin(\omega t + \phi) \tag{3.1}$$

where $V(t)$ is the induced voltage in volts at the antenna element, V_m is the instantaneous signal amplitude in volts, ω is the angular transmitting frequency in radian/second, and ϕ is the delay of the transmitted signal in radians. Comparing the two signal voltages at two spatially separated antenna elements results in a phase difference of the two received signals. In this case, the phase of one of the antenna is considered to be the 'reference' with respect to the other one and the antenna is referred as the 'sense antenna'.

In this dissertation, a small, light-weight, and compact system provides real-time position knowl-

edge for navigation of UAVs. This system can augment GPS as a backup (should an outage occur) or validate the GPS position data (to mitigate spoofing attempts). The system receives FM band signals from the broadcasting FM radio towers. The FM radio band spreads from 88 MHz to 108 MHz with a channel separation of 200 kHz. However, the intensity of the signal strength from the radio towers are not equal at any position due to the diversified position of the towers operating at different frequency bands. Therefore, the signals with the highest SNRs are chosen for the AoA calculation.

The sensor module of the proposed navigation system consists of two omnidirectional antennas that receive signals from the available RF band radio transmitters. The receiving antennas and the transmitters are assumed to be at the same elevation. Therefore, the AoA of the received signal is measured in the azimuth plane. The AoA of the received signal is derived from the phase difference of the received signals at two antenna elements separated by a baseline distance. The baseline is a reference for calculating AoA that is based on the geometry of the spatially separated receiving antennas. It should be noted here that the AoA derived from one baseline does not resolve the ambiguity between $(0, \pi)$ and $(0, -\pi)$. Therefore, additional baseline is required to eliminate the ambiguity. However, the different baselines must be non-collinear in order to avoid ambiguity.

3.1.2 Signal processing module

The signal processing module performs signal processing in 3 steps, such as down-conversion, demodulation, and computation. In the down-conversion process, the receiver down-converts and amplifies a Radio-Frequency (RF) signal to an Intermediate Frequency (IF) signal. The demodulator converts the IF signal to a suitable signal required for the computational processors, such as analog to digital conversion.

3.2 Working principle

3.2.1 AoA measurement

Consider the setup shown in Figure 3.1 where two antennas, A and B, are separated by a distance d. Moreover, the FM band broadcast transmitter is assumed to be in the far field of the antennas and thus can be considered as a point source. This assumption allows the received signals to be considered as plane waves.

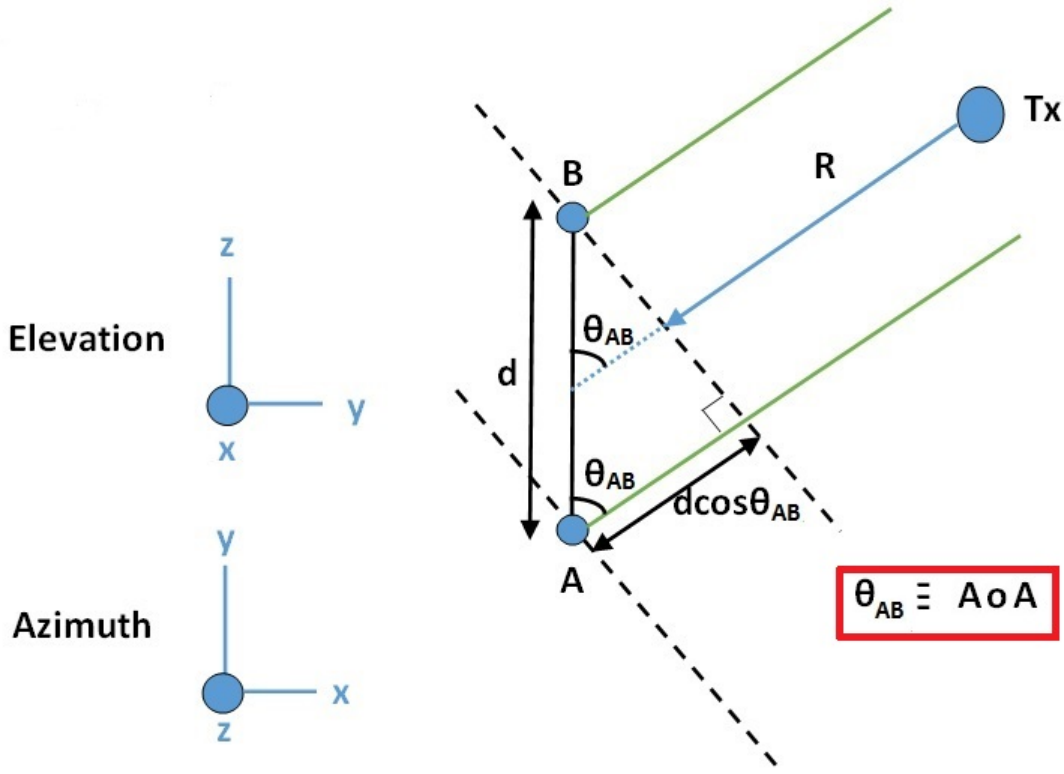

Figure 3.1: Receiving antenna geometry for measuring AoA.

The FM broadcast transmitter is shown as Tx in Fig. 3.1. The received signals at antennas A and B have a phase difference between them. The reason being that the received signal at A travels an additional path $dcos\theta_{AB}$ compared to that of antenna B. Therefore, the phase at antenna A is greater than that of antenna B by the product of $dcos\theta_{AB}$ and wavenumber, k where k is given by Equation

(3.2) and λ is the wavelength at the transmitting frequency.

$$k = \frac{2\pi}{\lambda} \tag{3.2}$$

The relative phases at antennas A and B are assumed to be Φ_A and Φ_B respectively. The phase difference between the two antennas can be found from the Equation (3.3).

$$\Phi_{AB} = kdcos\theta_{AB} \tag{3.3}$$

where θ_{AB} is the AoA of the signal coming from transmitter Tx. Moreover, Φ_{AB} is the phase difference between the received signals at antennas A and B and can be expressed as in Equation (3.4).

$$\Phi_{AB} = \Phi_A - \Phi_B \tag{3.4}$$

Equations (3.2) - (3.4) can be written as

$$\theta_{AB} = cos^{-1}(\frac{\lambda}{2\pi d}\Phi_{AB}) \tag{3.5}$$

It is shown in Equation (3.5) that the AoA of the received signal can be found from the relative phase difference between the two antennas and the wavelength at the transmitting frequency. The spacing between the antenna elements is kept to be less than or equal to $\frac{\lambda}{2}$, where λ is the free space wavelength at the transmitting frequency.

The calculated AoA is exposed to an ambiguity between $(0,\pi)$ and $(0,-\pi)$ as shown in Figure 3.2. It should be noted here that a single baseline measurement is not sufficient to accurately extract the sign of the AoA. Therefore, a second non-collinear baseline is required to eliminate the ambiguity.

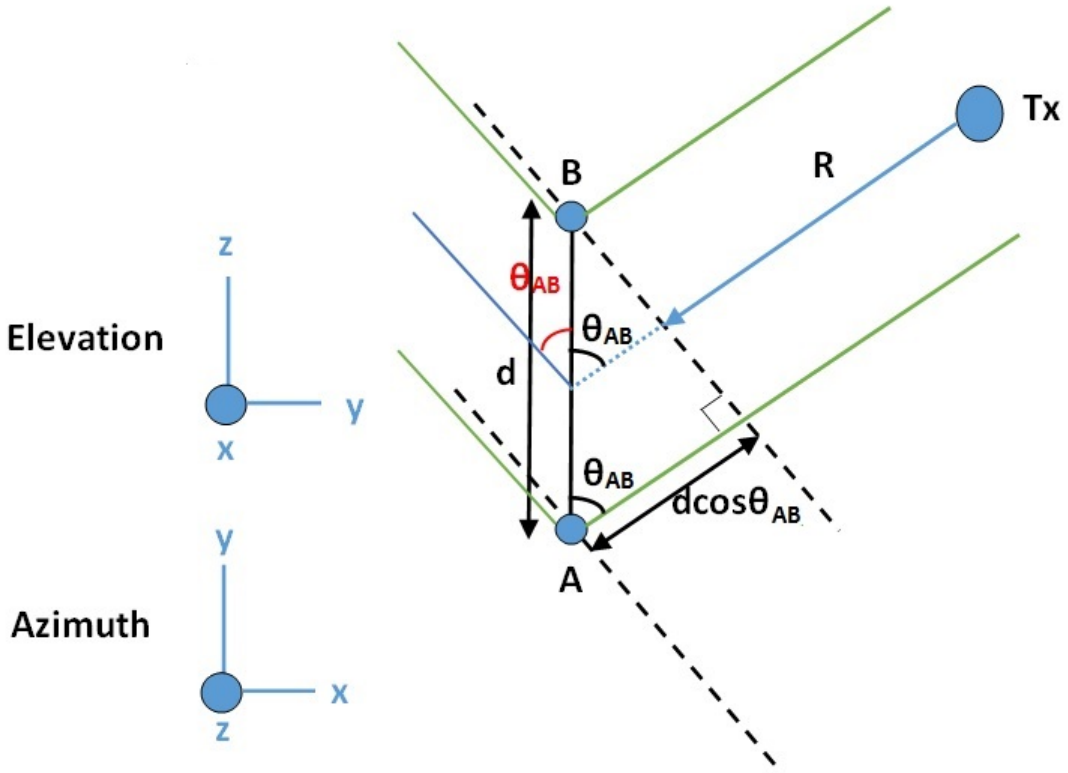

Figure 3.2: Ambiguity of AoA from the receiving antenna baseline.

Figure 3.3 demonstrates the elimination of the AoA ambiguity by two non-collinear baselines. The two baselines are perpendicular to each other over the azimuth. The antennas, *A* and *B*, are considered as baseline I. The baseline I is oriented along the y-axis. The antennas, *A* and *C* are considered as baseline II. Baseline II is oriented along the x-axis.

The AoA of the received signal is measured with a reference baseline. In the Figure 3.3, the reference is the baseline between antennas *A* and *C*. All the AoAs will be calculated with reference to this baseline. The AoA measured by antennas *A* and *C* is denoted as θ_{AC} whereas, the AoA measured by antennas *A* and *B* is denoted as θ_{AB}. It should be noted here that the two AoAs measured by two baselines will have a 90^{o} difference between them due to the perpendicular orientation to each other in the azimuth. Therefore, the ambiguity of AoA between $(0, \pi)$ and $(0, -\pi)$ can be eliminated by the two baselines. In the Figure 3.3, both θ_{AB} and θ_{AC} are between 0^{o}

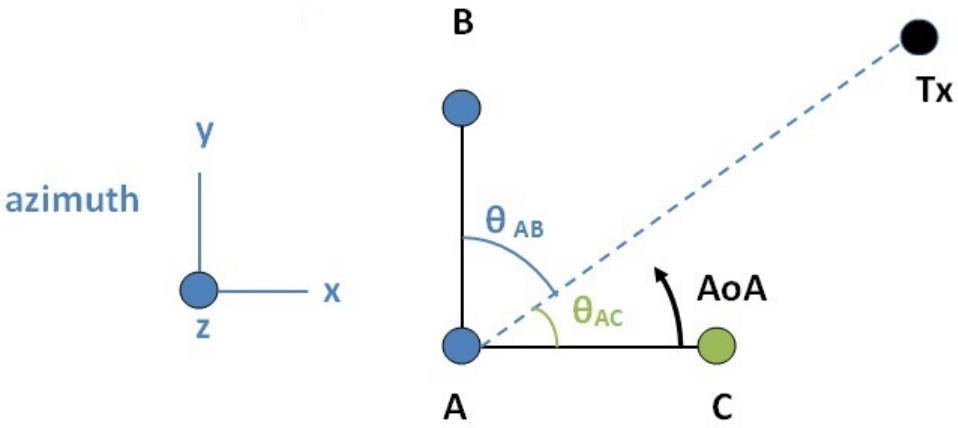

Figure 3.3: The setup of the two antenna baselines to eliminate the AoA ambiguity.

and 90^{o}. The AoA of the received signal is positive for both baselines. However, θ_{AB} and θ_{AC} are separated by 90^{o}. Therefore, θ_{AB} is shifted by 90^{o} to match the baseline of antennas A and C that should be the same as θ_{AC}. In order to achieve finer accuracy in calculating AoA, average value of the θ_{AC} and shifted θ_{AB} is considered to be the AoA of the received signal as shown in Equation (3.6).

$$AoA = \frac{\theta_{AC} + |90^{o} - \theta_{AB}|}{2} \tag{3.6}$$

3.2.2 Triangulation for position estimation

The position of the receiver can be calculated from the AoA measured in the previous section. The proposed navigation system estimates the position of the receiver that is independent of the orientation of the receiver with respect to the transmitters. The use of an external device to calculate the orientation of the receiver with respect to the transmitters coarsens the accuracy of the system. Therefore, the proposed navigation technique provides position estimation that is independent of the orientation of the receiver with respect to the transmitters. This section explains the triangulation technique that is applied to estimate the position of the receiver.

Consider a case of three broadcast transmitters with known positions and a receiver with an unknown position as shown in Figure 3.4.

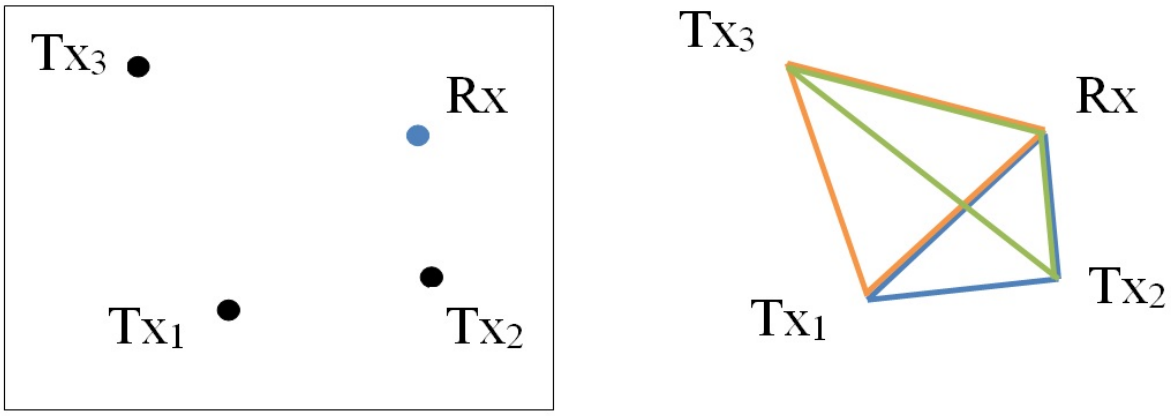

Figure 3.4: Rx and Tx positions.

It is shown in Figure 3.4 that three triangles can be defined with each triangle consists of Rx and one Tx pair. Each triangle can be analyzed with the law of sines as shown in Figure 3.5.

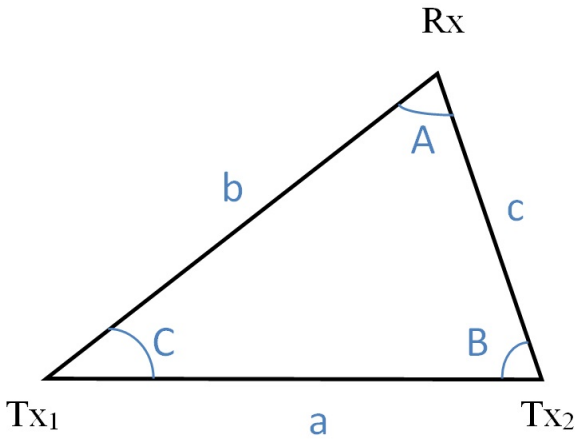

Figure 3.5: A triangle with the Rx and a Tx pair.

Applying law of sines in the triangle of Figure 3.5 leads to the Equation (3.7).

$$\frac{a}{b} = \frac{sinA}{sinB}, \frac{b}{c} = \frac{sinB}{sinC}, \frac{a}{c} = \frac{sinA}{sinC} \tag{3.7}$$

In this dissertation, the Tx positions are assumed to be known. Therefore, the distance between the two known Tx positions, **a**, is assumed to be known. The AoAs from different transmitters are calculated as shown in the previous section and thus the AoAs are known. It should be noted here that the AoAs are referenced to the receiving antenna system geometry whose orientation relative to the Tx position framework is unknown. Therefore, a differential Angle of Arrival (dAoA) is used to remove the reference to the orientation of the antenna system, such as shown in Figure 3.6.

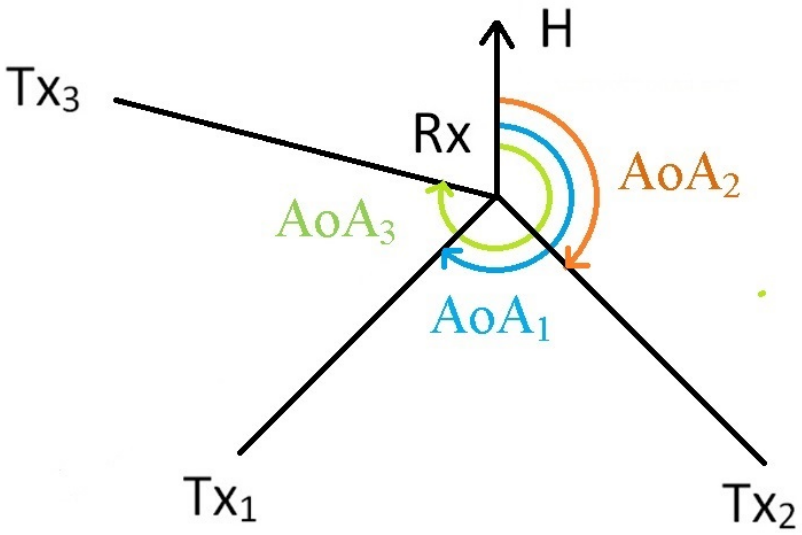

Figure 3.6: AoAs from 3 transmitters measured at the receiver relative to the ref. direction **H**.

The definitions of the dAoAs are shown in Figure 3.7. It can be shown from Figure 3.7 that the dAoAs are found from the following Equations (3.8-3.10).

$$dAoA_{21} = AoA_2 - AoA_1 \tag{3.8}$$

$$dAoA_{32} = AoA_3 - AoA_2 \tag{3.9}$$

$$dAoA_{13} = AoA_1 - AoA_3 \tag{3.10}$$

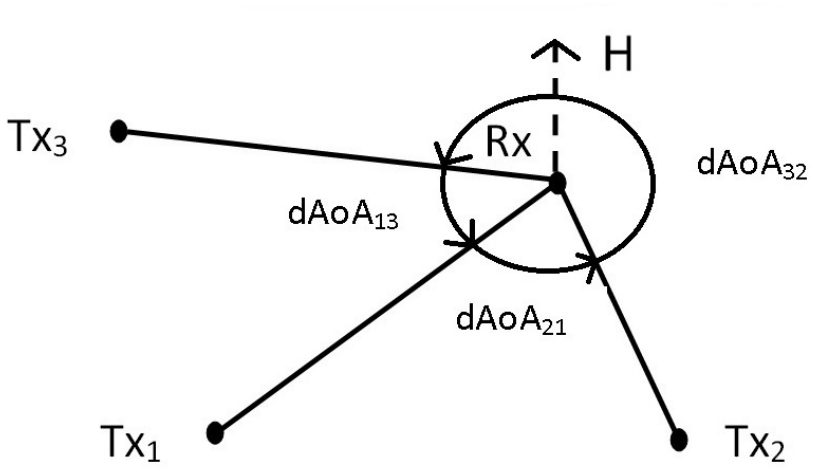

Figure 3.7: The dAoAs between transmitter pairs.

From this set of knowns, a locus of points representing the possible positions of the receivers can be calculated by applying law of sines and triangulation. First assume a series of values for $\angle\mathbf{B}$ ranging from 0^o to 360^o where $\angle\mathbf{B}$ is shown in Figure 3.5. For each assumed value of $\angle\mathbf{B}$, solve for $\angle\mathbf{C}$ such as shown in Equation (3.11).

$$\angle C = 180^o - \angle A - \angle B \tag{3.11}$$

Moreover, solve **b** for each assumed value of $\angle\mathbf{B}$ such as shown in Equation (3.12).

$$b = a\frac{sinB}{sinA} \tag{3.12}$$

The locus of points for the possible position of the receiver takes the form of a circle that passes through the two known Tx positions and the unknown Rx position as shown in Figure 3.8.

Thus the dAoA from one pair of transmitters provide the locus of points that contain the possible position of the receiver. However, in order to localize the position of the receiver from a circle to

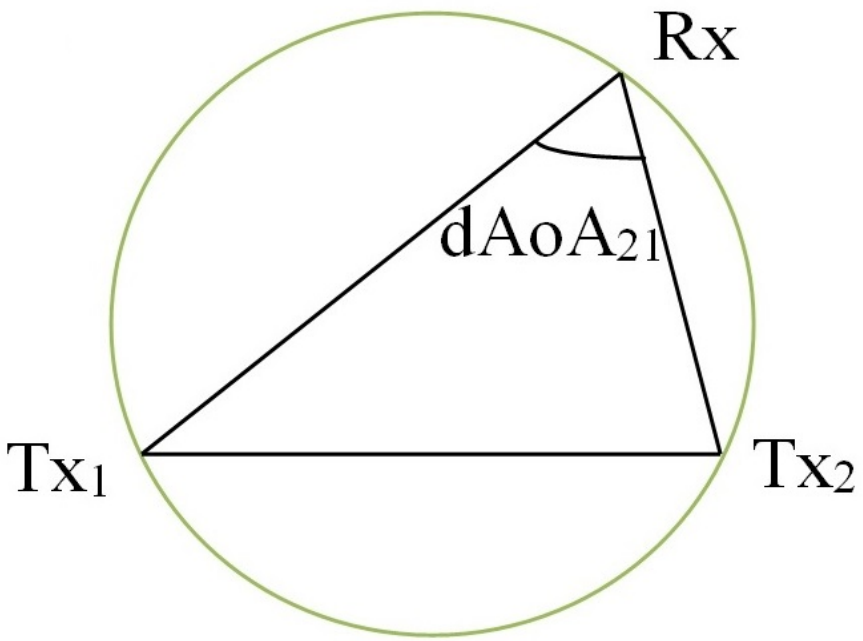

Figure 3.8: Locus of points for possible position of the receiver.

a single point in space, another pair of transmitters, Tx_1 and Tx_3 are required from which $dAoA_{31}$ is found. The Tx pair of Tx_1 and Tx_3 provide another circle that passes through Tx_1, Tx_3, and the Rx. The points of intersection of the two circles coincide with the position of Tx_1 and the Rx as shown in Figure 3.9.

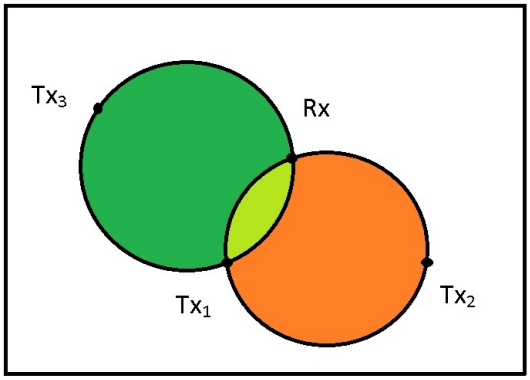

Figure 3.9: Position estimation of the Rx from the intersection of two circles.

The position estimate of the Rx relative to the known Tx positions requires equations describing the circles and solving for the intersections as shown in Figure 3.10.

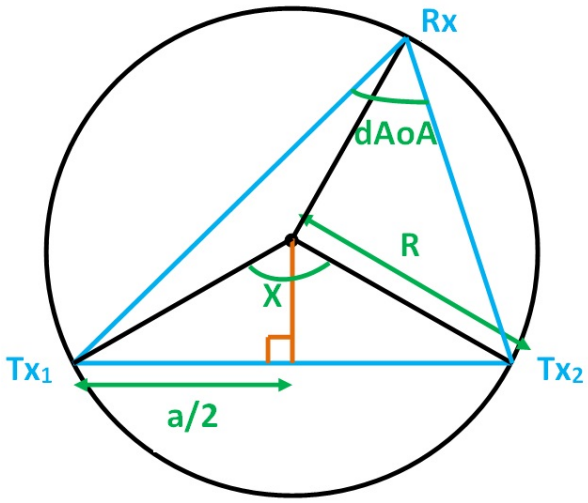

Figure 3.10: Triangulation for position estimation of the Rx.

Assume the radius of the circle is denoted by **R** in Figure 3.10. Moreover, the angle formed at the center of the circle by the Tx pair is assumed to be ∠**X**. The relation between the ∠**X** and ∠**dAoA** can be found from Equation 3.13.

$$\angle X = 2\angle dAoA \tag{3.13}$$

A perpendicular line is drawn from the center of the circle to the baseline of the Tx pair as shown in Figure 3.10 in orange. The line disects both the baseline length **a** and the ∠**X**. Therefore, ∠**X** is related to the baseline length **a** by the Equation (3.14).

$$sin(\frac{X}{2}) = \frac{a}{2R} \tag{3.14}$$

Equations (3.13) and (3.14) can be combined to find the relationship between **R**, **a**, and **dAoA** as shown in Equation 3.15.

$$R = \frac{a}{2sin(dAoA)} \tag{3.15}$$

The center of the circle is found by extending a line segment perpendicular to the midpoint of the

baseline between the Tx pair. A similar circle can be formed by using Tx1, Tx3, and Rx. Then there will be two circles formed by the combination of Tx1, Tx2, Tx3, and Rx as shown in Figure 3.11.

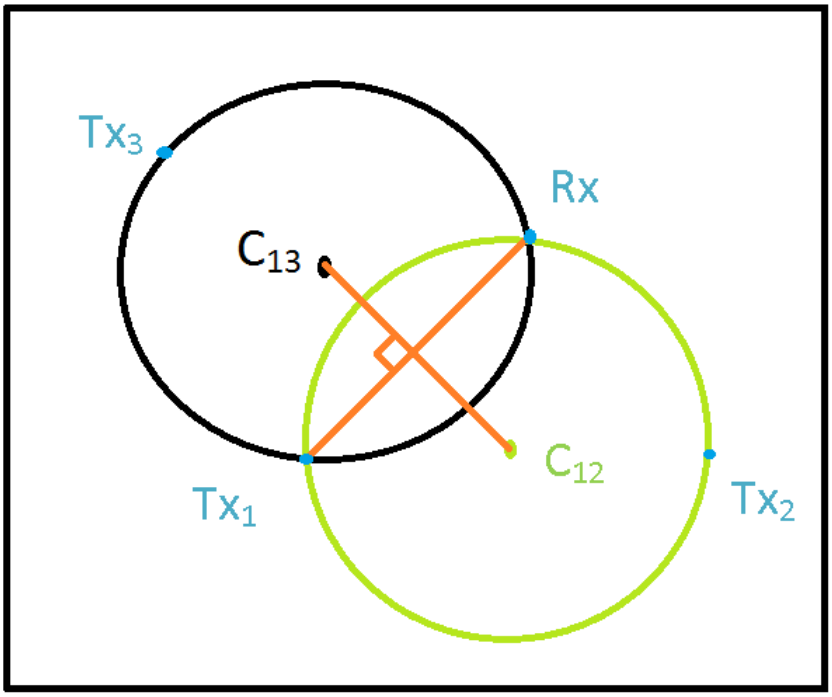

Figure 3.11: Rx position estimate from triangulation.

It should be noted here that Tx1 is common to both of the circles and a line can be drawn connecting the centers of the two circles. Then a perpendicular line from Tx1 is drawn on the connecting line between the centers of the circles. The drawn perpendicular line from Tx1 intersects both of the circles at the Rx position. The accuracy of the position estimate depends on the accuracy of the measured AoAs and this is explored in the next chapter. A study has been conducted to find a relationship between the accuracy of position estimate and the accuracy of measured AoA. Moreover, the factors that affect the accuracy of the measured AoA has been studied extensively. Finally an equation has been derived to predict the standard deviation of measured AoA.

Chapter 4

Simulation results

The technique for position estimation from dAoAs using multiple antenna elements and interferometry has been explained in the last chapter. The flowgraph of the proposed technique is shown in Figure 4.1. In Figure 4.1, (x_n, y_n) refers to the co-ordinates of the Tx_n, f_n is the transmitting frequency of Tx_n, $\Delta\phi_n$ is the phase difference between signals from Tx_n at two receiving antennas, θ_n is the AoA of the signal transmitted from Tx_n, (x_R, y_R) is the estimated Rx position, and n is the Tx index where $n = 1, 2, 3$. The receiver receives FM band (88 MHz - 108 MHz) radio signals from spatially separated transmitters (Tx). The FM band signals have a 200 kHz separation between channels. Therefore, the Tx signals can be spectrally isolated using an FFT. Then for each spectrally-isolated FM signal, the phase difference between the two signals collected from two difference receive antennas is estimated enabling the estimation of the dAoAs for each Tx signal. Then the dAoAs are exploited to estimate the position of the receiver (Rx).

The accuracy of the Rx position estimation depends on the accuracy of the measured dAoA. The dAoA accuracy is a function of the number of samples for FFT length ($N_{samples}$), the Signal-to-Noise Ratio (SNR) at the receiver, the baseline separation between the Rx antenna elements (d), and the true AoA. The FM band radio signals occupy 20 MHz (88 MHz - 108 MHz). The radio signals will be downconverted to baseband first and then digitized. After converting the FM radio

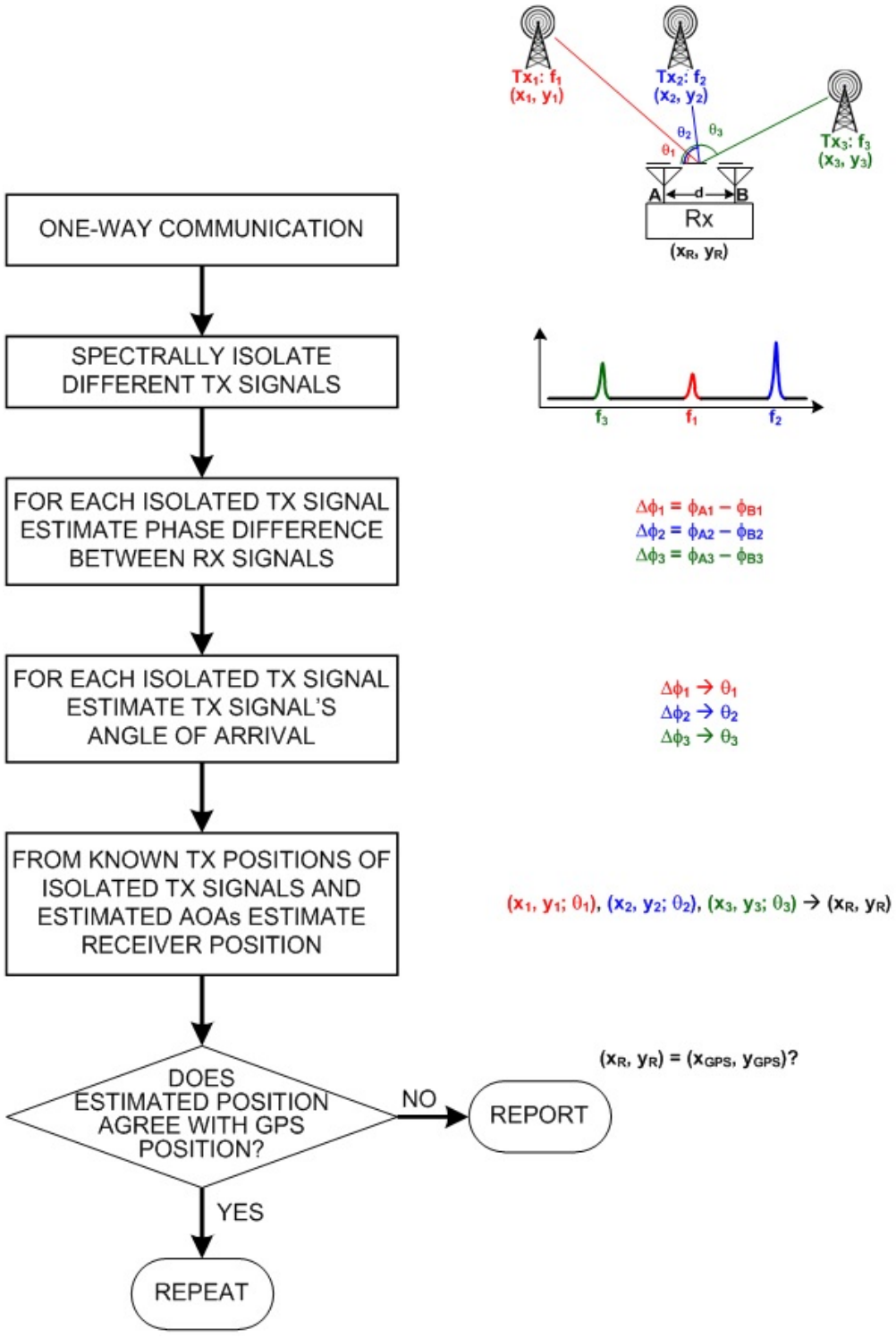

Figure 4.1: Graphical depiction of independent receiver position estimation process for comparison with satellite-based navigation position.

signals to baseband, the maximum frequency component will be about 20 MHz. The required frequency resolution (Δf) is 200 kHz (the separation between channels). The FFT length is then calculated as shown in Equation (4.1).

$$\Delta f = \frac{f_s}{N_{samples}} \tag{4.1}$$

where Δf is the frequency resolution, f_s is the sampling frequency, and $N_{samples}$ is the FFT length. According to Nyquist theorem, the sampling frequency must be at least twice the maximum signal bandwidth to retrieve the original signal. Therefore, f_s must be at least 40 MHz. The f_s is assumed to be 50 MHz in this dissertation. Then the $N_{samples}$ is calculated to be 250. The FFT length is chosen to be 256 (closest power of 2).

In this chapter, the accuracy of the position estimation from the measured dAoA is simulated first. Then the factors that are affecting the accuracy of the measured AoA are studied extensively. Moreover, an equation has been derived to predict the standard deviation of measured AoA (σ_{AoA}) based on $N_{samples}$, SNR, baseline separation between antenna elements (d), and true AoA. The derivation of the closed form equation relinquishes the demand for comptational loads, memory, and computation time. It will be shown that the derived equation predicts σ_{AoA} with a value of coefficient of determination (R^2) greater than 0.85.

4.1 Error analysis in position estimation

The proposed triangulation technique estimates the position of the receiver based on dAoAs from spatially separated transmitters at known positions. The accuracy of the position estimate depends of the accuracy of the measured AoA. Calculation of the AoA accuracy demands memory, execution time, and computational load. Therefore, an equation has been derived to predict the accuracy of the AoA. In this section, the accuracy of the position estimation will be simulated based on the AoA accuracy provided by the derived equation.

The accuracy of the position estimate is simulated by applying the proposed method in a grid consisting of the Rx and 3 Txs as shown in Figure 4.2.

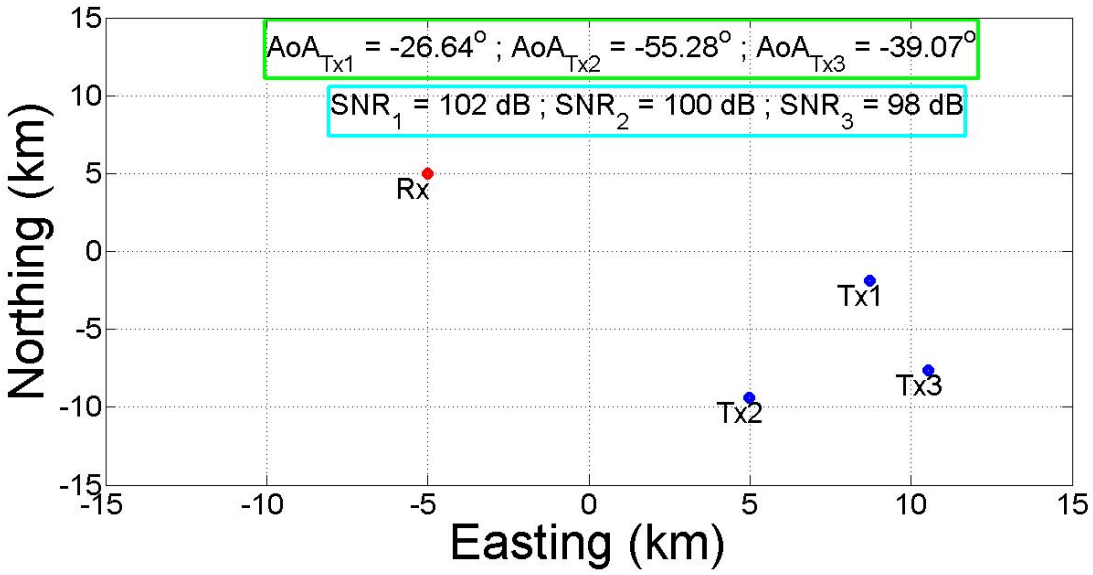

Figure 4.2: Position of the Rx and 3 Txs.

Based on the range between the receiver and the transmitters, the SNR is calculated from Equation (2.2). In the calculations of Equation (2.2), the gain of both the Tx and the Rx antennas are assumed to be 0 dBi and free space propagation losses are ignored. The true AoA is calculated from the true positions of the Rx and the Txs with the help of geometry. The baseline separation between Rx antenna elements (d) and $N_{samples}$ are chosen to be 256 and $\frac{\lambda}{2}$ respectively. The transmitted power (P_{Tx}) and Noise Figure (NF) of the receiver are chosen to be 50 dBW and 8 dB respectively. The parameters are then plugged into the Equation (4.2) to find the standard deviation of AoA (σ_{AoA}).

$$\sigma_{AoA} = \frac{53.256\exp(-0.02746\beta)}{(\sqrt{N_{samples}})(d/\lambda)(\sqrt{SNR(linear)})} \tag{4.2}$$

The step-by-step derivation of the Equation (4.2) is presented in the next section. Using this AoA standard deviation, a Gaussian random sequence of AoA_i with the length of 1000 samples repre-

senting various estimates of AoA from i-th transmitter. The AoAs are then exploited to find the position of the receiver as shown in Figure 4.3.

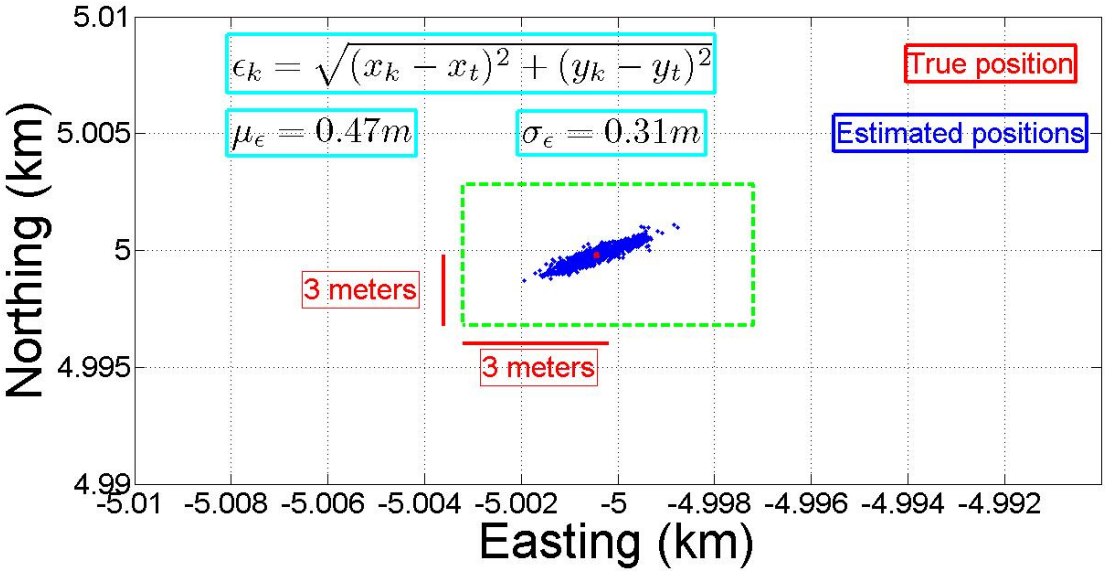

Figure 4.3: Accuracy of position estimation of the proposed method.

The accuracy of the position estimation is calculated as shown in Equation (4.3).

$$\varepsilon_k = \sqrt{(x_k - x_t)^2 + (y_k - y_t)^2}, \qquad k = 1, 2... \tag{4.3}$$

where (x_k, y_k) is the position estimation from k-th sample of AoA (AoA_k), (x_t, y_t) is the true position of the receiver, and ε_k is the error in position estimation with k-th sample of AoA (AoA_k). It is shown here that the proposed technique provides position estimation accuracy with a bias (μ_ε) of 0.47 m and standard deviation (σ_ε) of 0.31 m. However, the accuracy of the position estimation is subjected to efficient selection of transmitters that will be discussed in section 4.4.

4.2 Error analysis in AoA estimation

In the phase interferometry technique, the measured phase difference between two received signals from two spatially separated antenna elements are employed to calculate the AoA of the incoming signal. However, there are a number of factors that reduce the accuracy of the practical direction finding system, such as multipath, Co-Channel Interference (CCI), and mutual coupling between antenna elements.

Multipath is a major problem that can cause errors on the order of degrees in calculating the AoA [98]. Multipath is a phenomenon that causes RF signals to arrive at the receiving antennas by two or more paths. However, the effect of multipath can be minimized by isolating the Rx antenna elements from adjacent scatterers and thus multipath effect is not considered.

CCI is another source of error that corrupts AoA calculation [98]. CCI is the crosstalk between two transmitters operating at the same frequency. If the signal of interest is strong, then the averaging technique reduces the effect of CCI. However, the proposed navigation system exploits FM radio band signals that have spatially diversified transmitters i.e. FM transmitters at the same frequency do not operate near one another. Therefore, CCI is not taken into account for evaluating the performance of the proposed system.

Mutual coupling between the antenna elements is another source of errors. It has been previously discussed that the antenna baseline (spacing between antenna elements) must be kept less than or equal to $\frac{\lambda}{2}$, where λ is the free space wavelength at the transmitting frequency. This helps the phase difference between 0 and π and thus results in two solutions, such as the true AoA and the true AoA plus π. Another set of measurements by antennas forming an additional collinear baseline eliminates the ambiguity as discussed in the previous section. However, the effect of mutual coupling can be neutralized by a careful calibration of the mutual coupling in a standalone environment.

Thermal noise is the dominant and unavoidable source of error in this system. The antenna array and the receiver equipment works above absolute zero Kelvin temperature and thus there will be thermal noise due to random motion of the charged particles. The thermal noise corrupts phase estimation and thus produces errors in AoA calculation. Received signal power much greater than the noise power level (a high SNR) provides a finer AoA estimation than weaker received signal (assuming the noise power level is relatively constant). The theoretical thermal noise power is given by the Equation (4.4).

$$P_n = kTBF \tag{4.4}$$

where P_n is the thermal noise power in Watts, k is the Boltzman constant ($1.38\text{X}10^{-23}$ J/K), T is the receiver temperature in Kelvin, B is the receiver bandwidth in Hz, and F is the receiver Noise Figure (NF). NF is a measure of the added noise from the receiver. The SNR is given by the Equation (4.5).

$$SNR = \frac{P_s}{P_n} \tag{4.5}$$

where P_s is the average power of the received signal and P_n is the thermal noise power of the receiver calculated from Equation (4.4). It should be noted here that the SNR in Equation (4.5) refers to the SNR that will be used to calculate the AoA and not the SNR at the antenna terminals. The reason being that the operating bandwidth of the antenna is 20 MHz (88 MHz - 108 MHz) whereas, the bandwidth of the IF filter of the receiver is 200 kHz (channel bandwidth). Therefore, the B values are different at antenna terminal and at the receiver input terminal in Equation (4.4).

The received signal is assumed to be sinusoidal with zero mean (no DC component). The complex induced voltages at two spatially different antennas separated by half wavelength at the transmitting freqeuncy can be represented by the Equation (4.6).

$$V_{si} = V_{mi} e^{(j\phi_i)}, \qquad i = 1, 2...N_{samples} \tag{4.6}$$

where V_{si} refers to the complex signal voltage (V) at the antenna i, V_{mi} refers to the signal amplitude (V) at the antenna i, and ϕ_i represents the phase of the received signal (radian) at antenna i. Assuming an 1Ω resistor, the amplitude of the signal (V_{mi}) can be calculated by taking the square root of the signal power as shown in the Equation (4.7).

$$V_{mi} = \sqrt{2P_{si}}, \qquad i = 1, 2...N_{samples} \tag{4.7}$$

where P_{si} is the received signal power at antenna i.

The thermal noise is best represented by a Gaussian random sequence with zero mean [99]. The amplitude distribution of the Gaussian random sequence is characterized by the Probability Density Function (PDF) that is presented in Equation (4.8).

$$P(x) = \frac{1}{\sigma\sqrt{2\pi}} e^{-\frac{(x-\mu)^2}{2\sigma^2}} \tag{4.8}$$

where x represents a random variable which is noise in this case, $P(x)$ is the PDF of the distribution of random variable x, μ is the mean of the distribution ($\mu = 0$ as there is no DC component), and σ is the standard deviation of the distribution. Moreover, the variance and the standard deviation of the Gaussian random sequence represent the total noise power and the RMS value of the noise signal respectively. Thus, the RMS value of the noise signal can be calculated as the square root of the total noise power (assuming DC component to be zero). The standard deviation of the noise signal is calculated as the square root of thermal noise power as shown in Equation (4.9).

$$\sigma_x = \sqrt{P_n} \tag{4.9}$$

The length of the Gaussian random sequence is chosen to be equal to the length of the FFT

($N_{samples}$).

$$v_{ni} = \frac{\sigma_x}{\sqrt{2}}(\gamma_1 + j\gamma_2), \qquad i = 1,2...N_{samples} \tag{4.10}$$

where v_{ni} is a complex Guassian random sequence vector with length equal to $N_{samples}$ with a zero mean and standard deviation equal to σ_x, γ_1 and γ_2 are Additive White Gaussian Noise (AWGN) models with the length equal to $N_{samples}$. Then the mean of the sequence is taken as the noise signal for one snapshot as shown in Equation (4.11).

$$V_{ni} = \bar{v}_{ni}, \qquad i = 1,2...N_{samples} \tag{4.11}$$

In this dissertation, 'snapshot' refers to a record of the received signal at this particular position at this instant time and it is denoted as $N_{snapshots}$. The complex voltages at the receivers are then found by adding the noise voltages to the signal voltages as shown in the Equation (4.12).

$$V_i = V_{si} + V_{ni}, \qquad i = 1,2...N_{samples} \tag{4.12}$$

where V_i represents the complex signal voltage with added noise at the receiver i that closely resembles the practical scenerio. The phase of the received signals are extracted from the angles of the complex signals as shown in Equation (4.13).

$$\phi_i = \angle V_i, \qquad i = 1,2...N_{samples} \tag{4.13}$$

Finally, the AoA of the incoming signal is calculated as shown in Equation (4.14).

$$\theta = cos^{-1}(\frac{(\phi_2 - \phi_1)\lambda}{2\pi d}) \tag{4.14}$$

where θ is the AoA of the incoming signal, $(\phi_2 - \phi_1)$ is the phase difference between the two received signals at two spatially separated antennas, λ is the wavelength at the transmitting frequency, and d is the baseline distance between the two antennas.

The estimated AoA of the received signal that was derived in the previous section is susceptible to different factors, such as SNR, number of samples ($N_{samples}$), the AoA of the incoming signal (true AoA), and the baseline distance between antenna elements (d). The effect of each of the parameters on the AoA estimation has been examined and is explained in detail in this section. After careful investigation of the impact of each of the parameters, an equation has been developed that predicts the accuracy of the calculated AoA, σ_{AoA}. The number of snapshots ($N_{snapshots}$) is kept constant to be $10,000$ for the analysis of this section. The accuracy of the measured AoA is expressed as the standard deviation of the measured AoA with respect to the true AoA. The mathematical espression for the σ_{AoA} is shown in Equation (4.15).

$$\sigma_{AoA} = \sqrt{\frac{(AoA_i - AoA_{true})^2}{N_{snapshot}}}, \qquad i = 1,2..N_{snapshot} \tag{4.15}$$

where AoA_i is the estimated AoA at i-th snapshot.

4.2.1 Number of samples, $N_{samples}$

The number of samples taken during each snapshot plays an important role in the estimation of AoA. A large number of samples per snapshot ($N_{samples}$) reduces the error in AoA estimation. The estimated accuracy of AoA as a function of $N_{samples}$ is shown in Figure 4.4.

It is shown in Figure 4.4 that σ_{AoA} is 0.0001 degree for $N_{samples}$ of 256 and it decreases with increasing $N_{samples}$. The probability density of AoA for $N_{samples}$ equal to 256 is shown in Figure 4.5.

It is shown in Figure 4.5 that the AoA estimate has a small bias of 0.0044^{o} at fixed values of $SNR = 80$ dB, $N_{snapshots} = 10,000$ and true AoA $= 60^{o}$. Moreover, the distribution exhibits a standard deviation (σ_{AoA}) of 0.0001^{o} and thus the measured data is expected to be within 0.0001^{o} at 68% of the time.

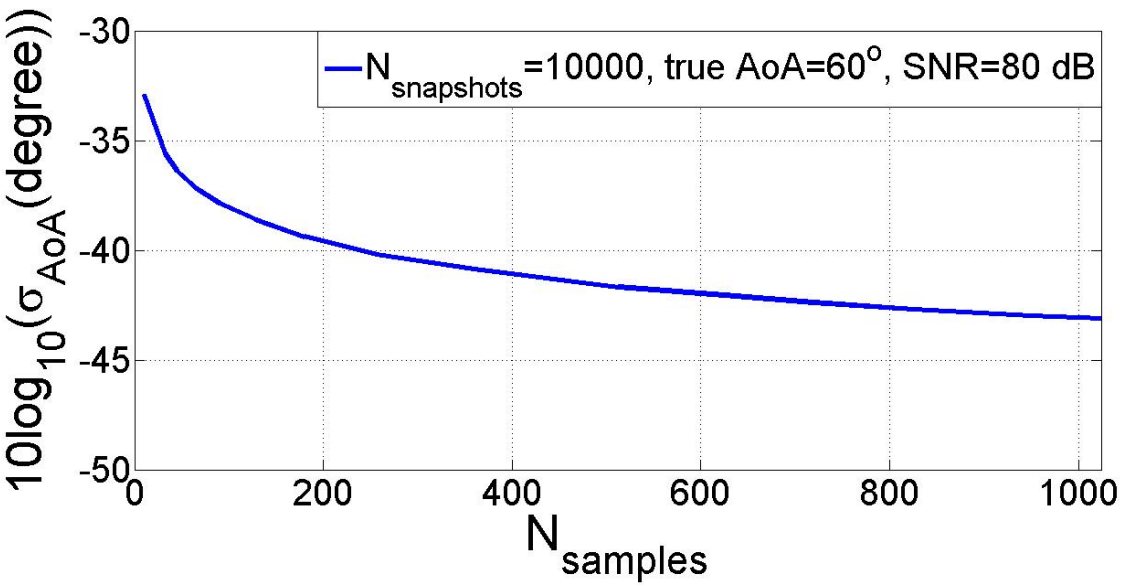

Figure 4.4: AoA estimation error as a function of $N_{samples}$.

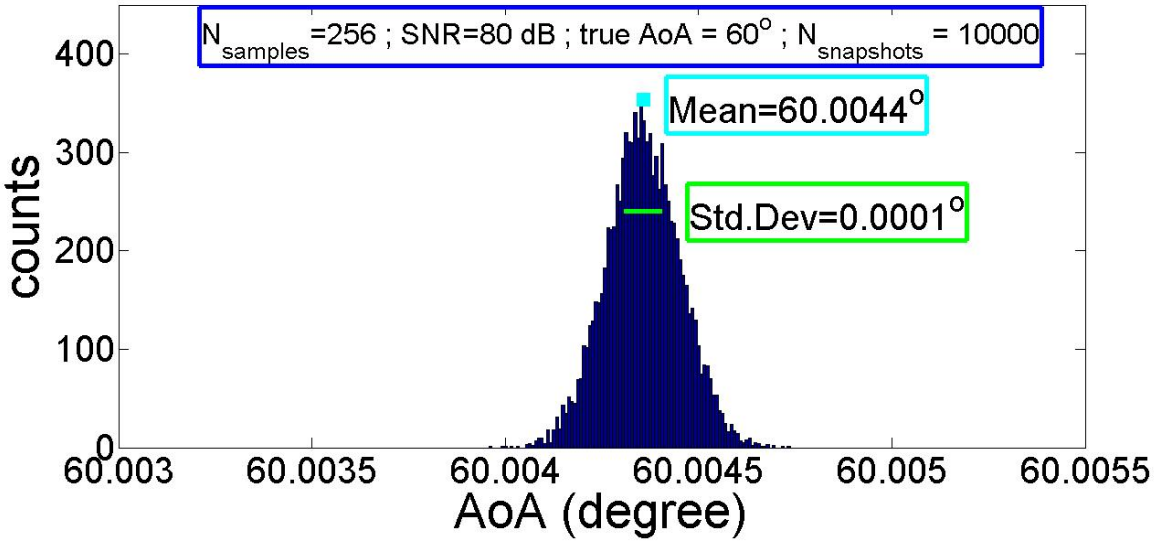

Figure 4.5: Histogram of AoA.

In order to predict the effect of varying $N_{samples}$ over σ_{AoA}, a curve-fitting approach has been adopted and shown in Figure 4.6.

The coefficient of determination or R^2 value of the predicted equation is found to be greater than

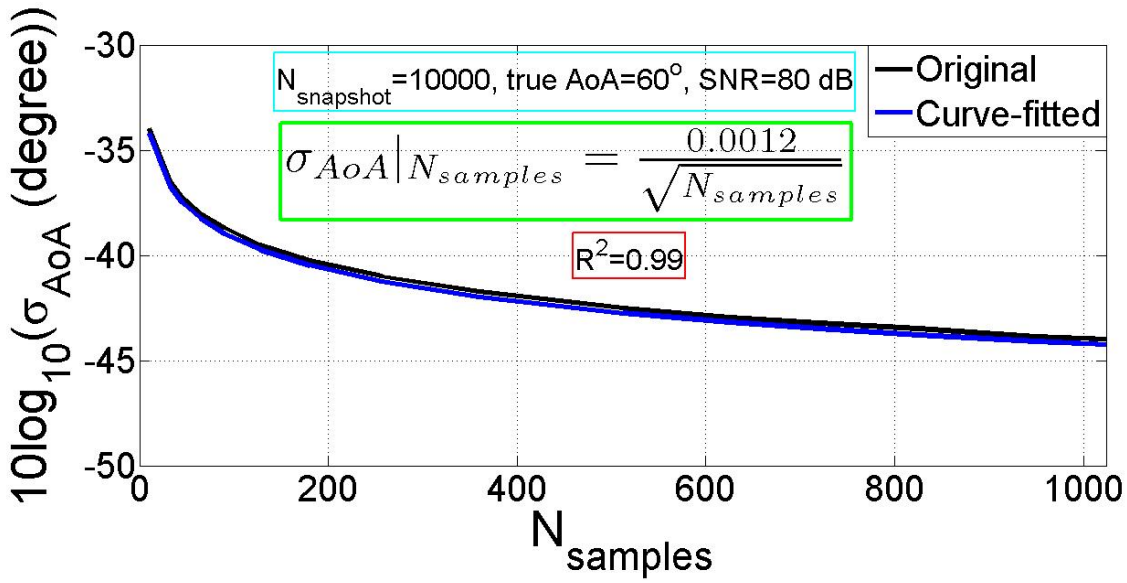

Figure 4.6: Calculated σ_{AoA} and predicted σ_{AoA} vs $N_{samples}$.

0.9. The equation for predicting the accuracy of AoA for different values of $N_{samples}$ is inversely proportional to the square root of $N_{samples}$ as shown in Equation (4.16).

$$\sigma_{AoA}|_{N_{samples}} = \frac{p}{\sqrt{N_{samples}}} \tag{4.16}$$

where p is a scalar. The coefficient of determination, denoted by R^2, is a number that indicates how well a set of data fits into a statistical model. The range of R^2 values lie between 0 and 1. A R^2 value of 1 represents the best fit between a set of data and a statistical model. The coefficient of determination is calculated by the Equation (4.17).

$$R^2 = 1 - \frac{SS_{res}}{SS_{tot}} \tag{4.17}$$

where SS_{res} refers to the sum of squares of the residuals and SS_{tot} refers to the total sum of squares. Assume that a data set has observed values y_i and predicted values f_i. If the mean of the observed values is $\bar{y}$, then SS_{res} and SS_{tot} can be calculated by the following Equations (4.18) and (4.19).

$$SS_{res} = \sum_i (y_i - f_i)^2 \tag{4.18}$$

$$SS_{res} = \sum_i (y_i - \bar{y})^2 \tag{4.19}$$

4.2.2 SNR

The effect of SNR on the accuracy of the AoA is shown in Figure 4.7.

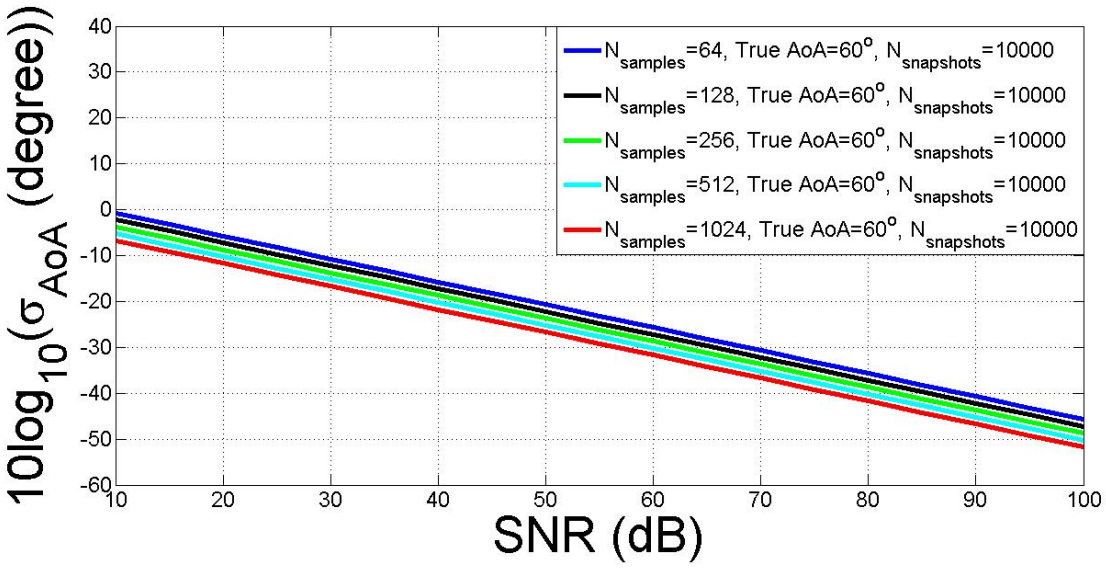

Figure 4.7: σ_{AoA} vs SNR for a range of $N_{samples}$.

It can be noted here that the accuracy of the AoA (σ_{AoA}) increases with the increased value of SNR. However, the change in AoA becomes negligible after SNR values of higher than 40 dB. A curve-fitting approach has been conducted to find a closed-form relationship between SNR and σ_{AoA} that results in Equation (4.20).

$$\sigma_{AoA}|_{SNR} = \frac{p}{\sqrt{SNR(linear)}} \tag{4.20}$$

where p is scalar. Thus the accuracy of the AoA is inversely proportional to the square root of SNR in linear format. The equation for predicting σ_{AoA} for different SNR values has been plotted in Figure 4.8 for fixed values of $N_{snapshots} = 10,000$, $N_{samples} = 256$, and true AoA $= 60^0$. The R^2

value for the equation is calculated to be greater than 0.9.

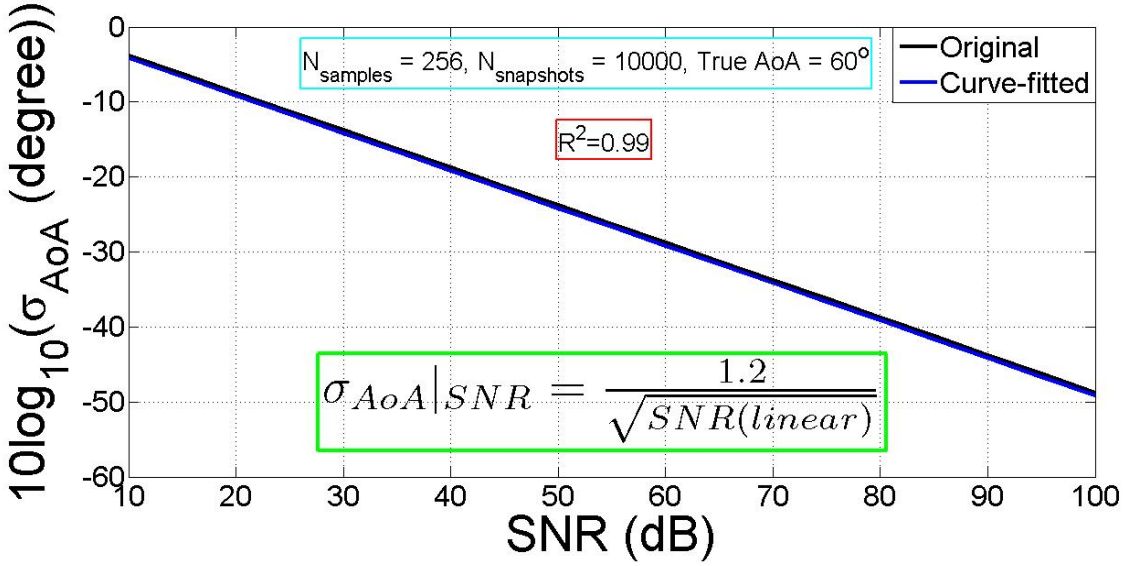

Figure 4.8: Calculated σ_{AoA} and predicted σ_{AoA} vs SNR.

4.2.3 Baseline distance between Rx antennas, d

The baseline distance between Rx antennas affects the accuracy of the AoA. A parametric study of σ_{AoA} in dB format vs baseline distance between Rx antennas has been shown in Figure 4.9 for different values of $N_{samples}$.

It is shown in Figure 4.9 that the measured AoA becomes stable at a baseline distance close to $\frac{\lambda}{2}$. A curve-fitting approach has been practiced to develop a closed-form relationship between AoA accuracy and baseline distance that results in Equation (4.21).

$$\sigma_{AoA}|_d = \frac{p}{d} \tag{4.21}$$

where p is a scalar, and d is the baseline distance between Rx antennas (m). Thus the AoA accuracy is inversely proportional to the baseline distance between Rx antennas. The equation for

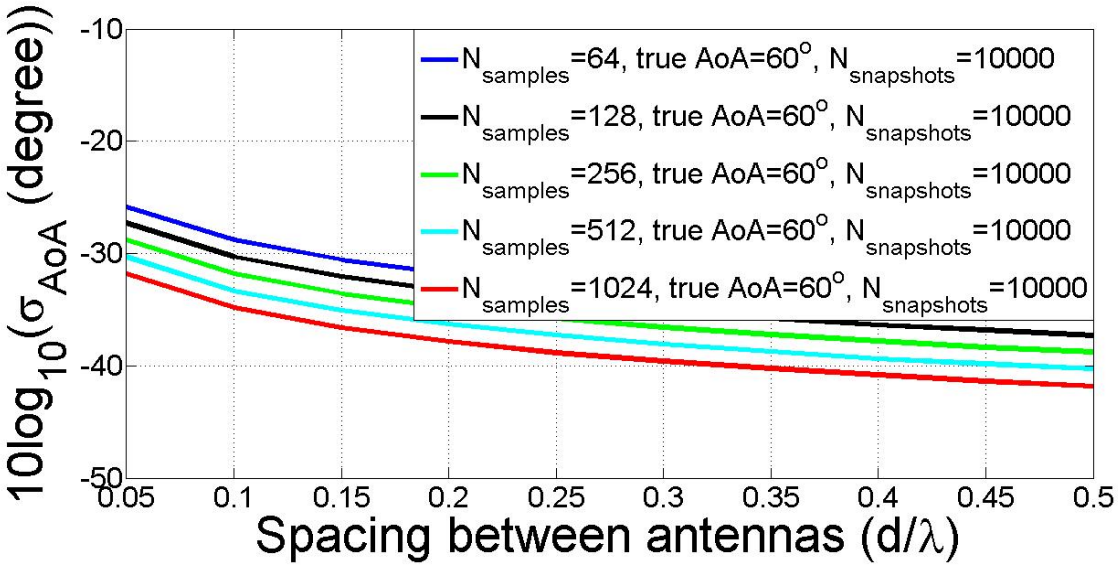

Figure 4.9: σ_{AoA} vs baseline.

predicting σ_{AoA} for different baseline separation values has been plotted in Figure 4.10 for fixed values of $SNR = 80$ dB, $N_{snapshots} = 10000$, $N_{samples} = 256$, and true AoA $= 60^0$. The R^2 value for the equation is calculated to be greater than 0.9.

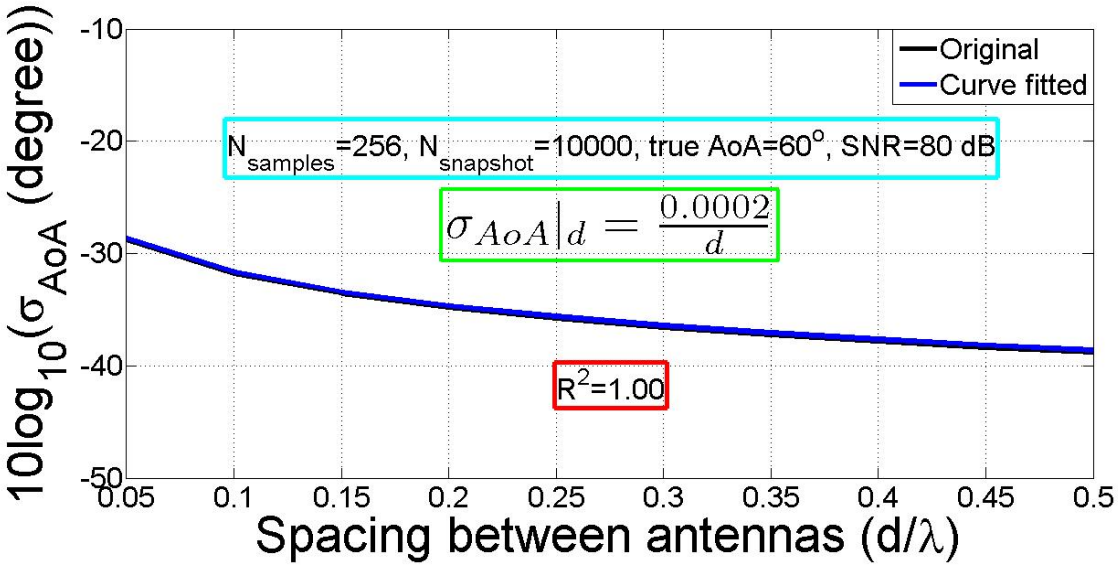

Figure 4.10: Calculated σ_{AoA} and predicted σ_{AoA} vs baseline separation (d).

4.2.4 True AoA

The AoA accuracy depends on the true AoA of the incoming signal. The σ_{AoA} exhibits low accuracy for AoA values between 0 to 10 degrees. Therefore, the proposed navigation system utilizes Tx positions that are between 10 to 170 degrees. A parametric study of σ_{AoA} vs true AoA for different values of $N_{samples}$ has been shown in Figure 4.11.

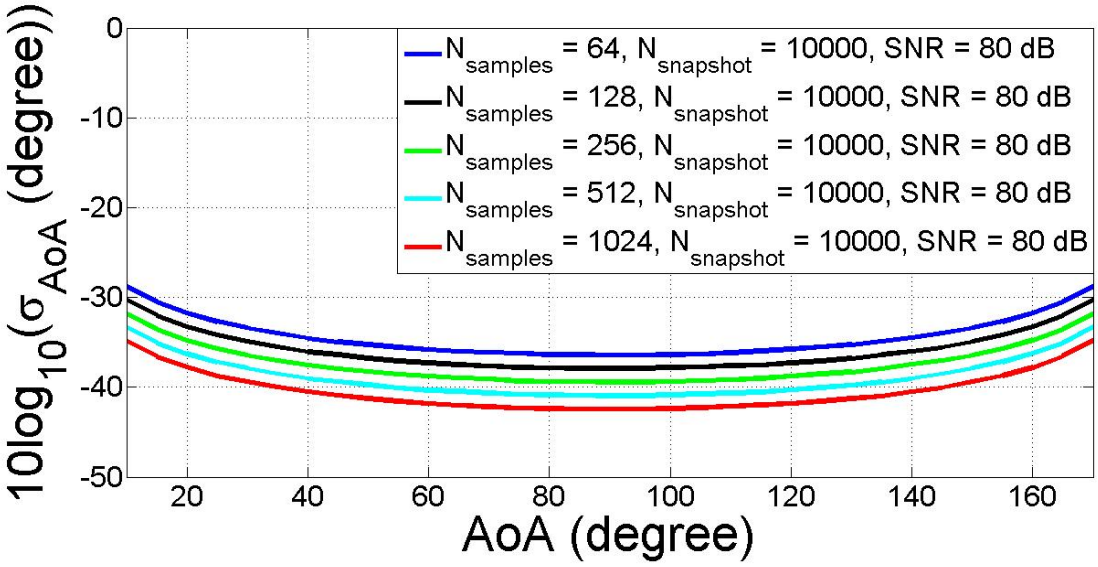

Figure 4.11: σ_{AoA} vs true AoA.

Figure 4.12 shows a curve-fitting approach to find a closed-form relationship between σ_{AoA} and true AoA for $N_{samples} = 256$, $N_{snapshot} = 10,000$, and $SNR = 80$ dB.

The predicted equation can be expressed as shown in Equation (4.22).

$$\sigma_{AoA}|_{trueAoA} = c_1 \exp(c_2 \beta) \tag{4.22}$$

where c_1 and c_2 are scalars and β is represented by Equation (4.23). The R^2 value of the predicted equation is found to be greater than 0.85.

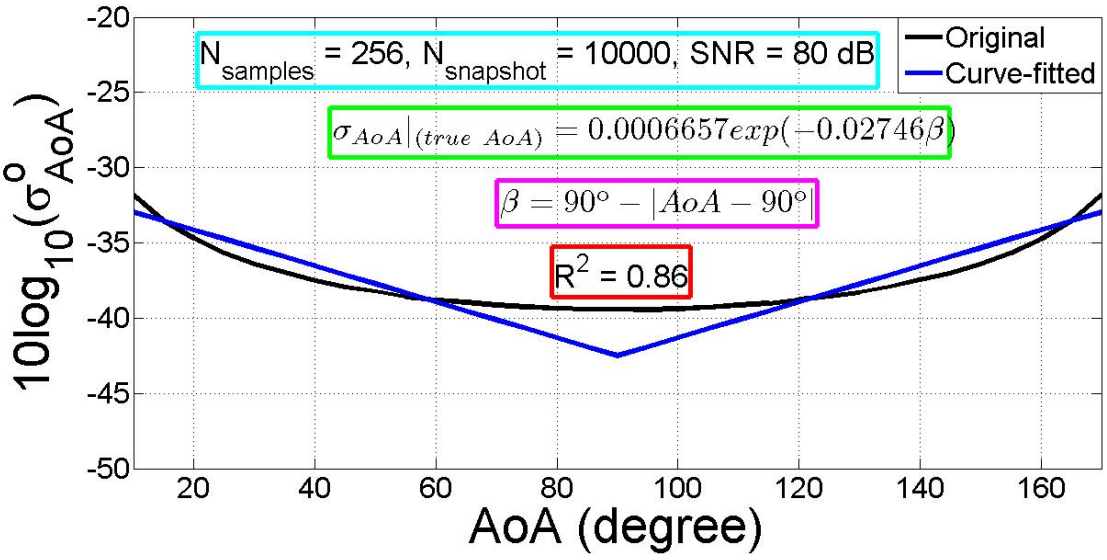

Figure 4.12: Calculated σ_{AoA} and predicted σ_{AoA} vs true AoA.

$$\beta = 90 - |AoA - 90| \tag{4.23}$$

4.2.5 Predicted equation

In the last 4 sections, the effect of $N_{samples}$, SNR, baseline distance between Rx antennas, and true AoA on the σ_{AoA} has been studied separately. Moreover, the closed-form relationships between the parameters and σ_{AoA} have been established. In this section, the effect of all the parameters on the σ_{AoA} simultaneously has been studied that results in Equation (4.24) that is revisited here from Equation (4.2).

$$\sigma_{AoA} = \frac{53.256\exp(-0.02746\beta)}{(\sqrt{N_{samples}})(d/\lambda)(\sqrt{SNR(linear)})} \tag{4.24}$$

Equation (4.24) predicts σ_{AoA} with a R^2 value greater than 0.85 for a range of different parameters as shown in Table 4.1.

Table 4.1: Range of values of parameters for equation predicting σ_{AoA}

Parameters	Range
$N_{samples}$	64 : 1024
SNR	30 dB : 150 dB
Baseline separation	$\frac{\lambda}{20} : \frac{\lambda}{2}$
True AoA	$10^{o} : 170^{o}$

4.3 Maximum range and lowest SNR

The accuracy of the AoA calculation is a function of SNR and true AoA as discussed in the previous section. Moreover, the SNR is a function of the range between the Tx and the Rx as shown in Equation (2.2). Therefore, the SNR determines the maximum allowable range between the Tx and the Rx by the Equation (4.25).

$$R_{max} = \frac{\lambda}{4\pi}\sqrt{\frac{P_t G_t G_r}{P_r}} \tag{4.25}$$

where P_t and P_r are the transmitted power by the Tx and the received power by the Rx in Watts respectively, G_t and G_r are the gains of the Tx antenna and Rx antenna respectively, and λ is the wavelength at the Tx frequency in meters. The assumed values of the aforementioned parameters are shown in Table 4.2.

Table 4.2: Assumed values of the parameters

Parameters	Assumed values
G_t	2 dBi
G_r	2 dBi
P_t	50 dBW

It has been shown in the Figure 4.7 that the σ_{AoA} exceeds 0.01 degree with a SNR lower than 45 dB when $N_{samples} = 256$. Therefore, the minimum SNR required by the proposed algorithm has been set to 45 dB or higher.

$$SNR \geq 45dB \tag{4.26}$$

The maximum range between the Rx and the Tx has been calculated with the SNR_{min} of 45 dB. Assuming the values listed in Table 4.2, it was determined that the maximum allowed range for the proposed algorithm was 30 km.

$$R_{max} \leq 30km \tag{4.27}$$

In this section, the minimum SNR and the maximum range between the Tx and the Rx has been determined. However, the proposed method triangulates AoAs for localization. Therefore, the geometrical combination formed by the Tx stations and the Rx affect the triangulation operation and thus the accuracy of position estimate. In the next section, The effect of geometrical combinations of the transmitters on the accuracy of the position estimate will be studied.

4.4 Tx selection algorithm

The propsoed method triangulates the dAoAs of the transmitters to estimate the receiver position. The accuracy of dAoA calculation depends on the accuracy of AoA calculation. It has been shown in the previous section that the accuracy of the AoA calculation depends on different parameters, such as $N_{samples}$, SNR, the baseline separation between the Rx antennas (d), and the true AoA. Moreover, the proposed technique employs triangulation for position estimate. The accuracy of the triangulation technique depends on the geometrical combinations formed by the Tx stations. Therefore, an emperical study will be studied in this section to simulate the effect of different geometrical combinations formed by the transmitters on the accuracy of the proposed technique.

The effect of different geometrical combinations was carried out by simulating a grid (50 km $\times$ 50 km) with different positions of the Rx on the grid. It was shown in the previous section that the maximum range for accurate position estimate by the proposed method was calculated to be 30 km from the Tx stations. Therefore, the Tx position was chosen such that the grid boundary was 30 km from the Tx stations in any direction. The study was conducted by forming different

geometrical combinations, such as right angle triangle, acute angle triangle, and obtuse angle triangle. The simulated results for all the aforementioned combinations will be presented in this section.

The resolution of the Rx position on the grid was chosen to be 500 m. The true AoAs of the Tx stations were calculated from the geometrical positions of the Tx stations by the Equation (4.28).

$$AoA(degree) = \tan^{-1}(\frac{Tx_n - Rx_n}{Tx_e - Rx_e}) \tag{4.28}$$

where Tx_n, Tx_e are the Tx positions and Rx_n, Rx_e are the Rx positions in northing and easting respectively. The received power at each Rx position on the grid from the transmitters was calculated by the Friis Transmission equation as shown in Equation (2.2). It should be noted here that the thermal noise of the receiver was calculated to be -123 dBm. The thermal noise was calculated using Equation (4.4) with an Noise Figure of 8 dB and a bandwidth of 10 kHz. The reason for choosing 10 kHz of bandwidth will be discussed with the measurement results in the next chapter.

The uncertainty (σ) of the AoA measurement was derived from the closed form equation as derived in Equation (4.24). The $N_{samples}$ was chosen to be 2048 in the calculation to be consistent with the measurement as will be discussed in the next chapter. The position estimate for each of the Rx position was calculated to be the average of 1000 snapshots. The uncertainty associated with the position estimate during each snapshot was characterized by a Gaussian random number sequence with a length equal to the number of snapshots. The PDF of the Gaussian Random number sequence was shown in Equation (4.8). The calculated σ_{AoA} was then added to the true AoA at each Rx position to mimic the measured AoA as shown in Equation (4.29).

$$AoA_{sim}(i,j) = AoA_g(i,j) + \sigma_{AoA}(i,j) \tag{4.29}$$

where $AoA_g(i,j)$ is the true AoA (degree) calculated from geometry, $\sigma_{AoA}(i,j)$ (degree) is the uncertainty of AoA measurement derived from Eqaution (4.24), and $AoA_{sim}(i,j)$ (degree) is the

simulated AoA for the (i^{th}, j^{th}) position of the Rx on the grid. The simulated dAoA was then calculated from the difference between the simulated AoAs of the Tx stations as shown in Equations (4.30), (4.31), and (4.32).

$$dAoA21_{sim}(i,j) = AoA2_{sim}(i,j) - AoA1_{sim}(i,j) \tag{4.30}$$

$$dAoA32_{sim}(i,j) = AoA3_{sim}(i,j) - AoA2_{sim}(i,j) \tag{4.31}$$

$$dAoA13_{sim}(i,j) = AoA1_{sim}(i,j) - AoA3_{sim}(i,j) \tag{4.32}$$

where $AoA1_{sim}(i,j)$, $AoA2_{sim}(i,j)$, and $AoA3_{sim}(i,j)$ are the AoAs of signals from Tx1, Tx2, and Tx3 respectively. The dAoAs were then utilized in triangulation for position estimate. The proposed triangulation technique for position estimate was explained in chapter 3. The triangulation technique creates locus of points on a circle for possible receiver positions as shown in Figure 4.13.

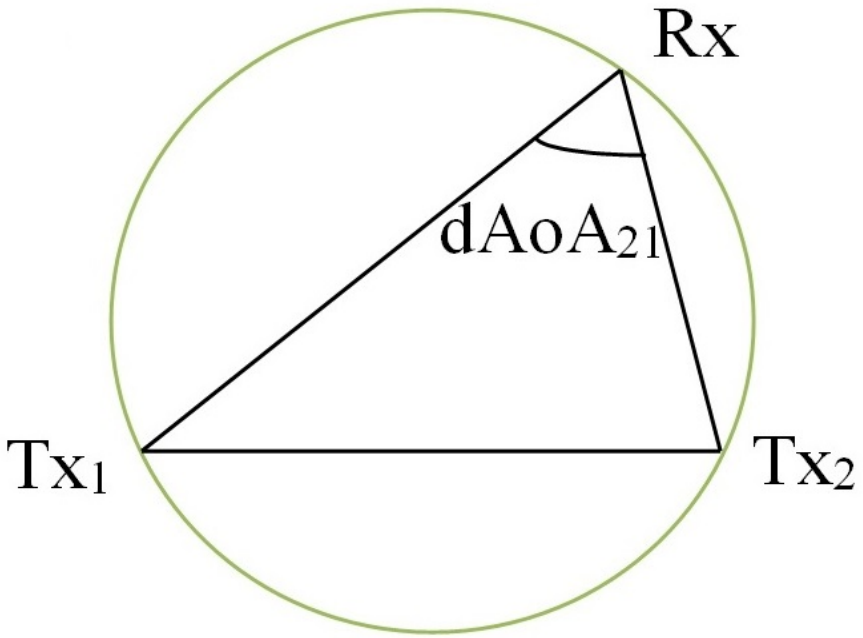

Figure 4.13: The locii of possible Rx positions.

It can be seen in Figure 4.13 that the triangulation technique requires the Rx position to be out of the baseline formed by the Tx1 and Tx2. The position was then estimated as the intersection of the two circles formed by two different Tx pairs.

The position estimate requires the intersection of two circles formed by two Tx pairs. However, the accuracy of the position estimate is augmented when position estimate is verified by the third baseline. Therefore, the position estimate was performed using all the three available baselines as shown in Figure 4.14.

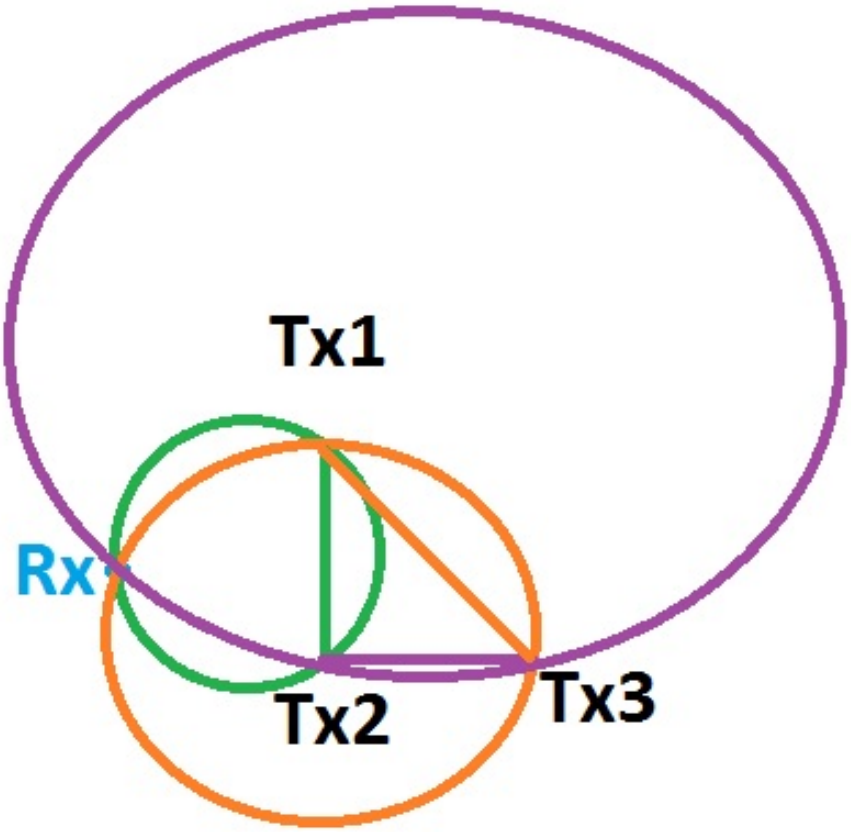

Figure 4.14: Position estimate utilizing three Tx pairs.

In Figure 4.14, green circle was formed by Tx1, Tx2, and Rx. The orange circle was formed utilizing Tx1, Tx3, and Rx. The purple circle was formed employing Tx2, Tx3, and Rx. The first

position was estimated as the intersection point of green and orange circles. The second position was measured to be the intersection point of orange and purple circles. The third position estimate was determined as the intersection point of green and purple circles. Then the position estimate was calculated as the average of the three estimated position as shown in Equation (4.33).

$$pos\_est_i = \sum \frac{pos\_est\_go_i + pos\_est\_op_i + pos\_est\_gp_i}{3} \tag{4.33}$$

where pos_est_i is the average position estimate for i^{th} snapshot, $pos\_est\_go_i$ is the position estimate using circles green and orange, $pos\_est\_op_i$ is the position estimate using circles orange and purple, and $pos\_est\_gp_i$ is the position estimate using circles green and purple for i^{th} snapshot. The calculated Rx position was then subjected to Equation (4.34).

$$pos_{error}(i,j) = \sqrt{(Rx_n(true) - Rx_n(sim))^2 + (Rx_e(true) - Rx_e(sim))^2} \tag{4.34}$$

where $pos_{error}(i,j)$ is the position error (m), $Rx_n(true)$ is the true Rx position in northing, $Rx_e(true)$ is the true Rx position in easting, $Rx_n(sim)$ is the simulated Rx position in northing, and $Rx_e(sim)$ is the simulated Rx position in easting at (i^{th}, j^{th}) position of the Rx on the grid.

The accuracy of position estimation resulting from different geometrical combinations formed by 3 Tx stations and the Rx varies from each other. The objective of this section is to quantify the level of position estimation accuracy for different geometrical combinations through simulations.

The geometrical combinations formed by 3 Tx stations assume different triangles, such as right angle triangle, acute angle triangle, and obtuse angle triangle. The resultant contour plots of the position estimation accuracy are shown in Figure 4.15, 4.16, and 4.17.

It is shown in Figure 4.15, 4.16, and 4.17 that the position errors were coarse when the Rx positions were away from one or more transmitters by 30 km or higher. This constraint comes from

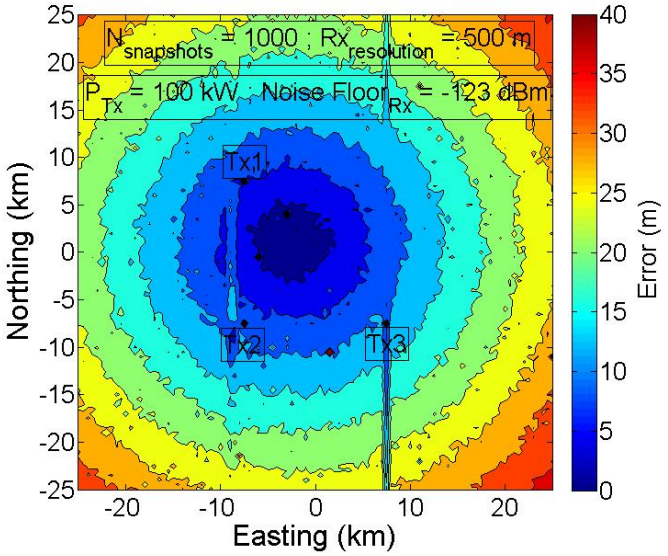

Figure 4.15: The contour map of the position estimate accuracy for right angle triangle formed by Tx stations.

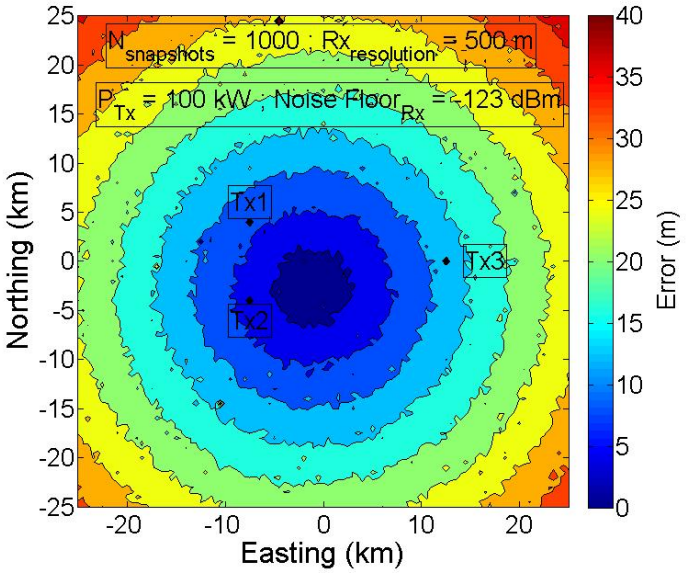

Figure 4.16: The contour map of the position estimate accuracy for acute angle triangle formed by Tx stations.

the fact that the SNR drops below 45 dB when the range between the Tx and the Rx is more than 30 km. This is true for all of the geometrical combinations. However, the position estimate during each snapshot was averaged over all of the position estimates utilizing all the available 3 Tx pairs.

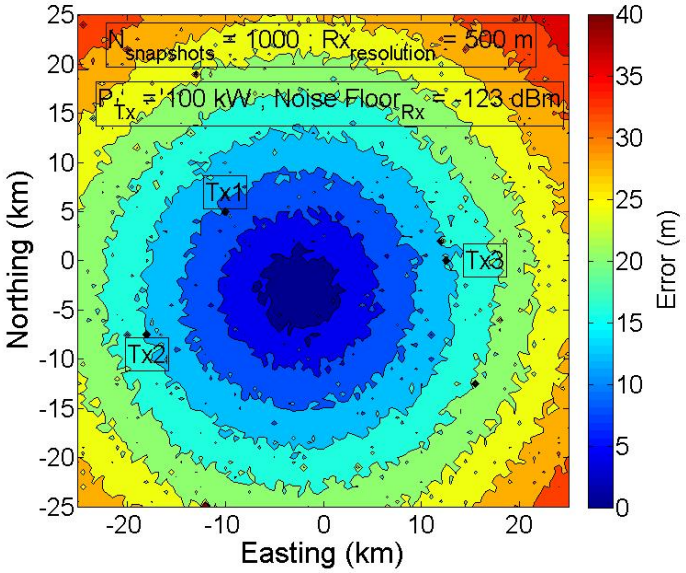

Figure 4.17: The contour map of the position estimate accuracy for obtuse angle triangle formed by Tx stations.

The averaging of all the position estimates reduced the position estimate error due to one or more transmitters.

It should be noted here that the proposed method provided a simulated position estimation error of less than 15 m for the Rx positions that were inside the triangle formed by the 3 Tx stations. Moreover, the Rx positions that were away from all the 3 Tx stations by 30 km or lower were estimated with an error of less than 20 m. The position estimation error tends to increase with an increasing range between the Rx and the Tx stations.

This chapter analyzed and examined the parameters that affect accuracy of the AoAs, dAoAs, and position estimate. The effect of different parameters, such as $N_{samples}$, SNR, baseline separation between Rx antennas (d), and the true AoA on the accuracy of AoA calculation has been studied extensively. Moreover, a closed form equation has been derived to predict the uncertainty of AoA calculation. Then the effect of geometrical combinations formed by the Tx stations, such as right angle triangle, acute angle triangle, and obtuse angle triangle on the position estimate ac-

curacy has been investigated. It was shown that the position estimate accuracy was finest inside the triangle formed by the 3 Tx stations. With the knowledge gained from literature and the simulation results, measurement was conducted for position estimate using the FM band radio signals. The measurement setup and the measurement results are the contents of next chapter.

Chapter 5

Measurement setup and results

It has been shown in the previous chapter that the accuracy of the position estimate depends on a number of factors, such as $N_{samples}$, SNR, baseline separation between antenna elements (d), and true AoA. Moreover, an equation has been derived to predict the standard deviation of the AoA. In addition, the proposed concept has been verified by the measurement results. The measurements were conducted in three different sites, such as on top of the roof of Eaton Hall at the University of Kansas, on top of the watch tower at Wells Overlook County Park south of Lawrence, KS, and at the Blue Valley park at Kansas City, MO. The measurement data was recorded with an oscilloscope at Eaton Hall and with the Software Define Radio (SDR) card at both Overlook park and Blue Valley park. The setup and the results from all the measurements are presented and discussed in this chapter. Furthermore, a comparison between simulated and measured results is conducted and analyzed for each measurement. This chapter ends with a discussion on the findings from the measurement results with an explanation about the discrepencies between the simulated and measured results.

The first measurement was conducted at the Eaton Hall at the University of Kansas, KS. The FM band signals were received by two antennas with similar characteristics. The matching between the characteristics of the antennas, such as S_{11}, radiation pattern, gain, and polarization

were crucial for achieving coherency between the received signals. The received signals from the two antennas were then passed to the oscilloscope where the signals were digitized and recorded. The recorded time-series data was then subjected to post-processing, such as FFT analysis in a separate computer. The block diagram of the setup is shown in Figure 5.1.

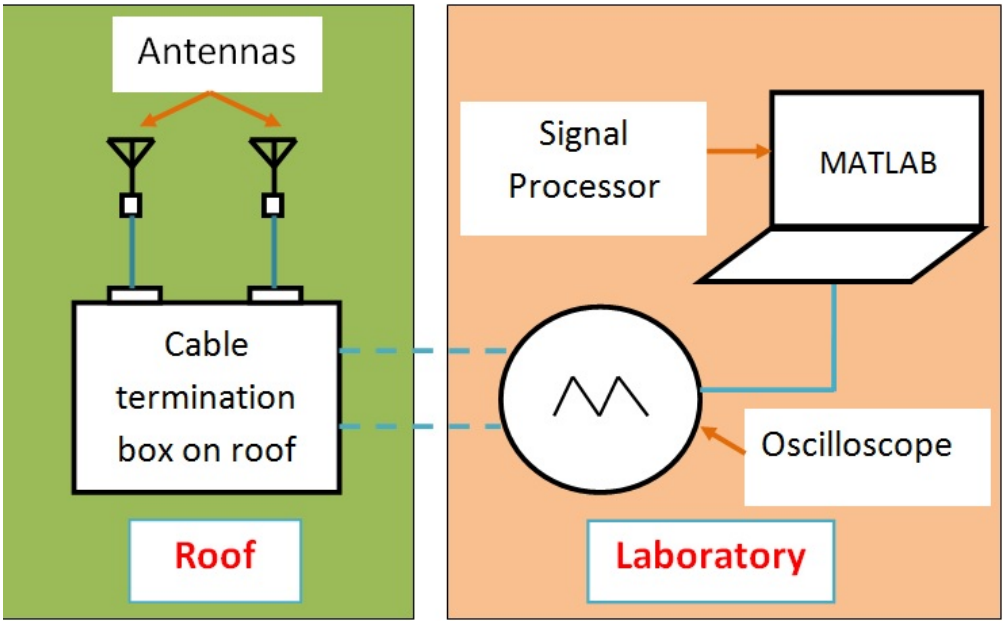

Figure 5.1: Block diagram of the measurement setup in the Eaton Hall.

The FM band antennas were mounted on top of the roof of the Eaton hall at the University of Kansas. Due to the unavailability of AC power on the roof, the oscilloscope was placed inside the laboratory at Eaton Hall. Two long co-axial cables were then installed from the roof to the laboratory. In the laboratory, the two cables were connected to the oscilloscope to record the time-series data received by the Rx antennas. The received data was then subjected to an FFT to produce the spectrum of the received signals.

In the second setup, a Software Defined Radio (SDR) card from Ettus Research with a model number B210 [100] was exploited to record and process the received signals instead of an oscilloscope.

In the first setup, the antennas were mounted on top of the roof of Eaton Hall in the vicinity of pre-existing antennas. Therefore, the pre-existing antennas were interfering with the Rx antennas. Moreover, the neighboring antennas were corrupting the phase measurement by incorporating multipath effect. Therefore, the second measurement was conducted outside University of Kansas at the Wells Overlook park that is just on the outskirts of Lawrence, KS. The exploitation of the oscilloscope during the second measurement was not possible due to the lack of the AC power supply at the measurement site. Therefore, an SDR card was utilized that runs on shared power drawn from the laptop through its USB port. The received signals from the Rx antennas were passed to the SDR card that is equipped with an integrated mixer, Local Oscillator (LO), and A/D converter. The processed signals from the SDR card were then subjected to spectral analysis (e.g. FFT), interferometry, and triangulation for position estimate. The block diagram of the setup is shown in Figure 5.2.

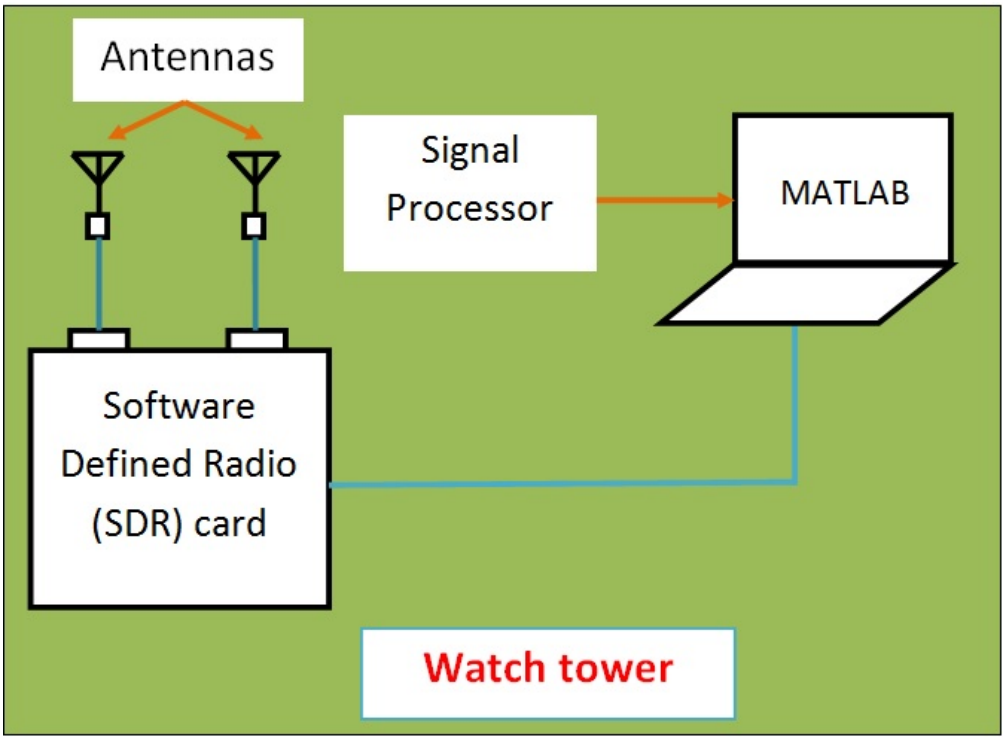

Figure 5.2: Block diagram of the measurement setup on top of the watch tower.

In the third measurement, the measurement site was carefully chosen to be able to provide su-

pertowers. Supertowers are towers that host more than one Tx station. The selection criterion of the measurement site was based upon two factors, such as multiple number of supertowers and the range between the supertowers and the measurement site being less than or equal to 30 km. Based on the selection criteria, different locations were searched in the Google Maps and finally, the Blue Valley Park in Kansas City, MO was chosen to be the measurement site. The locations of the measurement site with the available supertowers are shown in Figure 5.3.

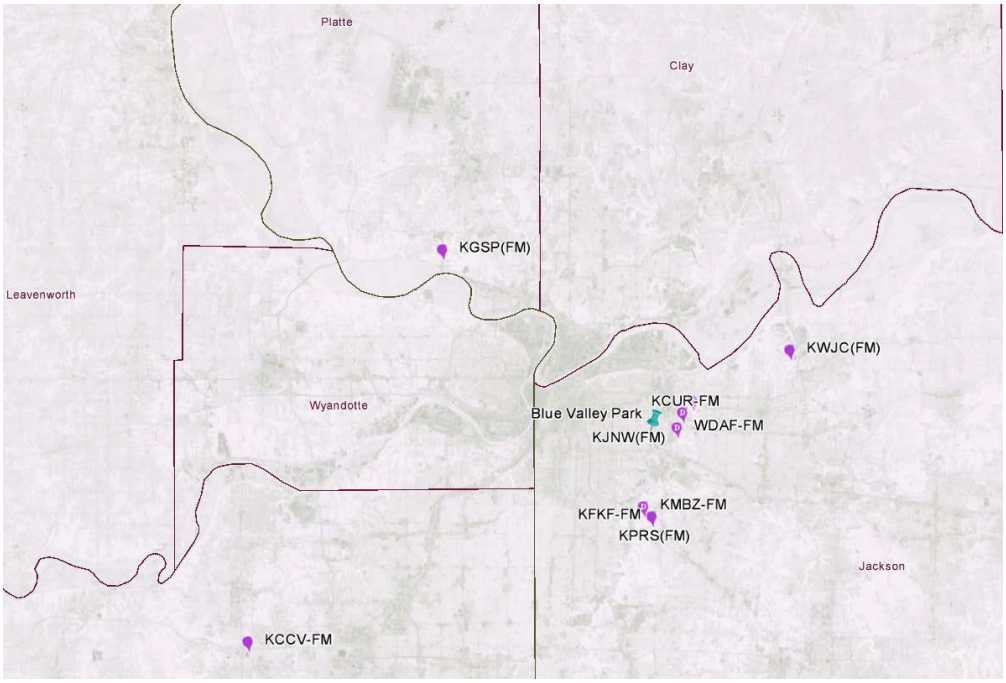

Figure 5.3: The location of the measurement site and the available supertowers.

In this experiment, the same setup from second measurement was used. However, the AoAs from one supertower were calculated for each Tx station located at that supertower. All of the AoAs from one supertower were then averaged and the average AoA was chosen to be the AoA for that tower. It will be shown that the supertower provides finer accuracy in position estimate.

The spectrum of the received signals consisted of multiple peaks across FM radio bands (88 MHz - 108 MHz). Each peak in the spectrum represented a transmitter station that was transmitting at a particular frequency within the FM radio band. It was shown in the previous chapter that the

triangulation method requires at least 3 strong signals from 3 spatially separated Tx stations to localize the receiver. Therefore, 3 strongest signals were chosen based on the signal strength (signal amplitude) from the spectrum. The chosen 3 strongest signals were spatially separated so that a triangle can be made with the 3 Tx stations. It is worth mentioning here that the co-ordinates of the Tx stations were a known priori. Thus the Tx stations were chosen to be separated both in space and in transmitting frequency. A detailed selection criteria for choosing Tx stations was presented in the previous chapter. Afterwards, the phase difference of the received signals at the two Rx antennas were recorded and a two-element antenna array interferomtry was applied to determine the AoA of the signals transmitted from the selected Tx stations. The three AoAs from the 3 Tx stations were then triangulated to localize the receiver.

The two antennas that were used in interferometry system possesed similar characteristics, such as reflection coefficient (S_{11}), radiation pattern in azimuth and elevation plane, and antenna gain. The reason being that the received power at the antennas are function of antenna parameters as shown in Equation (5.1).

$$P_r = P_t G_t G_r (\frac{\lambda}{4\pi R})^2 \tag{5.1}$$

It is shown in Equation (5.1) that the received power is a function of both of the Tx and the Rx antenna gain (G_t and G_r), wavelength at the Tx frequency (λ), and the free space distance between Tx and Rx (R). It should be noted here that $(\frac{4\pi R}{\lambda})^2$ is called Free Space Path Loss (FSPL). FSPL represents the attenuation of the transmitted power in the free space from the Tx antenna to the terminal of the Rx antenna [101]. Moreover, it is assumed in the calculation of the FSPL that the Tx and Rx antennas are matched in polarization. The commercial FM Tx stations are allowed to utilize horizontal or circular (both horizontal and vertical) polarization ([102]-[103]). The polarization of the transmitted EM wave by a particular FM radio stations is found in FCC information page [104]. The received signal power is maximum in the case of complete match in the polarization of the transmitted and the received signal. The Polarization Loss Factor (PLF) is

calculated by the Equation (5.2).

$$PLF = |cos\psi_p|^2 \tag{5.2}$$

Where ψ is the angle between the two unit vectors along the axes of the transmitted and the received signals [101]. In this measurement, the polarization of the transmitted signal was found to have both of the horizontal and vertical components [104]. The antennas that were employed as received antennas exhibited vertical polarization [105]. Therefore, the received signal should be 3 dB down compared to the received signal by a circularly polarized antenna.

5.1 Measurement with an Oscilloscope

The first measurement was conducted on top of the roof at Eaton Hall at the University of Kansas. The available FM band signals were captured by two Rx antennas and then passed to the oscilloscope. A detailed description of the measurement setup and the measurement results will be presented in this section.

5.1.1 Measurement setup with an Oscilloscope

In this setup, two identical antennas were mounted on top of the roof of the Eaton Hall at the University of Kansas. The separation between antennas was kept to be $52''$ that is $\frac{\lambda}{2}$ at the highest frequency of interest (108 MHz). The antennas were mounted on a styrofoam that has a dielectric constant of 1.03. Figure 5.4 shows the antenna setup on top of the roof of Eaton Hall.

An Agilent Digital Storage Oscilloscope (DSO) was used to record the time-series data received by the Rx antennas. The specifications of the DSO is provided in [106]. Due to the unavailability of the AC power supply on top of the roof, the oscilloscope was placed at the laboratory on the 3rd floor of the Eaton Hall. Two long cables were used to connect the Rx antennas to the oscilloscope. The lenghts of the two cables from the roof to the third floor laboratory was not equal. Therefore,

Figure 5.4: Antenna pair setup on top of the roof of Eaton Hall.

the cables were calibrated first to remove the phase difference that was introduced by inequality in the length of the cables.

A 2 way 0^{o} power divider from Mini-Circuits with a model number of ZX-10-2-12+ was employed in the calibration process of the cables from Rx antennas to the oscilloscope. The datasheet of the power divider was found in [107]. The calibration was conducted in two steps, such as verifying the accuracy of the two oscilloscope ports at the first step and then measuring the phase difference between two received signals at two oscilloscope ports. The major difference between the setup of the two steps being that of the position of the power divider. In both the steps, one signal was split in the power divider, fed into the oscilloscope ports, and then the phase differnece was measured at the two oscilloscope ports. However, the first step placed the power divider after the cable and the length of the two cables from the power divider output ports to the oscilloscope ports were matched exactly. There was only one signal coming through the conduit and thus eliminates

any phase difference introduced by the inequality in length of the cables. First, the output from one of the Rx antennas was fed to the input of the power splitter. The power splitter split the input signal equally (3 dB down) and then the signals were passed to the two ports of the oscilloscope. The setup is shown in Figure 5.5.

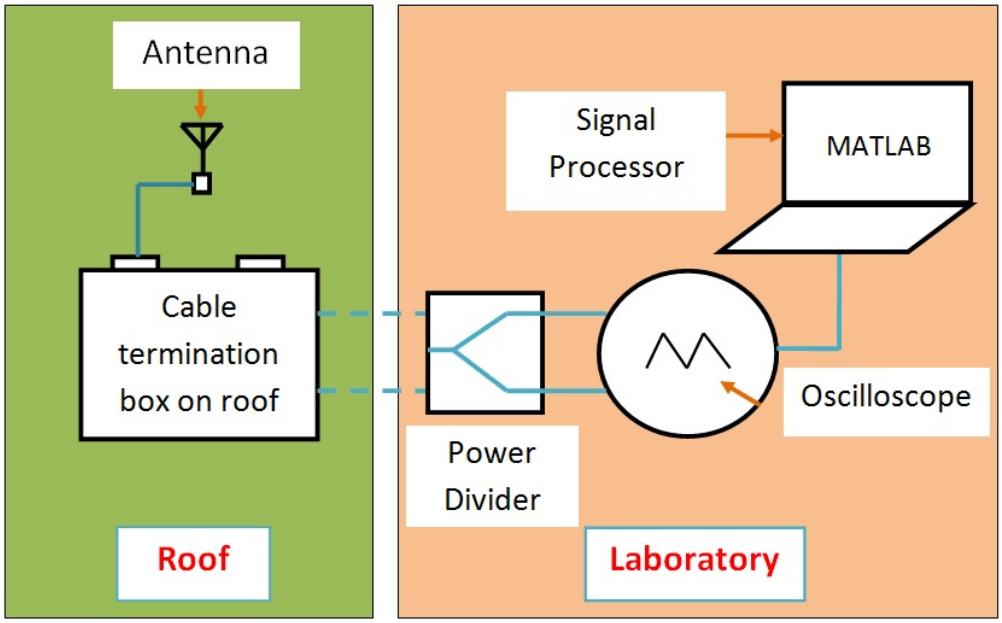

Figure 5.5: Block diagram of the setup to validate the accuracy of the oscilloscope ports.

The power divider was placed after the conduit and there was only one signal coming from top of the roof through the cable. Moreover, the output signals from the power divider experienced the same propagation delay through the power divider. Therefore, the delay between the signals at two oscilloscope ports should be zero. The measured delay between the two oscilloscope ports is shown in Figure 5.6.

It is shown in Figure 5.6 that the measured phase difference between two received signals was zero. Thus the accuracy of the oscilloscope ports was verified. In the second step, the power divider was placed before the cable. The input port of the power divider received the signal from one of the Rx antennas and then split the signal equally (3 dB down). The split signals were then fed to the oscilloscope ports through the conduits. The length of the cables in the conduit were not equal

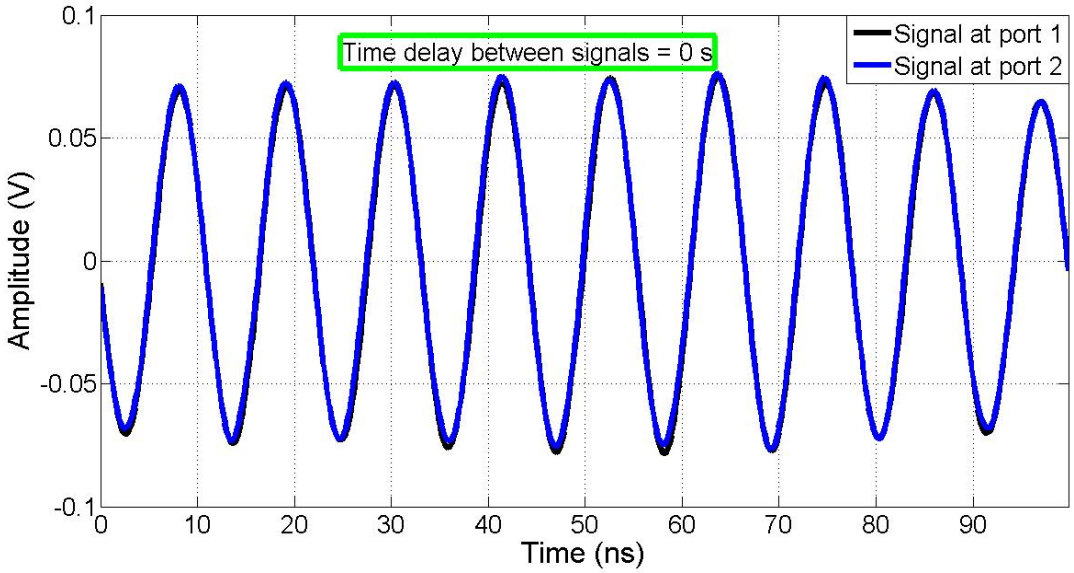

Figure 5.6: Phase difference between two received signals at two oscilloscope ports.

and thus the split signals experienced variable delay. The block diagram of the setup is shown in Figure 5.7.

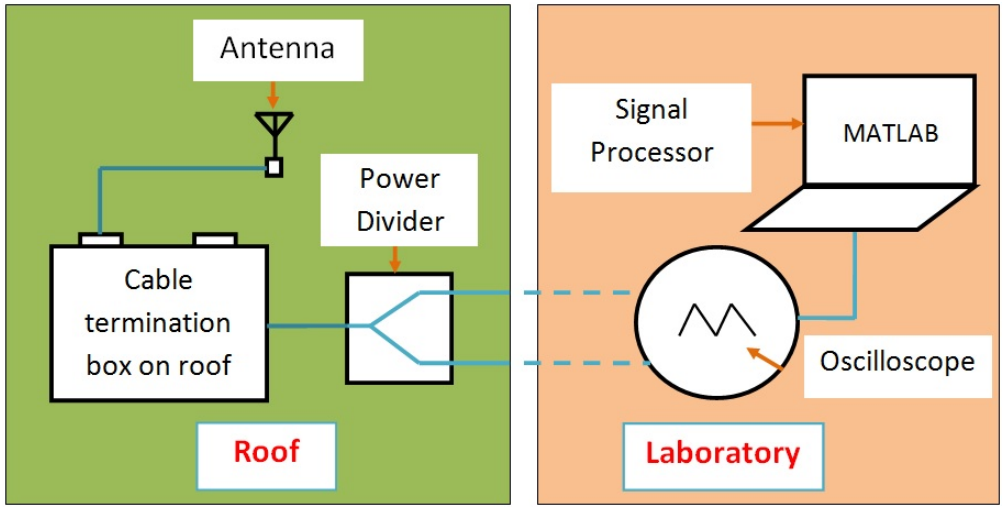

Figure 5.7: Block diagram of the setup to measure the phase difference between the two oscilloscope ports.

The lengths of the cables were not equal through the conduit and thus introduced a delay between the received signals. The measured delay between the received signals at two oscilloscope ports is

shown in Figure 5.8.

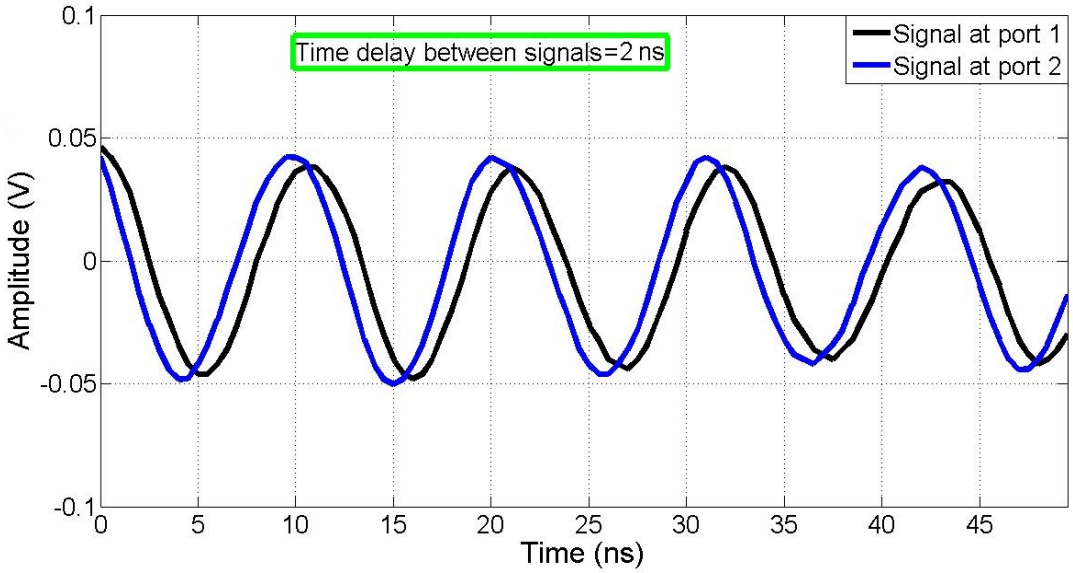

Figure 5.8: Phase difference between two received signals at two oscilloscope ports.

The measured phase delay was stored and then utilized to calibrate out the effect of inequality in cable lengths for the subsequent measurements. Next, both of the Rx antennas were employed to receive the available FM radio signals (88 MHz - 108 MHz). The signals received by the antennas were then passed to the oscilloscope ports. The time domain representation of the received signals is shown in Figure 5.9.

It is shown in Figure 5.9 that the received signals at the two ports exhibit a phase difference between them. The received signals were then subjected to FFT to find out the available spectrum of the FM radio signals. The highest freqeuncy of interest was 108 MHz and thus the sampling frequency needed to be at least twice the highest frequency of interest (108 MHz). The sampling frequency (f_s) was chosen to be 400 MHz. The separation between FM channels are 200 kHz. Thus the FFT length was chosen to be 2000 to achieve the required frequency resolution of 200 kHz as shown by the Equation (5.3).

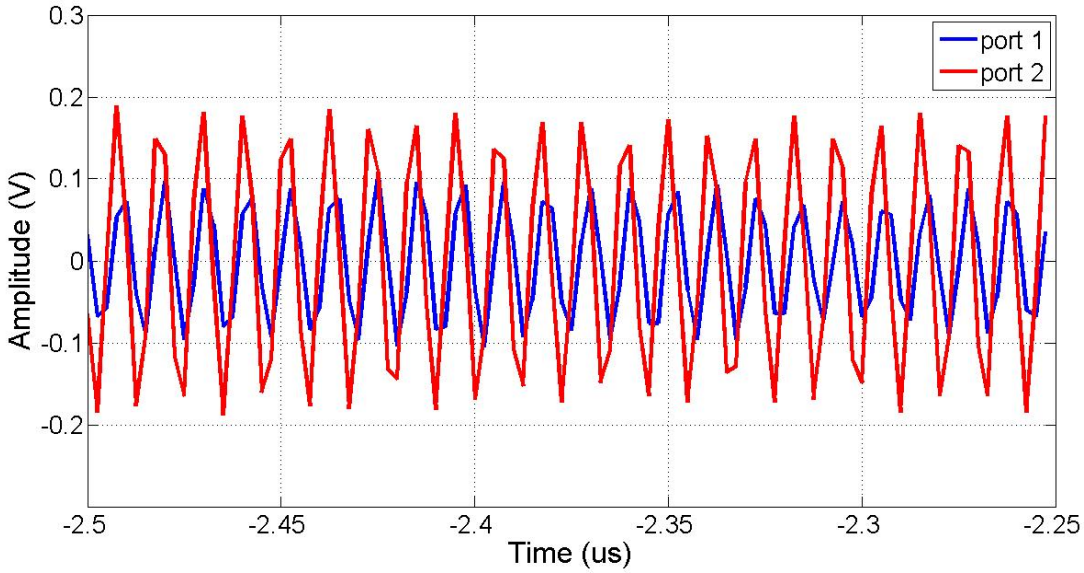

Figure 5.9: Received signals at two oscilloscope ports.

$$\Delta f = \frac{f_s}{N} = \frac{400\text{MHz}}{2000} = 200\text{kHz} \tag{5.3}$$

The spectrum of the FM radio frequencies that were received by one of the antennas is shown in Figure 5.10.

The proposed method estimates the position by triangulating AoAs from 3 spatially transmitters with SNR > 45 dB. However, due to the unavailability of 3 Tx signals with SNR > 45 dB, the three strongest signals were chosen from the spectrum, such as 88.1 MHz, 91.5 MHz, and 105.9 MHz. Moreover, it can be seen in Figure 5.11 that the aforementioned three stations were spatially separated to form a triangle.

5.1.2 Measurement results with an Oscilloscope

It has been mentioned in the previous section that the length of the cables from the Rx antennas to the oscilloscope were not equal. Therefore, the effect of the unequal cable lenghts were calibrated out to accurately measure the phase difference between the received signals. At first, one of the

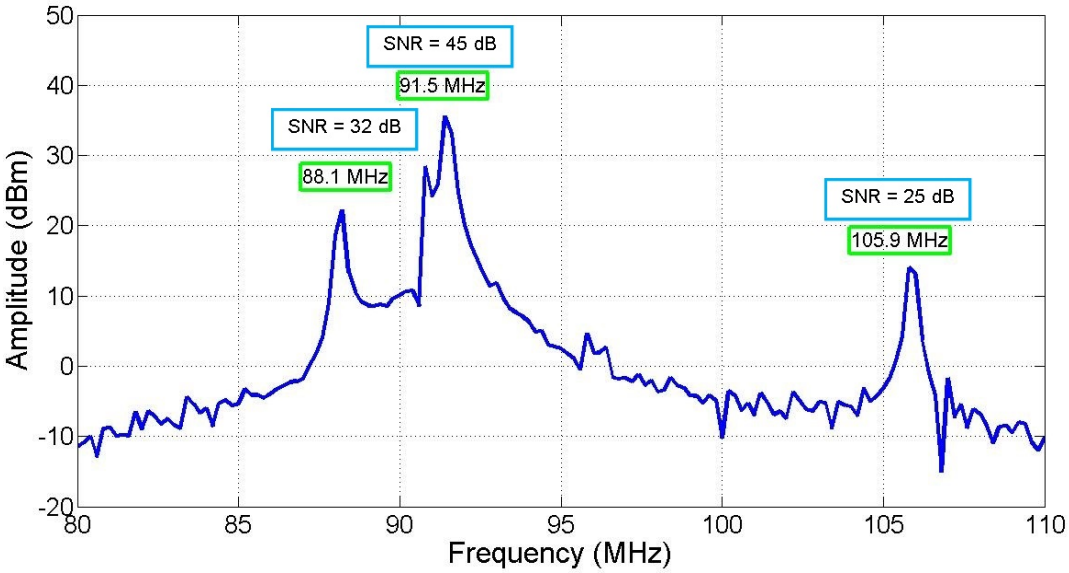

Figure 5.10: Spectrum of the received signals at one of the oscilloscope ports.

Figure 5.11: Position of the Rx and 3 Tx on the map.

two antennas was connected to the input port of a 2-way 0^o power divider and the two output ports of the power divider were terminated at the cable termination box on top of the roof. The cables were then connected to the oscilloscope through the cables in the conduit. The signal amplitudes in voltage at the two oscilloscope ports were then stored and transferred to MATLAB for further processing and analysis. In the MATLAB, an FFT of each signal was performed and the phase

difference of the two split signals was recorded. The phase difference between the received signals was then translated into time delay by the Equation (5.4).

$$\Delta\phi = \omega\Delta t \tag{5.4}$$

where $\Delta\phi$ is the phase difference in radians, ω is the angular frequency in radians/second, and Δt is the time delay in seconds. It has been previously noted that the Rx antennas were accompanied by pre-existing antennas on top of the roof at the Eaton Hall. The neighboring antennas were introducing the multi-path effect that corrupted the phase measurements at the Rx antennas. Therefore, the phase measurement was corrupted by the multipath effect. Moreover, the phase measurement was repeated for 100 snapshots with an average time interval between successive snapshots being 15 seconds. The purpose of measuring 100 snapshots was to reduce the uncertainty associated with the measurement. The measured phase differences are shown in Figures (5.12-5.14) for 88.1 MHz, 91.5 MHz, and 105.9 MHz respectively.

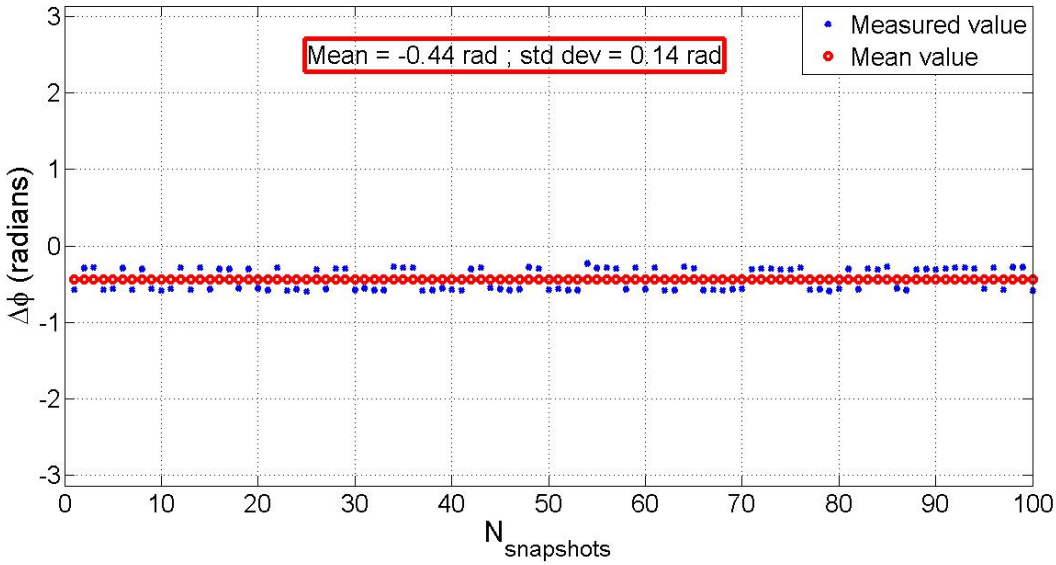

Figure 5.12: Calibrating out the cable lengths at 88.1 MHz.

In the next step, both of the Rx antennas were connected from top of the roof to the oscilloscope at the laboratory. The phase difference between the two received signals at the two oscilloscope

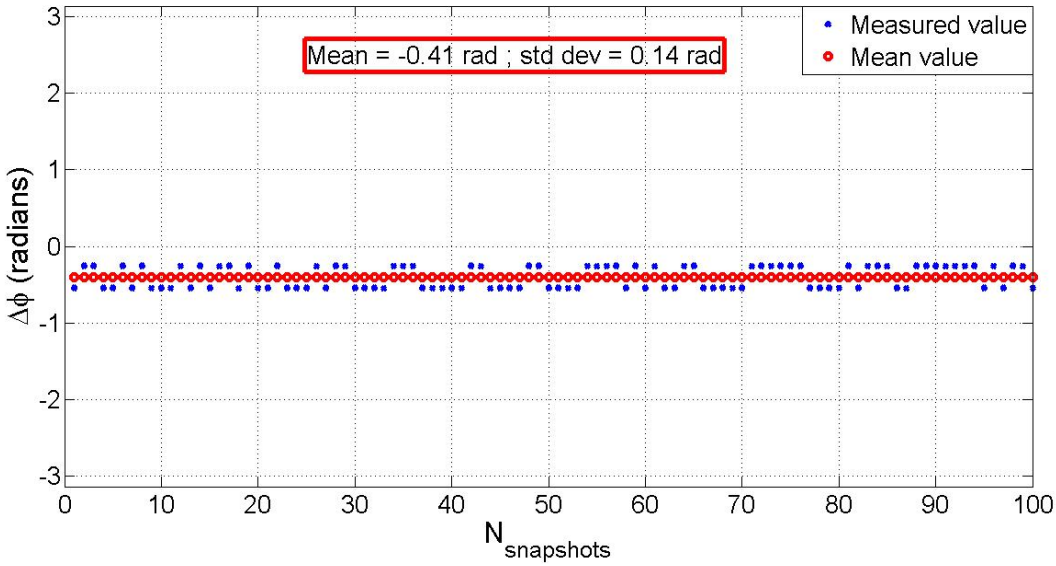

Figure 5.13: Calibrating out the cable lengths at 91.5 MHz.

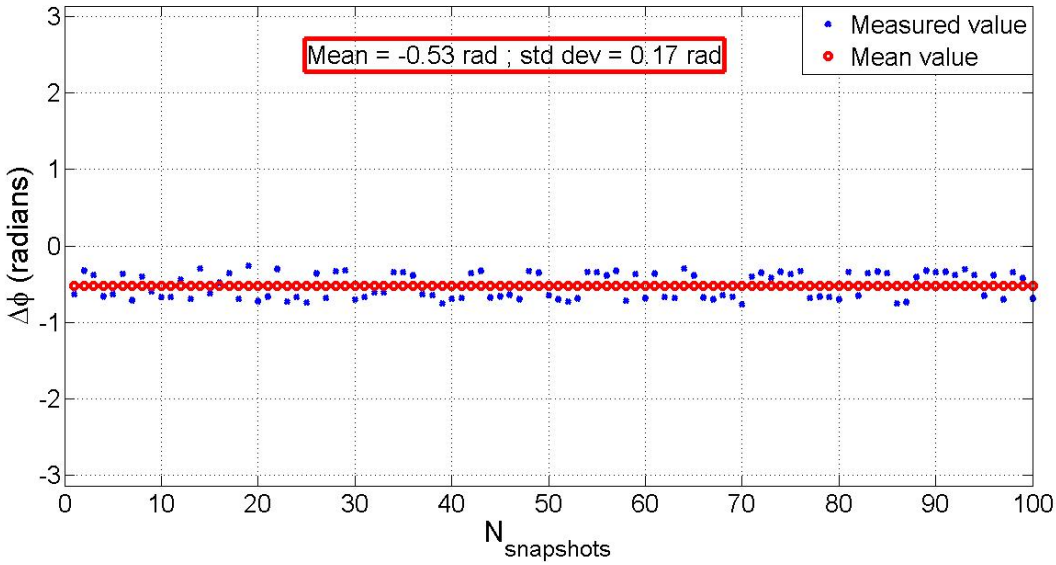

Figure 5.14: Calibrating out the cable lengths at 105.9 MHz.

ports was then calculated. Moreover, previously stored calibration data was applied towards phase difference calculation to calibrate out the effect of inequal cables between the Rx antennas and the oscilloscope. The corrected phase difference between the received signals are shown in Figures (5.15-5.17) at 88.1 MHz, 91.5 MHz, and 105.9 MHz.

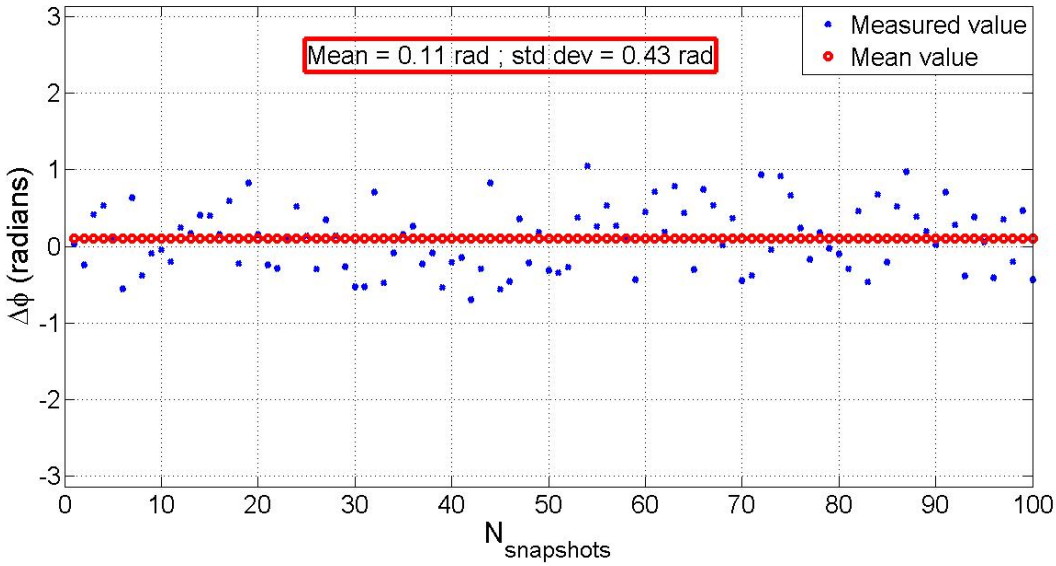

Figure 5.15: Variation in phase difference over snapshots for 88.1 MHz signal.

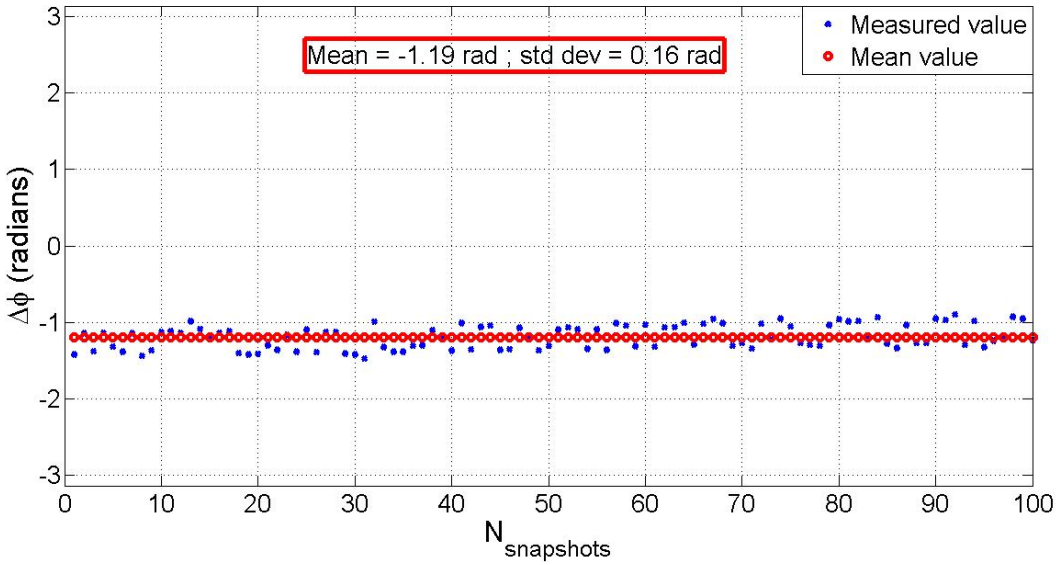

Figure 5.16: Variation in phase difference over snapshots for 91.5 MHz signal.

The measurement of phase difference between the received signals was conducted for 100 snapshots. The average time interval between successive snapshots was 15 seconds. Moreover, the setup was kept the same for the measurement during 100 snapshots. It can be seen in Figures (5.15-5.17) that the measured phase differences were tightly bound for signals with SNR > 45 dB

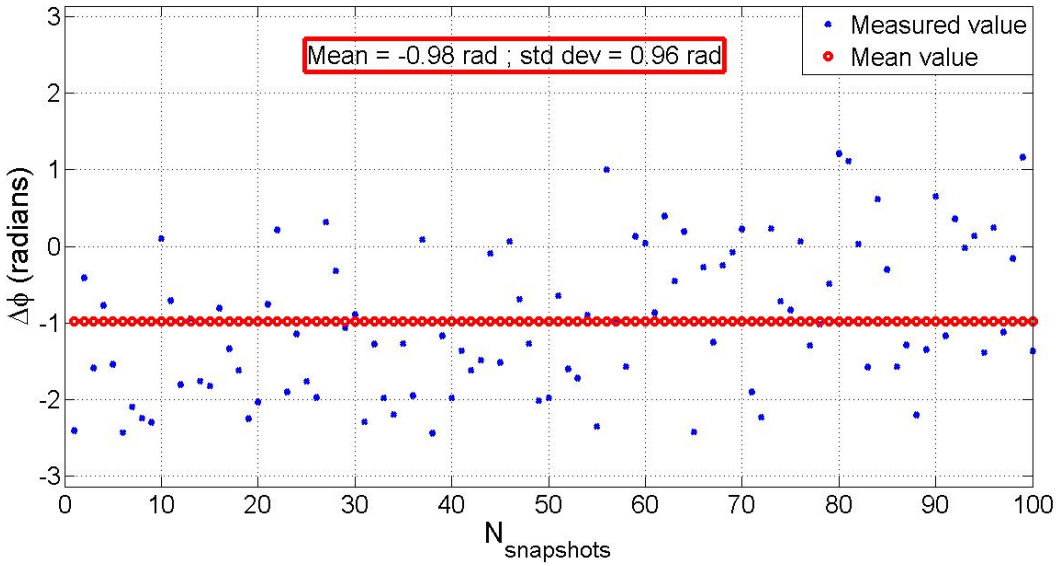

Figure 5.17: Variation in phase difference over snapshots for 105.9 MHz signal.

than the signals with SNR < 45 dB. The fact was indicated by lower value of $\sigma_{\Delta\phi}$ (0.16 rad) for signal with 45 dB SNR (91.5 MHz signal) and higher value of $\sigma_{\Delta\phi}$ (0.96 rad) for signal with 25 dB SNR (105.9 MHz signal).

The measured phase difference was then translated to the AoA of the Tx stations as shown in Figure 5.18.

The phase difference between the received signals failed to exhibit a constant pattern due to multi-path and SNR < 45 dB. Consequently, the AoA of the Tx signals varied significantly over 100 snapshots. The variation of AoAs over the 100 snapshots is more visible in polar format as shown in Figure 5.19.

Thus the measurement on top of the roof provided ambiguous results. In the next section, the measurement that was conducted away from the University of Kansas will be explained. The measurement site was chosen carefully to reduce multi-path effect and increase SNR. It will be

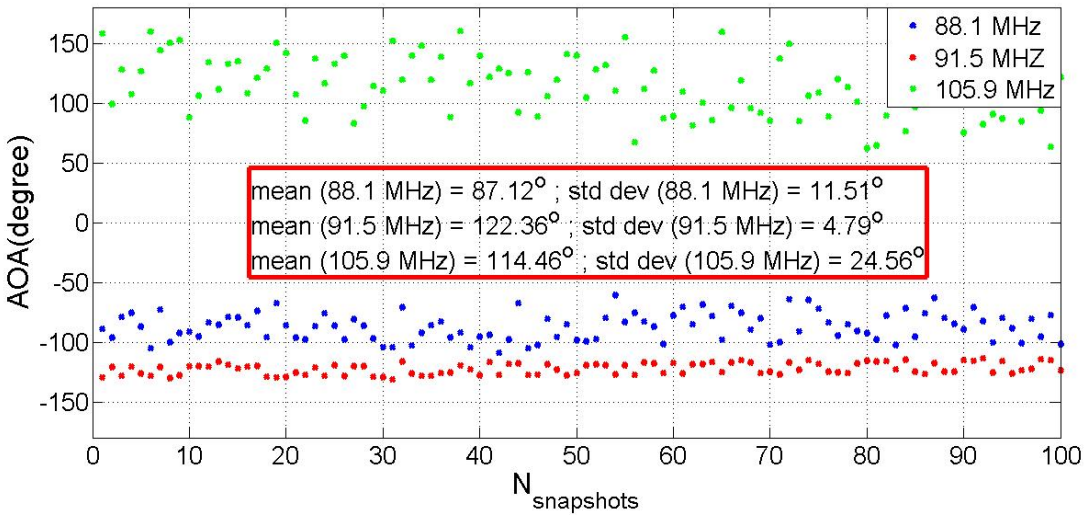

Figure 5.18: AoA of the Tx signals.

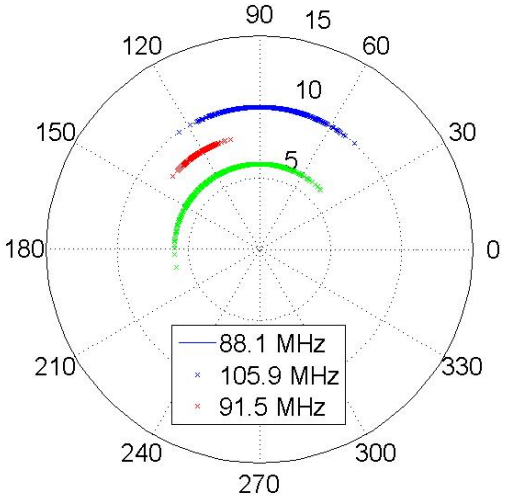

Figure 5.19: Variation of AoA of the Tx signals.

shown in the next section that reduced multi-path effect and higher SNR of the Tx signal provides more accurate results.

5.2 Measurment with SDR card

The position estimate accuracy of the proposed method relies on the accurate AoA estimation of the Tx signals. Moreover, the AoA accuracy depends on the accurate extraction of the phase difference between received signals at the two Rx antennas. However, the measurement on top of the roof at Eaton Hall lacks in accurate extraction of the phase difference between the Rx antenna terminals due to multipath and scattering from the adjacent antennas as well as SNR being less than 45 dB. Therefore, a different set of measurements were conducted in Wells Overlook County Park that provided a lower number of scatterers compared to that of the Eaton Hall. Moreover, the Wells Overlook County Park exhibits a raised watch tower and thus provided a good Line of Sight (LoS) for receiving signals from the Tx towers. In this section, the measurement setup at watch tower will be described. Moreover, the obtained measurement results will be presented and analyzed.

5.2.1 Measurement setup with SDR card

The setup at Wells Overlook County Park is shown in Figure 5.20.

The utilization of DSO was out of scope due to the unavailability of AC power supply at the measurement site. Instead an SDR (Software Defined Radio) card was used to downconvert and digitize the RF signals received by the pair of antennas. The SDR card was obtained from Ettus Research group with the model number B210 [100]. An SDR card is an embedded radio communication system that implements a receiver with the help of software instead of hardware. The SDR card was equipped with a tunable LO (Local Oscillator), mixer, and ADC. Furthermore, the SDR card shared the required input power through USB interface from the Laptop. A snapshot of the B210 SDR card from Ettus Research is shown in Figure 5.21.

The B210 SDR card contains 2 Tx and 2 Rx ports with fully-coherent 2×2 MIMO (Multiple In-

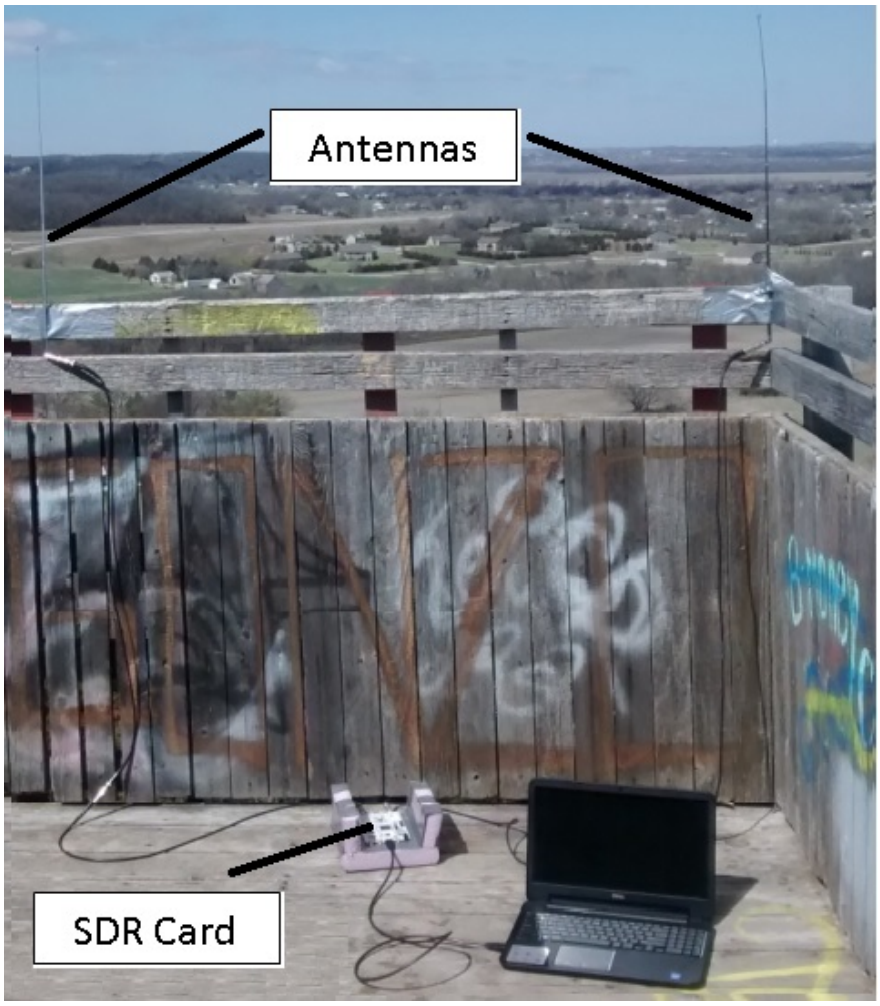

Figure 5.20: Antenna pair setup on top of the watch tower.

put Multiple Output) capability. The coherency between the Rx ports is an essential feature for extracting accurate phase diffference between the received signals. Moreover, the SDR card covers RF frequencies from 70 MHz to 6 GHz with a bandwidth of maximum 30.72 MHz in 2×2 MIMO mode. Thus the B210 SDR card was an ideal candidate for this project. Besides, the B210 board comes with a AD9361 chip that performs the function of ADC and DSP. A schematic of the AD9361 chip is shown in Figure 5.22.

The proposed technique employs the dAoAs of the Tx signals for position estimate. The AoAs of the Tx signals were calculated from the phase of the received signals. The phase of a signal can

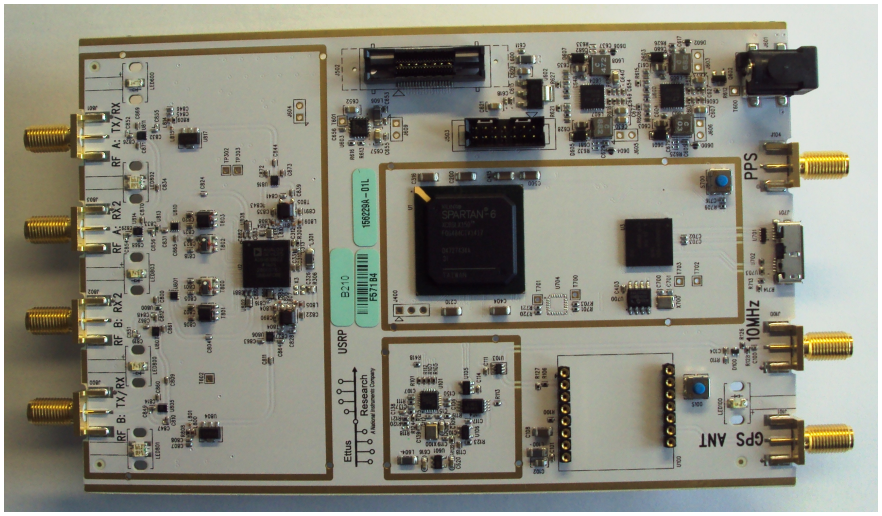

Figure 5.21: A picture of B210 SDR board from Ettus Research.

be obtained in two methods. In the first method, an accurate signal is used as the reference signal and the received signal is compared to the reference signal. The phase difference between the two signals are then employed to calculate the AoA of the received signal. In the second method, two spatially separated receiving sensors are employed to receive the signal. Then the phase difference between the two received signals are utilized to calculate the AoA of the received signal. The B210 board is equipped with 2 fully coherent MIMO capable ports. Therefore, measurement for extracting the phase difference was conducted based on the second method. Two FM band antennas were used as the receiving sensors.

The receiving antennas were connected to the Rx ports of the SDR card. The specification of the antennas are given in [105]. Both of the receiving antenna elements were chosen to be of similar characteristics in terms of return loss, radiation pattern, polarization, and gain. The received signals at the Rx antennas entered the two coherent Rx ports of the SDR card. The coherency between the Rx ports of the SDR card was crucial for accurate phase difference measurement between the two Rx ports.

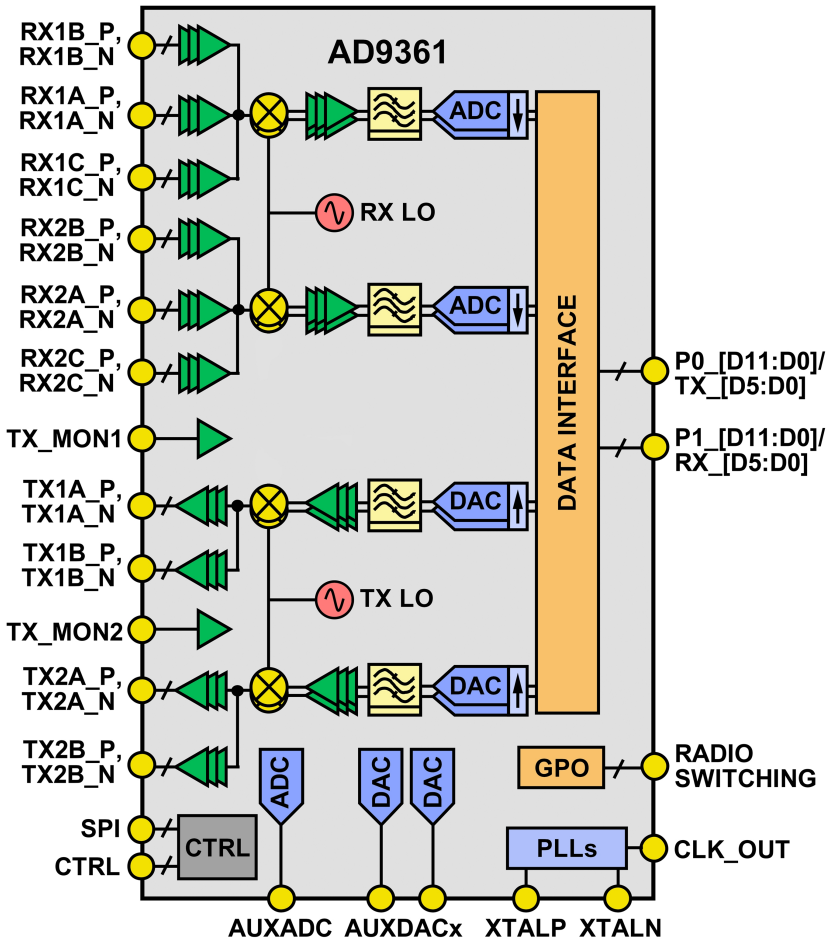

Figure 5.22: The schematic of the AD9361 chip of B210 SDR board.

5.2.2 SDR card configuration

The SDR card was configured with the GNU Radio Companion (GRC) interface. GRC is a graphical user interface to build GNU radio flow graphs or the software circuits. The GNU radio flow graph enables the SDR card to receive signals from the two antennas, spectrally isolate them, and then calculate the phase difference between the received signals. The flow graph or the software circuit that was used to receive two signals at the two ports is shown in Figure 5.23.

The GRC flow graph consists of blocks with each block representing a software circuit component. Each block is equivalent to a software module and performs a specific task. A simple representa-

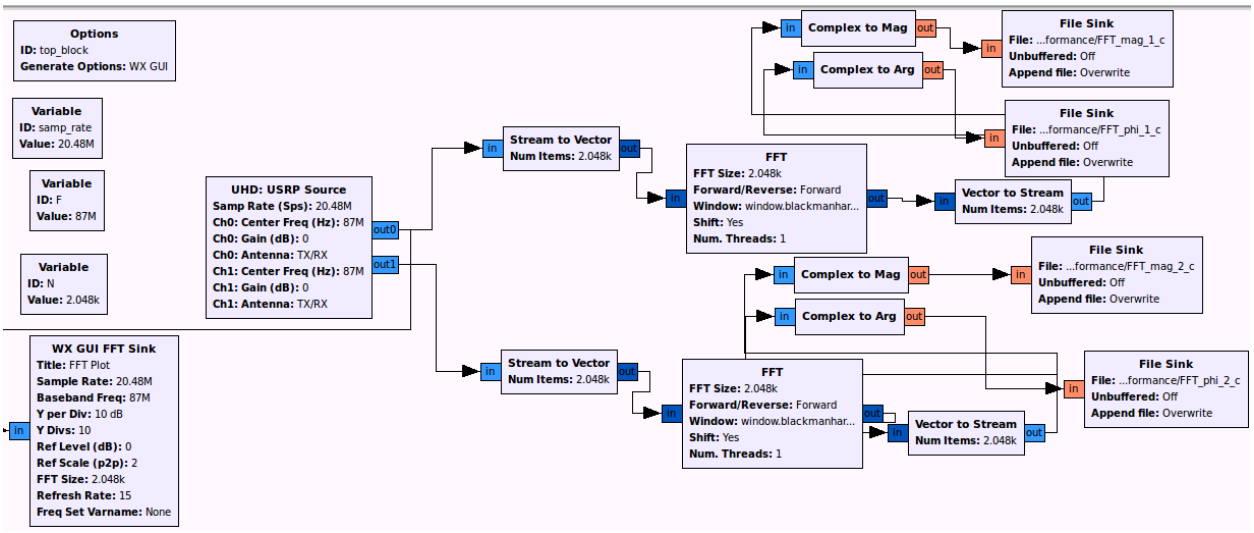

Figure 5.23: GRC flowgraph for SDR card to receive two signals at two ports.

tion of the above GRC flowgraph is shown in Figure 5.24.

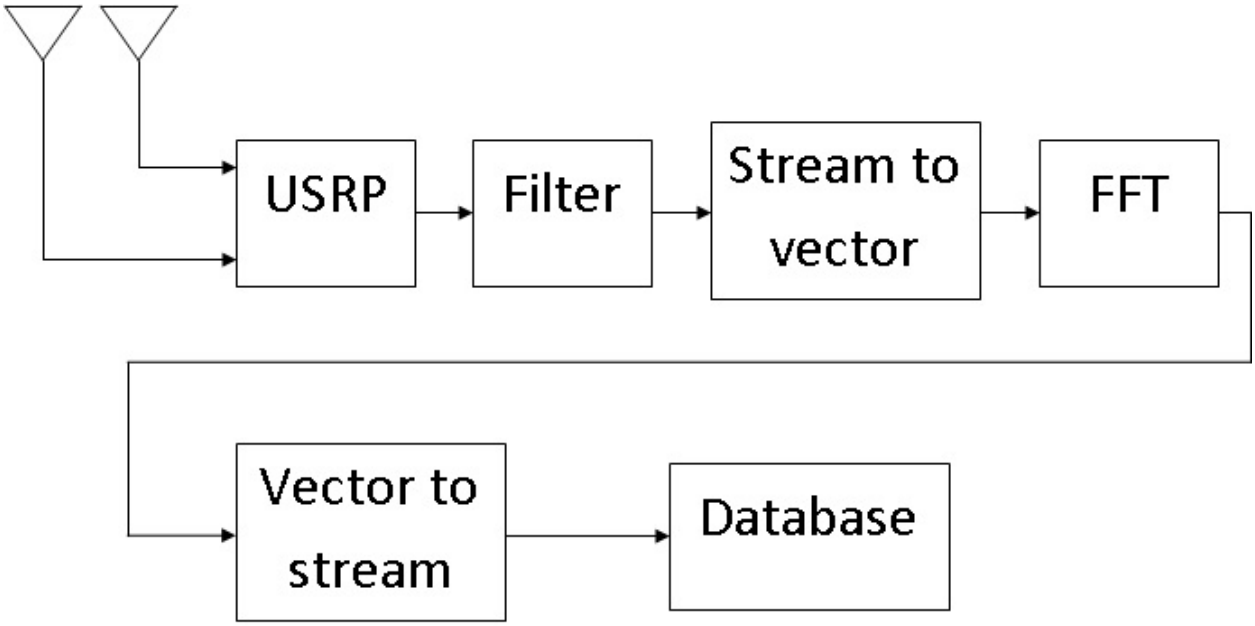

Figure 5.24: Simplified GRC flowgraph.

A brief description of the blocks will be given in this section. A complete description of all of the blocks can be found in [108].

5.2.2.1 USRP and filter

The USRP (Universal Software Radio Peripheral) source block is the interface block between the SDR card and the GRC flow graph. The two TX/RX ports of the Ettus B210 SDR card were used to receive the signals from the two antennas and the two ports were defined at this block. Moreover, this block performs the basic filtering and rejects the out-of-band signals. The down-conversion of the receiving signals from RF band to baseband was executed in this block as well. The LO frequency was chosen to be 87 MHz for the lower RF frequency band and 97 MHz for the upper frequency band. It is worth mentioning here that the full span of FM band signals (88 MHz - 108 MHz) could not be received by a single sweep of the SDR card. The limitation stems from the maximum sampling rate of the SDR card in the 2×2 MIMO mode. In this mode, the maximum sampling rate was 30.72 MHz and according to the Nyquist criterion, the maximum bandwidth of the received signal could not exceed 15.36 MHz. Therefore, the sampling rate was chosen to be 20.48 MHz and the measurement was performed with two different LO frequency settings. In the first setting, LO frequency was set to 87 MHz and FM band signals from 87 MHz to 97 MHz were received. In the next setting, LO frequency was set to 97 MHz and FM band signals from 97 MHz to 107 MHz signals were received. The received signals were then passed to the next block to be prepared for FFT.

5.2.2.2 Stream to vector

This block converts the received waveform to an array of time domain samples. This function is essential for performing time domain to frequency domain translation or FFT. The "Num Items" parameter in this block refers to the FFT length. The FFT length was chosen to be 2048. The frequency resolution is then calculated as the ratio of sampling rate to FFT as shown in Equation 4.1.

5.2.2.3 FFT

This block converts the received data from time domain to frequency domain. As mentioned in the previous section, the The sampling rate of the A/D converter was chosen to be 20.48 MHz and FFT size was chosen to be 2048. Therefore, the frequency resolution was 10 kHz. It should be noted here that the channel separation between the FM band signals is 200 kHz. Thus, it can be argued that the required frequency resolution was 200 kHz to extract the phase of the received signal. However, the signal energy density in the 200 kHz band is not uniform and therefore, 10 kHz frequency resolution was found to provide the highest density of signal energy.

5.2.2.4 Vector to stream

This block converts the array of time domain samples to continuous data stream.

5.2.2.5 Database

The SDR captures the complex data in raw binary format. The complex data was converted into polar data format (magnitude and phase). Both the magnitude and phase data were saved in binary format and were ready to be processed for post-processing.

The FFT was performed using 2048 samples. It was shown in Chapter 3 that the accuracy of the position estimate gets finer when averaged over 1000 snapshots. Therefore, the measurement was performed for a duration to receive more than 2048 $\times$ 1000 samples. The SDR card was not equipped with on-board memory to store the data. The data was transferred to the Laptop hard-drive using USB 3.0 interface. The average rate of storing data was 900 snapshots/s i.e. (900 $\times$ 2048) samples/s. An accurate position estimate requires averaging at least 100 snapshots. Therefore, the maximum position update rate is 10 Hz. However, the accuracy of the position estimate increases with increasing the number of snapshots.

5.2.3 Post processing of the received data

The received data from the SDR card was then analyzed for extracting the phase information. MATLAB software was utilized to read the binary data and for post-processing. The phase information was extracted from the received data and phase difference was calculated. The measured phase difference was then used to calculate AoA of the Tx signals, dAoA, and position estimate.

It should be noted here that the FFT provided 20 frequency bins for each of the Tx signals. The 20 frequency bins were resulted from the fact that the FM channel bandwidth is 200 kHz and the frequency resolution was chosen to be 10 kHz. The phase information was extracted from the frequency bin with highest SNR for each Tx signal. A more accurate method for selecting the correct frequency bin will be presented later with introducing the concept of supertower.

In this section, the SDR card setup was described. Moreover, the setup of the GRC flowgraph or software circuit has been explained. In the next section, the measurement results obtained using the SDR card will be presented.

5.2.4 Measurement results with SDR card

The SDR card was used to receive the spectrum of the FM band radio signals on the watch tower at Wells Overlook County Park. It should be noted here that the data from SDR card was not radiometrically calibrated. Therefore, the received spectrum by the SDR card was calibrated by capturing the spectrum with the SDR card and a Spectrum Analyzer (SA) at the same location at the same time. The Resolution Bandwidth (RBW) of the SA was kept to be 10 kHz. It was found out that the received signal by the SDR card exhibited an amplitude offset of 52 dB with respect to the received signal by the SA. The received spectra by the SA and the SDR card (calibrated) are shown in Figures (5.25-5.27). The call signs, center frequencies, and measured SNRs of each station are shown in the box above the corresponding signals.

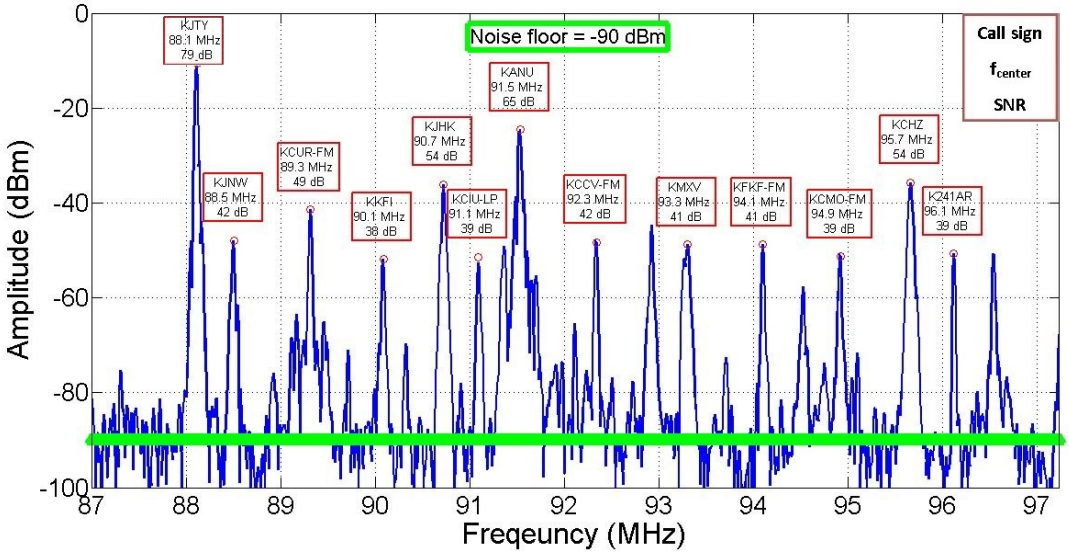

Figure 5.25: Spectrum of the lower FM band received signals by the SDR card.

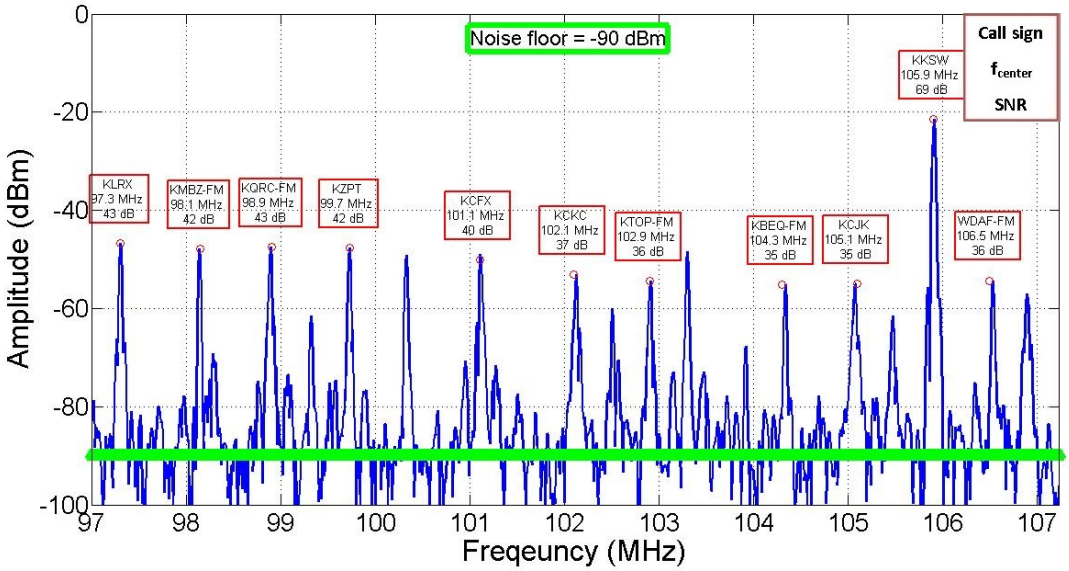

Figure 5.26: Spectrum of the upper FM band received signals by the SDR card.

It can be seen in Figures (5.25-5.27) that the SNRs of the received signals by the SDR card and the SA are similar to each other. It was mentioned in the previous section that the frequency resolution during the FFT of the signals received by the SDR card was chosen to be 10 kHz. Thus the spectrum of the received signals by the SA and the SDR card should be similar to each other.

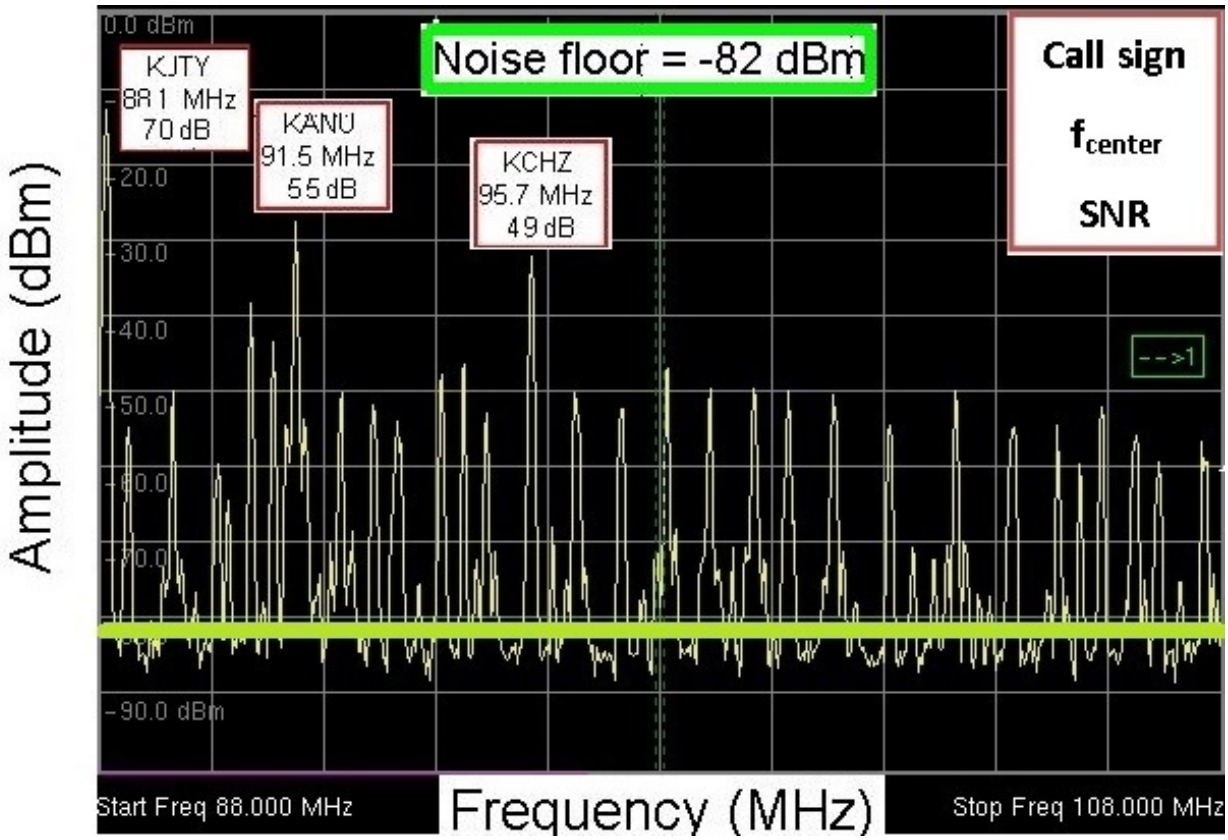

Figure 5.27: Spectrum of the FM band received signals by the Spectrum Analyzer.

Moreover, the received power from the Tx transmitters were calculated by Friis Transmission Equation as shown in Equation (2.2). The calculated received powers from transmitters with center Tx frequencies of 88.1 MHz, 91.5 MHz, and 95.7 MHz were calculated to be -3 dBm, -20 dBm, and -22 dBm respectively. It is worth mentioning here that the FM transmitters transmit in circular polarization and the used receive antennas were linearly polarized. Therefore, the received power was at least 3 dB lower than the transmitted power. However, the noise floor of both the SDR and the SA exhibited a higher value than the calculated thermal noise of -123 dBm. Therefore, it is evident that the noise floor was elevated by the external noise. Besides, the total noise that affects a radio receiver depends on the environment noise, the receiver thermal noise, and the antenna loss characteristics [109]. The total noise of the receiver, as shown in [109], can be represented by the Equation (5.5).

$$N = 10log_{10}(kT_oB) + 10log_{10}(\eta(f_a - 1) + f_r) \tag{5.5}$$

where N is the noise power in dBW, T_o is the reference temperature in Kelvin, B is the effective noise bandwidth of the measurement in Hz, η is the antenna radiation efficiency, f_a is the external noise factor, and f_r is the receiver noise factor with respect to the base of the lossy antenna. It is shown in [109] that the median value of the man-made external NF varies between 20 and 25 dB across the FM radio frequency band.

It has been demonstrated in the previous chapter that at least 3 spatially separated Tx stations are required to estimate the position by triangulation. Furthermore, the Tx positions play an important role in the accuracy of the position estimation. The details of the transmitter selection algorithm has been explained in the previous chapter. Based on that knowledge, 3 Tx stations were chosen, such as 88.1 MHz, 91.5 MHz, and 95.7 MHz from the spectrum of the received signals at the Wells Overlook County Park. Then the phase differences were measured for each of the 3 Tx stations. To reduce the effect of any natural or man-made random noise that can deteriorate the measurement accuracy, the phase difference measurement result were obtained for 1000 snapshots. Figure 5.28 shows the measured phase differences for each of the three transmitters for 1000 snapshots.

It is evident from Figure 5.28 that the phase differences between the received signals for each of the 3 Tx stations were bound tightly with a lower σ value compared to that one obtained on roof of the Eaton Hall. Therefore, the obtained measurement results in this setup were used to calculate the AoA and position estimate. The phase differences were then translated to the AoAs of the transmitting signals. However, the proposed method provides the position estimate independent of the orientation of the antennas. Therefore, measured dAoAs of the Tx stations were compared to the true dAoAs that were calculated from geometry. The comparison results are shown in Figure 5.29.

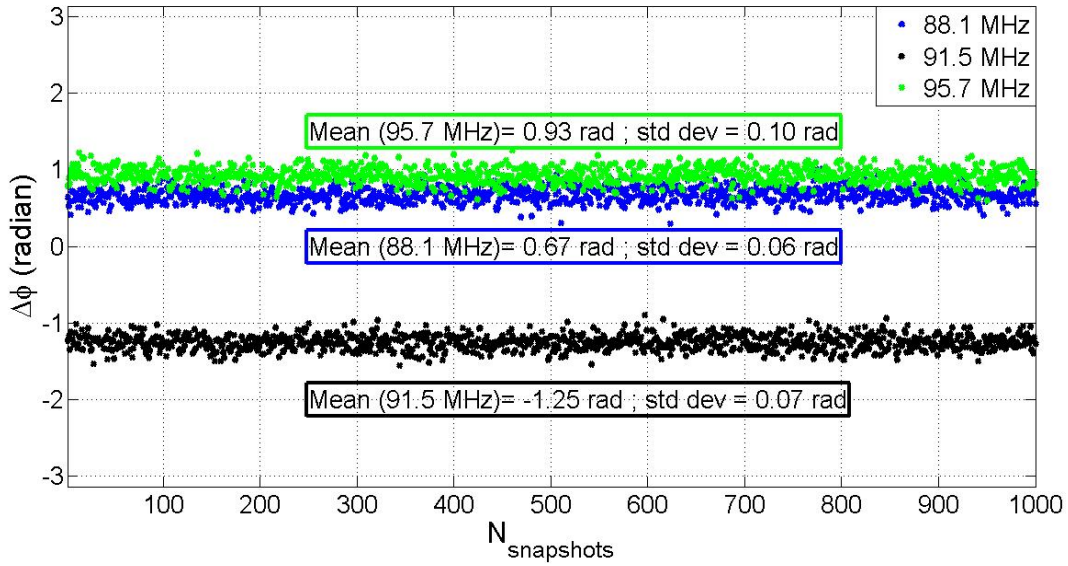

Figure 5.28: Measured phase differences between the 3 received Tx signals for 1000 snapshots.

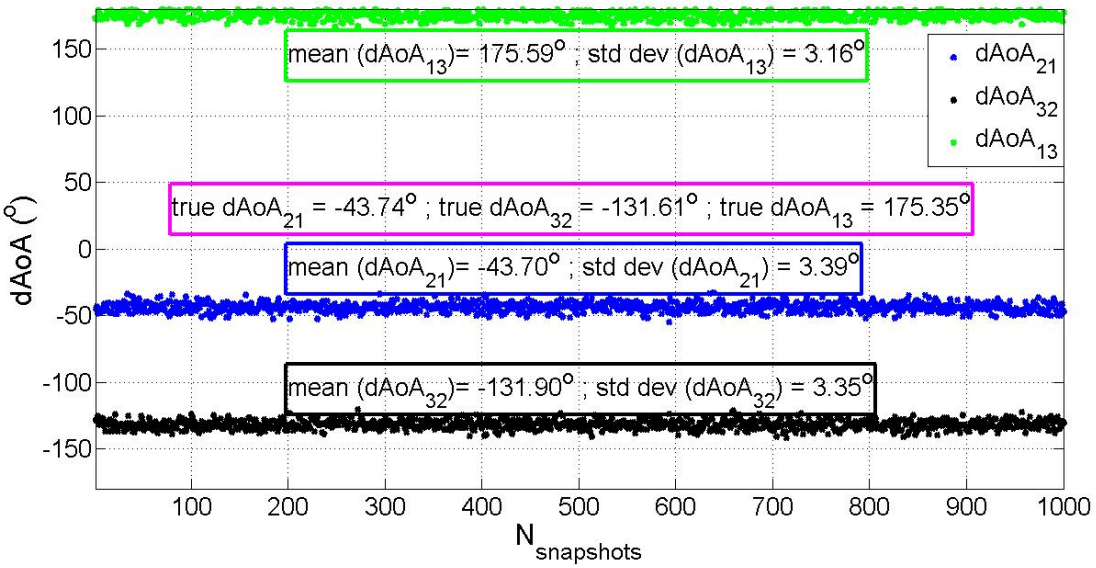

Figure 5.29: dAoAs between 3 Tx stations for 1000 snapshots.

It is shown in the Figure 5.29 that the mean of the measured dAoAs and the calculated dAoAs agree to each other. The measured dAoAs were then translated to position estimation and the mean of the position estimate was compared to the true position of the receiver that was collected by GPS.

The measured phase differences and the calibrated dAoAs were utilized in 3 different ways to estimate Rx position. In the first way, the phase difference from 1000 snapshots were transferred to 1000 dAoA measurements and the 1000 dAoA measurements were translated to 1000 position estimate. Then the mean of the 1000 position estimate was found and the error between the measured and true position was denoted by ε_{μ_pos}. In the second way, 1000 dAoAs were calculated from 1000 phase difference measurement results and then the mean of the 1000 dAoAs was calculated. Then the mean value of the dAoA was used for position estimate. The error between the measured position estimate and the true position was denoted by ε_{μ_dAoA}. In the third way, the mean of the 1000 phase difference measurements was calculated first and then the mean value was used to calculate a single value for dAoA as well as a single value for position estimate. The resultant error was denoted as $\varepsilon_{\mu\_\Delta\phi}$. It should be worth mentioning here that 2 trials have been performed to validate the measured results. A single trial consists of received signals data worth of 1000 snapshots and (1000×2048) samples. A comparison between the errors derived from the aforementioned algorithm is shown in Table 5.1.

Table 5.1: Comparison of the position estimate errors between the 3 methods from 2 trials.

Methodology	$\varepsilon_{\textbf{position\_estimate}}$ (trial1)	$\varepsilon_{\textbf{position\_estimate}}$ (trial2)
ε_{μ_pos}	$27.63m$	$28.2m$
ε_{μ_dAoA}	$26.14m$	$27.73m$
$\varepsilon_{\mu\_\Delta\phi}$	$22.33m$	$24.51m$

The transformation between the phase differences, the dAoAs, and the position estimation is not a linear process and thus the error terms were different from each other as expected. Moreover, it is evident from the Table 5.1 that the least error occured when the mean of the measured phase differences was used for position estimate. The reason being that the averaging of the phase differences reduced the impact of outliers in the first stage of the measurement calculation.

The accuracy of the position estimate was further improved by filtering the measured phase differences. The standard deviation (σ) of the 1000 measured phase differences was calculated and the

measured values that were outside σ were discarded. The resultant measured phase differences are shown in Figure 5.30 with 320 data being discarded.

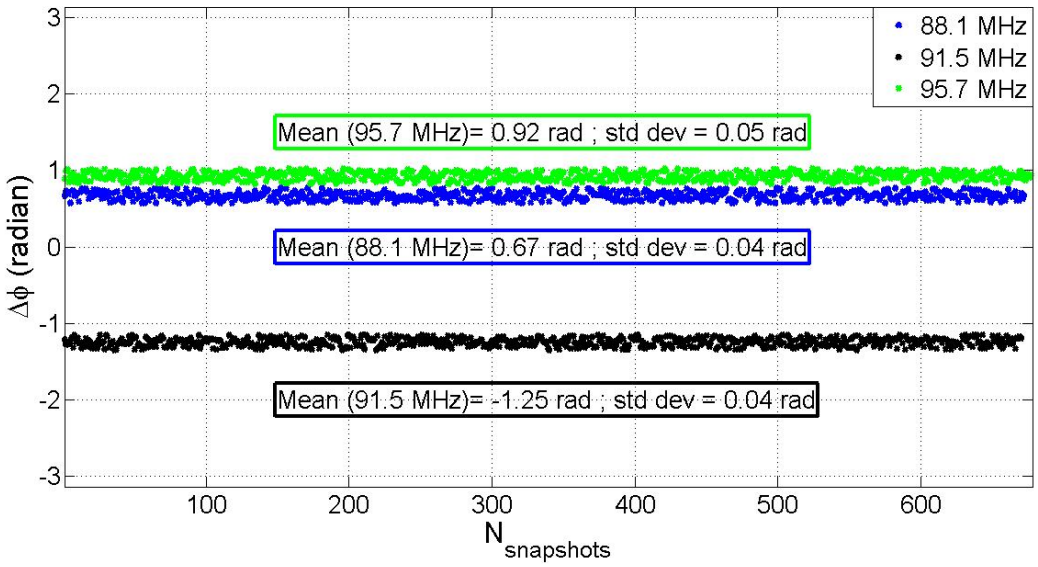

Figure 5.30: Measured phase differences between the received signals after filtering.

The mean of the measured phase difference was then used to calculate the dAoA and the position estimate. The errors of the position estimate were found to be 16.4 m and 19.75 m for the two trials. The error between position estimates before and after filtering are shown in Table 5.2.

Table 5.2: The position estimate errors before and after filtering.

Methodology	$\varepsilon_{\textbf{position\_estimate}}$ (trial1)	$\varepsilon_{\textbf{position\_estimate}}$ (trial2)
Before filtering	$22.33m$	$24.51m$
After filtering	$16.4m$	$19.75m$

In this section, the measurement setup with SDR card was discussed. Moreover, the configuration of SDR card with GRC flowgraph was explained. The building blocks of the GRC software circuit were described. Furthermore, the measurement results with the SDR card were presented with and without filtering the raw data.

In this measurement, the AoA was calculated from the phase difference extracted from the frequency bin with highest SNR. However, the frequency bin with highest SNR does not ensure the most accurate phase information. Therefore, the utilization of supertower has been proposed in this dissertation. The supertower is defined as the tower that hosts multiple Tx stations operating with different frequencies. The advantage of utilizing supertowers will be described in the next section. Moreover, the algorithm for finding the most accurate frequency bin will be developed. The measurement results obtained from utilizing supertower will be presented.

5.3 Measurement with SDR card utilizing supertowers

The AoA measurement accuracy depends on the accurate phase difference measurement. Signals with high SNRs provide more accurate phase difference measurement results. However, The SNR of the received signal was not uniform across the channel bandwidth of 200 kHz. Therefore, the frequency resolution was chosen to be 10 kHz during FFT. Then the frequency bin with highest SNR value was utilized to extract the phase difference information. However, the frequency bin with highest SNR does not ensure the most accurate phase difference measurement result. Therefore, an algorithm has been presented in this section to localize the frequency bin with the most accurate phase information.

5.3.1 Algorithm for finding the optimum frequency bin

The AoA of the Tx station was calculated from the phase difference between two received signals. The accuracy of the phase difference measurement depends on the coherency between the received signals. The measured phase difference is then used to calculate the AoA of the Tx signal as shown in Equation (5.6).

$$AoA(degree) = cos^{-1}(\frac{\lambda}{2\pi d}\Phi) \tag{5.6}$$

where Φ is the phase difference between the same received signals at two different sensors in radians, λ is the wavelength in meters at Tx frequency, and d is the separation between Rx sensors in meters. It is worth mentioning here that the AoA should be the same for two Tx stations transmitting from the same tower. It can be seen in the Equation (5.6) that the terms $(\frac{\lambda}{2\pi d}\Phi_{12})$ resulting from two co-located Tx signals must be equal to each other as shown in Equation (5.7).

$$cos^{-1}(\frac{\lambda_1}{2\pi d}\Phi_{12}) = cos^{-1}(\frac{\lambda_2}{2\pi d}\Phi'_{12}) \tag{5.7}$$

where Φ_{12} and Φ'_{12} are the phase differences between the same received signals at two different sensors from colocated Txs transmitting at different frequencies in radians. This algorithm was applied to find the optimum frequency bin from which to extract the phase information. Moreover, the frequency bin must satisfy the previous stipulations about the SNR (SNR $\geq$ 45 dB). It should be noted here that the algorithm was applied to supertowers where one tower hosted more than one transmitter. The effect of this algorithm on the accuracy of the position estimate will be discussed in this chapter.

5.3.2 Measurement results with supertower

The concept of supertower could not be verified in the previous measurement sites in Lawrence due to unavailability of multiple Tx signals with SNR values greater than 45 dB from a single tower. Therefore, a suitable location was first sought in the Google maps that can provide multiple Tx signals with SNR > 45 dB from the same tower. Besides, it was shown in Equation 4.27 that the maximum distance between the Tx and the Rx is 30 km for accurate position estimate. Moreover, the position of the transmitting towers were checked so that the co-located transmitters formed a triangle that is essential for accurate triangulation and thus position estimate. The geometrical position of the Rx and the towers with the Tx stations are showed in Figure 5.31.

The SNR was estimated by the Friis transmission equation as shown in Equation (2.2). The opti-

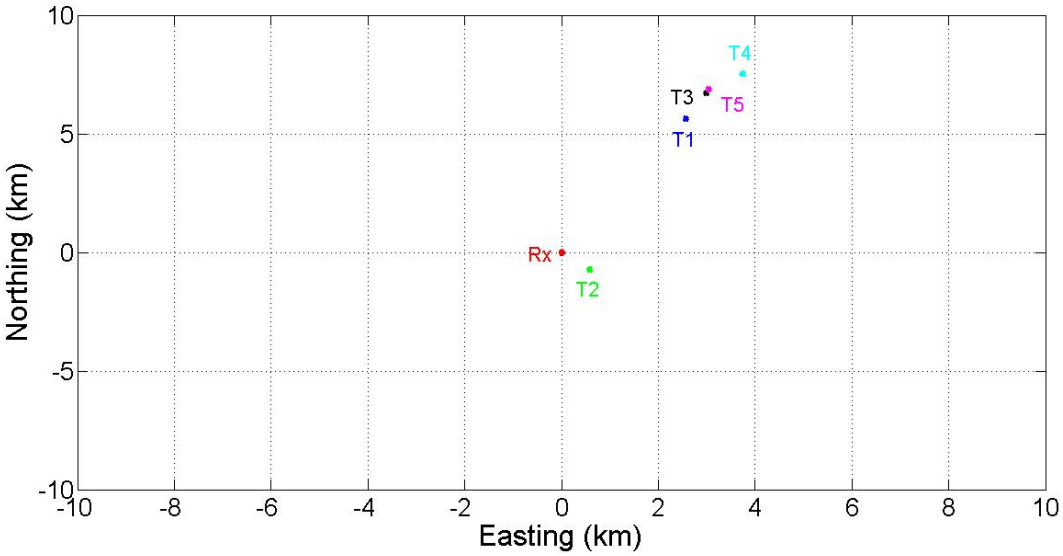

Figure 5.31: Geometrical position of the Towers and the Rx on the grid.

mum site was found to be the Blue Valley Park in Kansas City, MO. The SDR card with a laptop was used to capture the complex FM-band radio signals. The description of the SDR card and the configuration of SDR card with GRC flowgraph were described in the previous section. The received FM band signals are shown in Figure 5.32 and 5.33. The call signs, center frequencies, and measured SNRs of each station are shown in the box above the corresponding signals.

The noise floor of the SDR card was assumed to be -90 dBm as was assumed during the previous measurement. It can be seen in Figures 5.32 and 5.33 that the spectrum provided multiple Tx signals with SNR > 45 dB. The actual position of the Tx stations were collected from [104]. The co-located Tx stations with SNR > 45 dB and within the range of 30 km are shown in a tabular format in Table 5.3.

The availability of multiple Tx stations provided the opportunity to obtain finer AoA accuracy by applying the method described in the previous section. The application of the algorithm will be shown in the next section for supertowers, such as 2, 3, and 4.

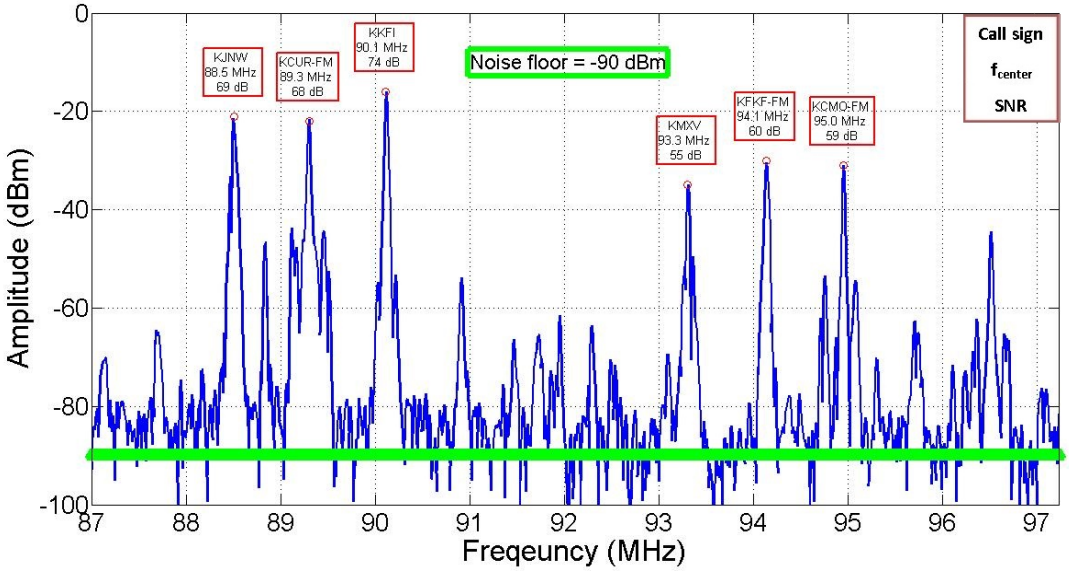

Figure 5.32: Spectrum of the lower FM band received signals.

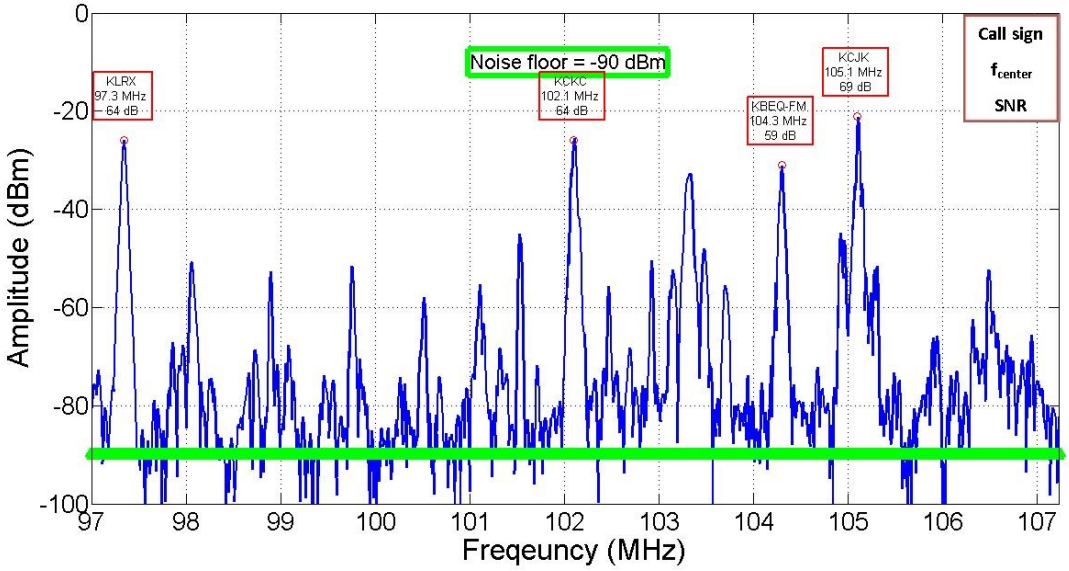

Figure 5.33: Spectrum of the upper FM band received signals.

5.3.2.1 AoA calculation from tower 2

The accuracy of AoA calculation depends on the accurate phase difference measurement. It was shown in the previous chapter that finer AoA accuracy can be achieved by averaging phase dif-

Table 5.3: The co-located Tx transmitters with SNR > 45 dB and R < 30 km.

Tower number	Tx frequency (MHz)			
1	88.5	-	-	-
2	93.3	103.3	94.1	-
3	89.3	104.3	-	-
4	94.9	102.1	105.1	97.3
5	90.1	-	-	-

ference than averaging AoAs. Moreover, the phase difference measurement accuracy gets finer by discarding measured results outside σ. Therefore, the phase difference between the received signals were measured for 1000 snapshots and then the results outside σ were discarded. Afterwards, the average of the remaining snapshots were recorded as the phase difference at that particular frequency. The phase differences for all of the Tx frequencies at tower 2 are shown in Figure 5.34.

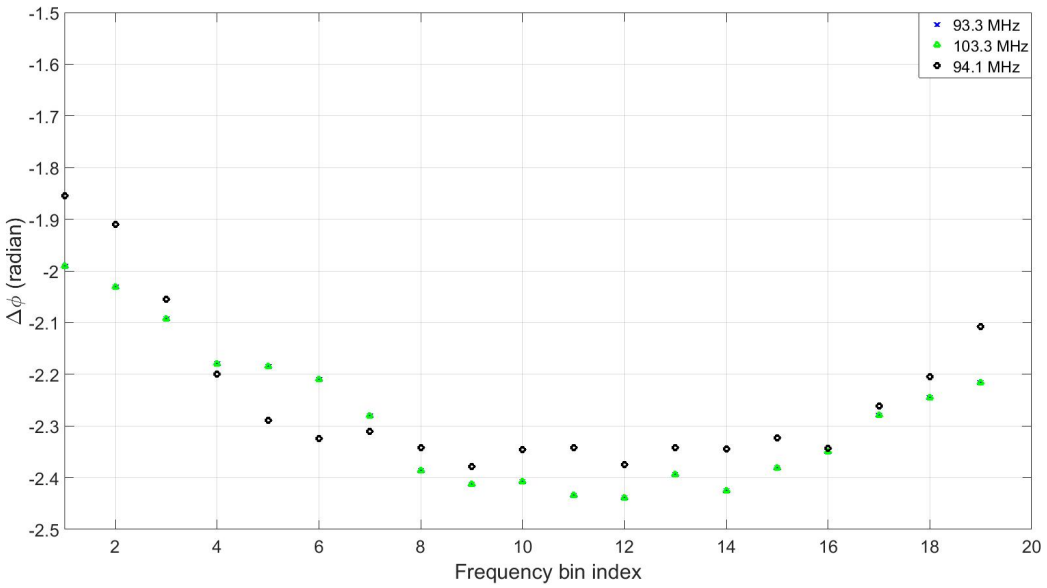

Figure 5.34: Phase difference between received signals from tower 2.

It was previously explained that the product of phase difference and $(\frac{\lambda}{2\pi d})$ should be equal for all the Tx stations located at the same tower. The product of phase differences and the constant terms for all Tx stations on tower 2 are shown in Figure 5.35.

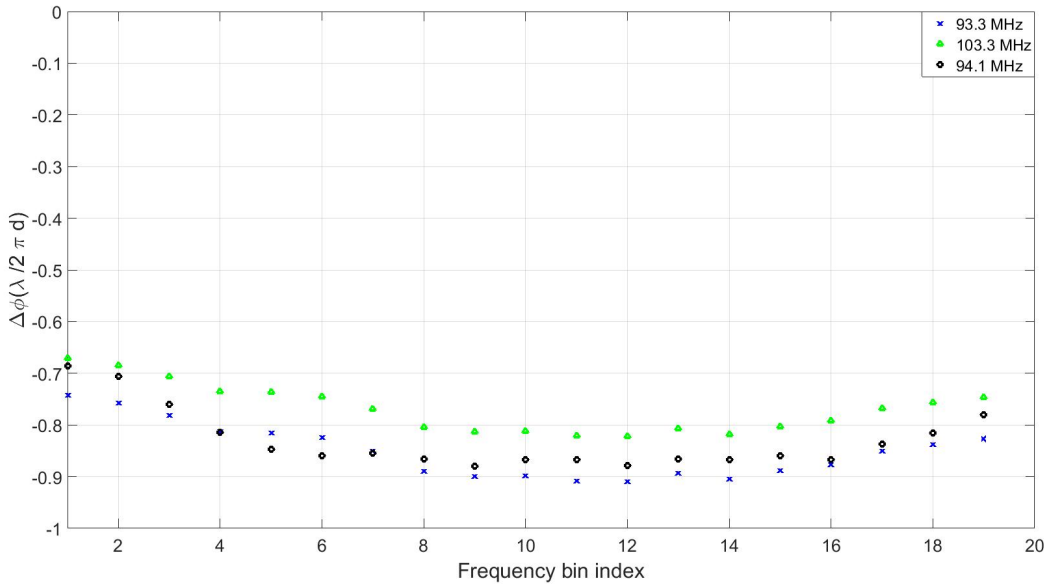

Figure 5.35: Product of phase difference and $\frac{\lambda}{2\pi d}$ term for all Tx signals from tower 2.

The selection of the appropriate frequency bin depends on the SNR and the product term as shown in Figure 5.35. The difference in the products of two colocated Tx frequencies should be zero. Besides, it has been mentioned in Equation (4.26) that the proposed method requires 45 dB or higher SNR.

The SNR for all the frequency bins of the Tx stations at tower 2 is shown in Figure 5.36.

First, the frequency bins that provided SNR < 45 dB were excluded from the selection of optimum bins. Then the remaining bins of one Tx frequency was compared to the other remaining bins of the second Tx frequency as shown in Figure 5.35. The bins of the Tx frequencies that were equal or close to each other with 45 dB or higher SNR were chosen to be the optimum bin for that corresponding Tx frequency. The optimum bins for the tower 2 Tx stations of 93.3 MHz, 103.3 MHz, and 94.1 MHz were chosen to be the bins with center frequencies of 93.31 MHz, 103.32 MHz, and 94.15 MHz. The calculated AoAs from the selected frequency bins are shown in Table 5.4.

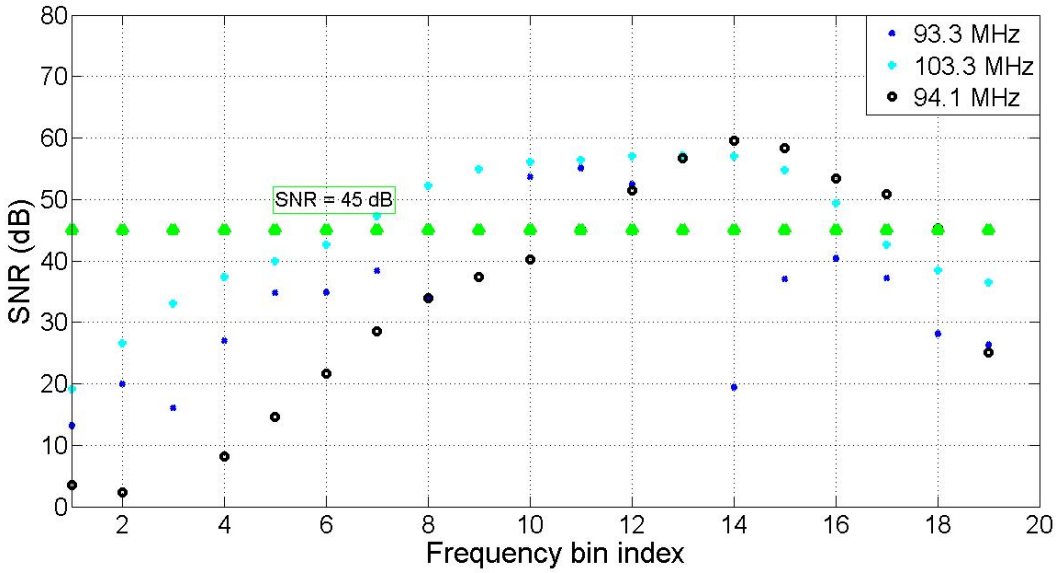

Figure 5.36: SNR at each frequency bins of the Tx stations at tower 2.

Table 5.4: Calculated AoAs from the optimum frequency bins for tower 2.

Tx frequency (MHz)	Calculated AoA (^{o})	Optimum frequency bin	Highest SNR Frequency bin
93.3	-28.1378	11	11
103.3	-28.4238	12	12
94.1	-28.4834	15	14

It should be noted here that the optimum bin selected by the application of proposed algorithm was not the same as the frequency bin with maximum SNR. Thus the supertower provides an option to obtain finer accuracy in the AoA calculation. Finally, the AoAs of the Tx stations were averaged to obtain the AoA from that tower as shown in Equation 5.8.

$$AoA_n = \sum_{i=1}^{N} \frac{AoA_i}{N} \tag{5.8}$$

where AoA_n is the AoA from the Tx stations at tower n, AoA_i is the AoA from i^{th} Tx located at tower n, and N is the total number of Tx stations at tower n.

5.3.2.2 AoA calculation from tower 3

The phase differences for all of the Tx frequencies at tower 3 are shown in Figure 5.37.

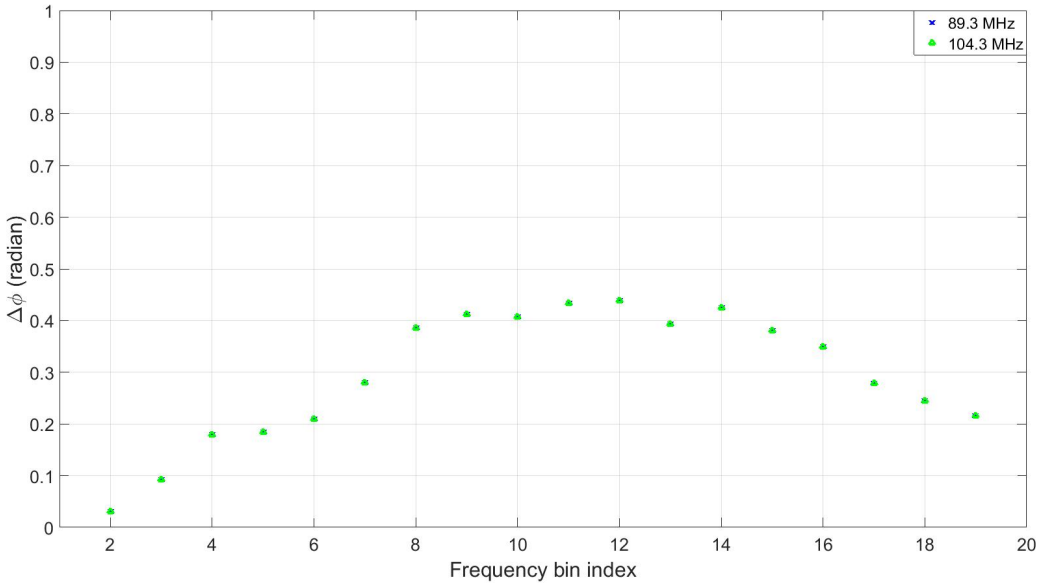

Figure 5.37: Phase difference between received signals from tower 3.

The product of phase differences and the constant terms for all Tx stations on tower 3 are shown in Figure 5.38.

The SNR for all the frequency bins of the Tx stations at tower 3 is shown in Figure 5.39.

The calculated AoAs from the selected frequency bins are shown in Table 5.5.

Table 5.5: Calculated AoAs from the optimum frequency bins for tower 3.

Tx frequency (MHz)	Calculated AoA (^{o})	Optimum frequency bin	Highest SNR Frequency bin
89.3	88.3713	10	11
104.3	88.4106	10	12

Finally, the AoAs of the Tx stations are averaged to obtain the AoA from that tower as shown in

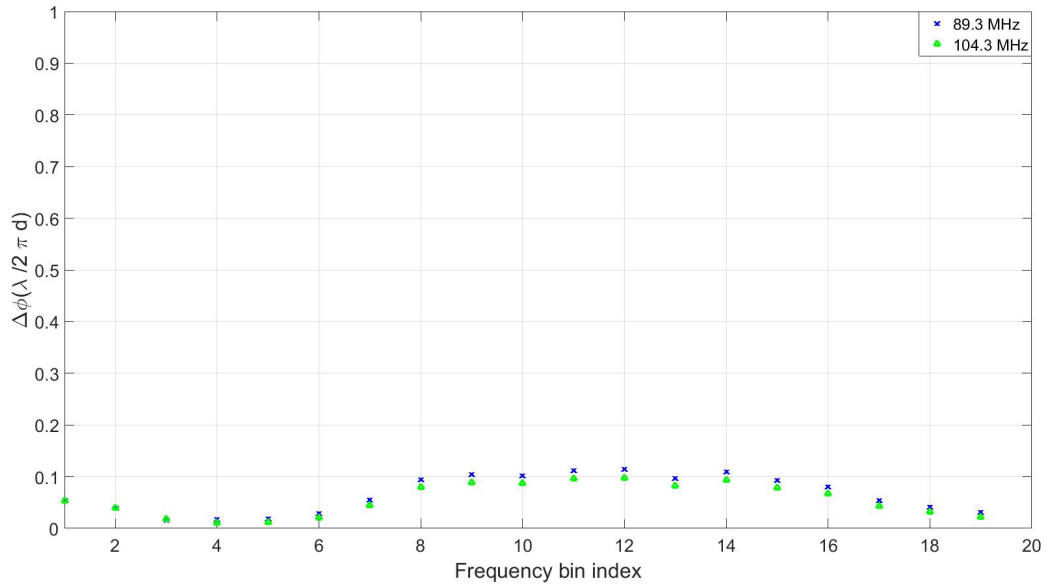

Figure 5.38: Product of phase difference and $\frac{\lambda}{2\pi d}$ term for all Tx signals from tower 3.

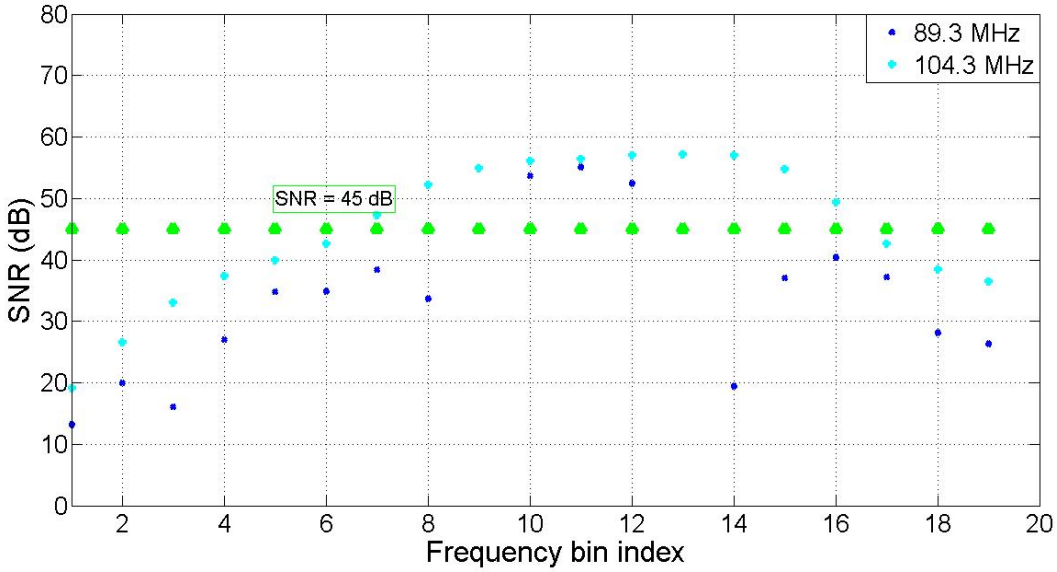

Figure 5.39: SNR at each frequency bins of the Tx stations at tower 3.

Table 5.5.

5.3.2.3 AoA calculation from tower 4

The phase differences for all of the Tx frequencies at tower 4 are shown in Figure 5.40.

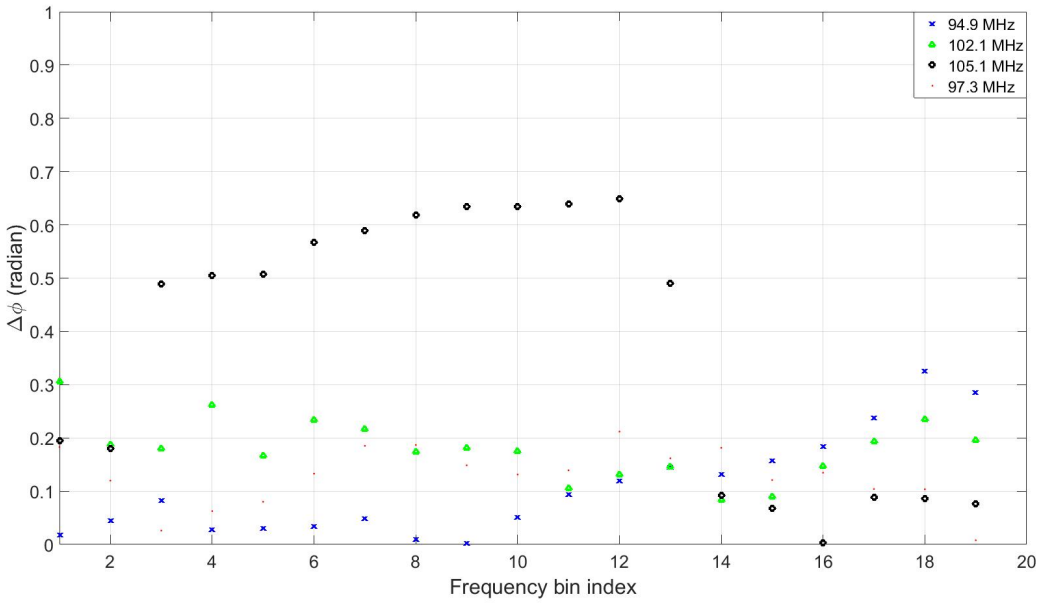

Figure 5.40: Phase difference between received signals from tower 4.

The product of phase differences and the constant terms for all Tx stations on tower 4 are shown in Figure 5.41.

The SNR for all the frequency bins of the Tx stations at tower 4 is shown in Figure 5.42.

The calculated AoAs from the selected frequency bins are shown in Table 5.6.

Finally, the AoAs of the Tx stations are averaged to obtain the AoA from that tower as shown in Table 5.6.

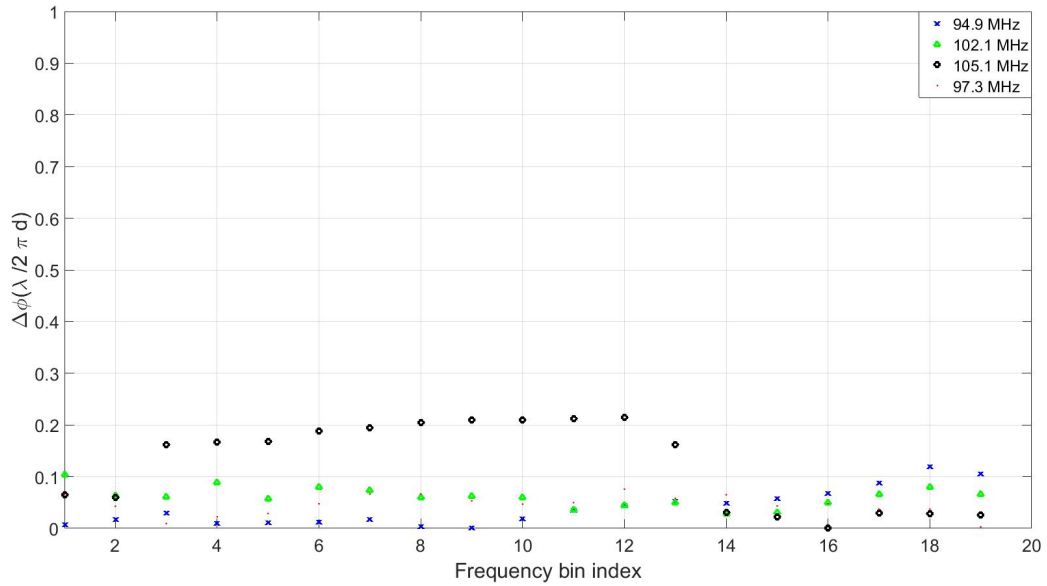

Figure 5.41: Product of phase difference and $\frac{\lambda}{2\pi d}$ term for all Tx signals from tower 4.

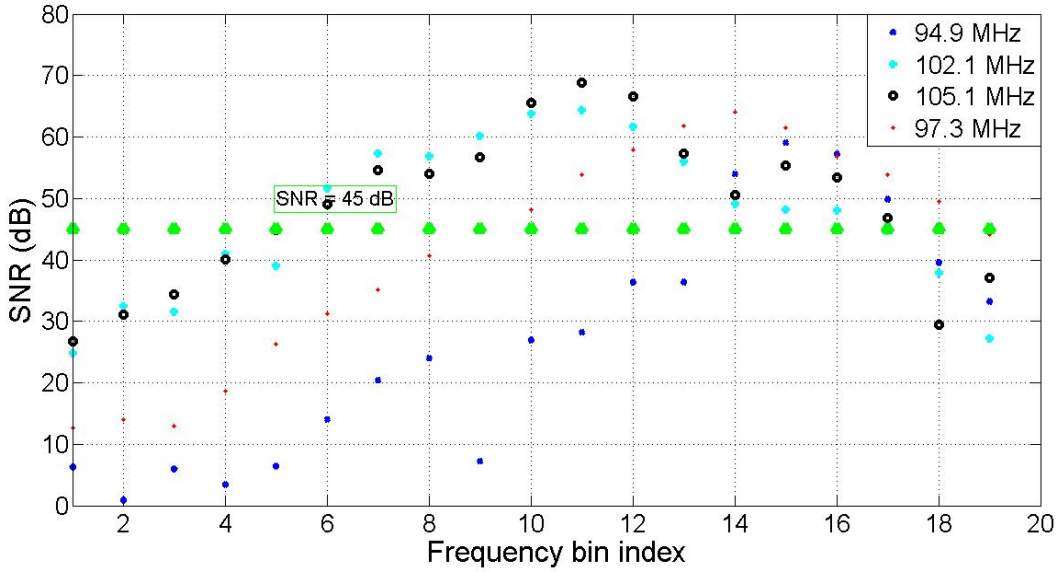

Figure 5.42: SNR at each frequency bins of the Tx stations at tower 4.

5.3.2.4 Comparison of position estimates with and without supertowers

The position estimate accuracy is a function of AoA accuracy as shown in the Chapter 3. Moreover, the dissertation proposed an algorithm for achieving finer AoA measurement accuracy by utilizing

Table 5.6: Calculated AoAs from the optimum frequency bins for tower 4.

Tx frequency (MHz)	Calculated AoA (^{o})	Optimum frequency bin	Highest SNR Frequency bin
94.9	87.2439	14	15
102.1	87.1506	13	11
105.1	86.6302	11	11
97.3	87.4297	12	14

supertowers. Therefore, the position estimate was calculated using supertowers and then the error in position estimate was calculated. The resulted position estimation results are shown in Table 5.7.

Table 5.7: A comparison of position estimate with and without supertower.

No. of utilized supertowers	Index of used supertowers	Position estimate error (m)
3	2, 3, and 4	12.57
2	1, 2, and 3	32.55
2	1, 2, and 4	22.43
2	1, 3, and 4	46.37
2	2, 3, and 5	33.43
2	2, 4, and 5	30.37
2	3, 4, and 5	48.28
1	1, 2, and 5	26.35
1	1, 2, and 5	26.35
1	1, 3, and 5	63.31
1	1, 4, and 5	30.48

It can be seen from the above results that the accuracy of the position estimate was the finest with the utilization of all of the 3 supertowers. Therefore, it can be concluded that a fine accuracy in the position estimate can be achieved by utilizing triangulation along with the application proposed in this dissertation for selection of the Tx and the supertowers.

5.4 Further investigation of error sources

It has been shown in the previous section that the SDR card that was used in the measurement procedures exhibited an elevated noise floor of -90 dBm compared to the calculated thermal noise floor. Therefore, the adjacent frequency bands were scanned by the SDR card at the watch tower in the Overlook Park to find the presence of any strong signal that might result in aliasing into the desired frequency range. The measured signals for the adjacent frequency bands are shown in Figure 5.43, 5.44, and 5.45.

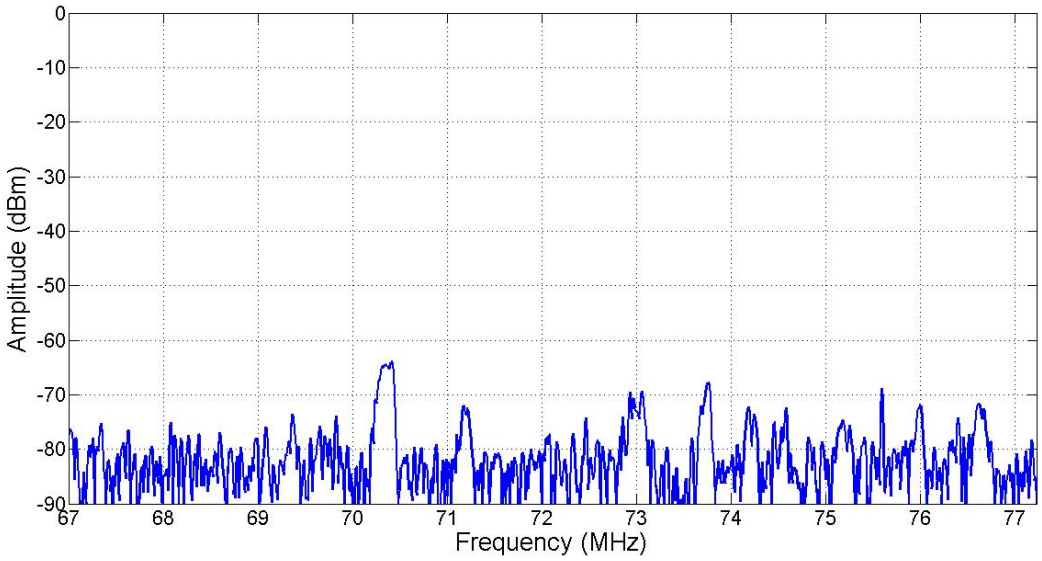

Figure 5.43: Frequency spectrum from 67 MHz to 77 MHz.

It was assumed in the previous sections that the signals with SNR > 45 dB were not the results of aliased signals. The absence of any strong signal with SNR > 45 dB in the above spectrums holds the previous assumption. Moreover, the effect of multipath was examined by scanning the frequency spectrum from top of the watch tower and at the bottom of the watch tower. The spectra at the top and bottom of the watch tower are shown in Figures 5.46 and 5.47.

It is evident from the above figures that the spectrums at the top and bottom of the watch tower

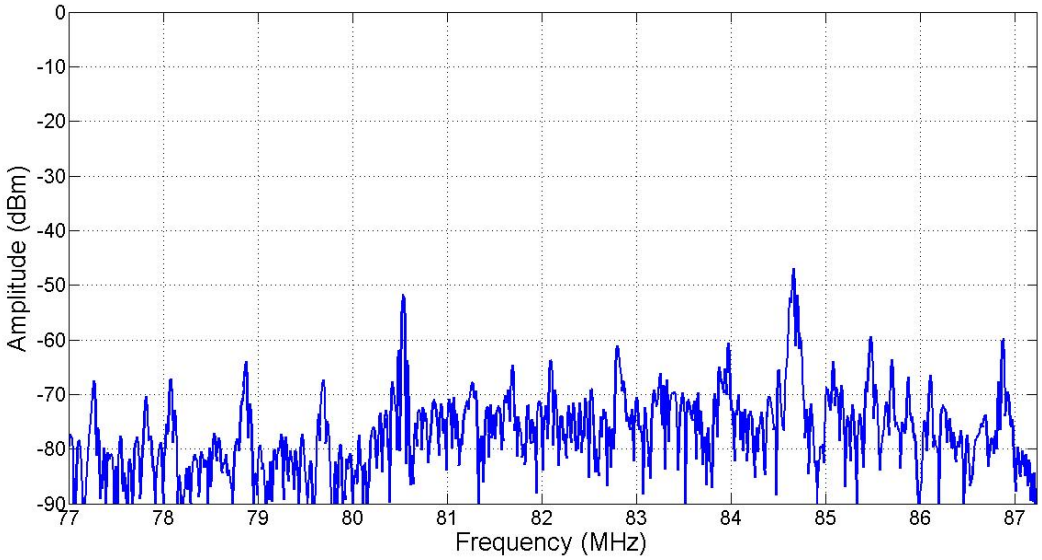

Figure 5.44: Frequency spectrum from 77 MHz to 87 MHz.

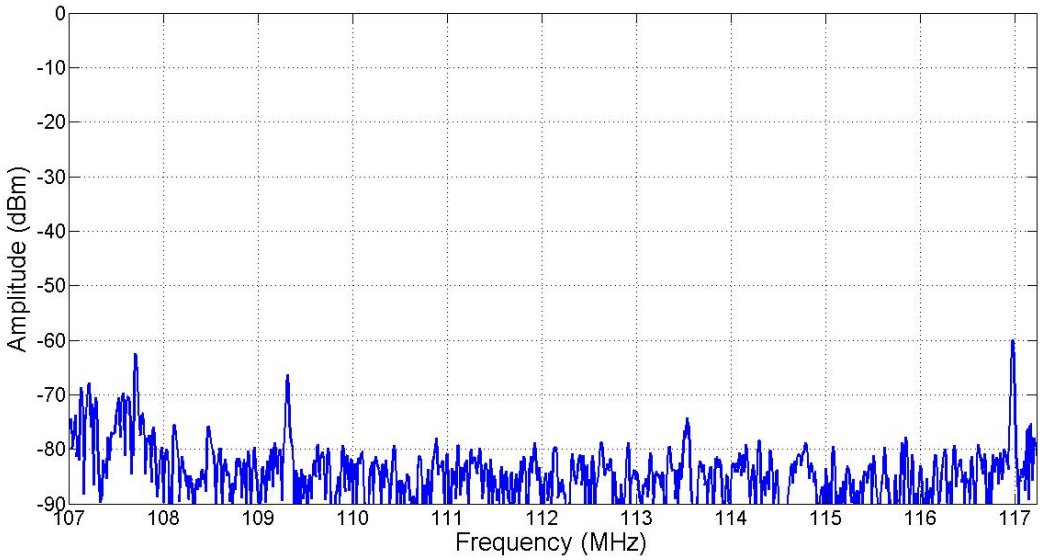

Figure 5.45: Frequency spectrum from 107 MHz to 117 MHz.

(30 feet tall) exhibited slightly different phase information. Therefore, the position estimate error was partly due to the multipath phenomena. However, the method for the elimination of multipath effect from the AoA calculation was out of scope of this dissertation.

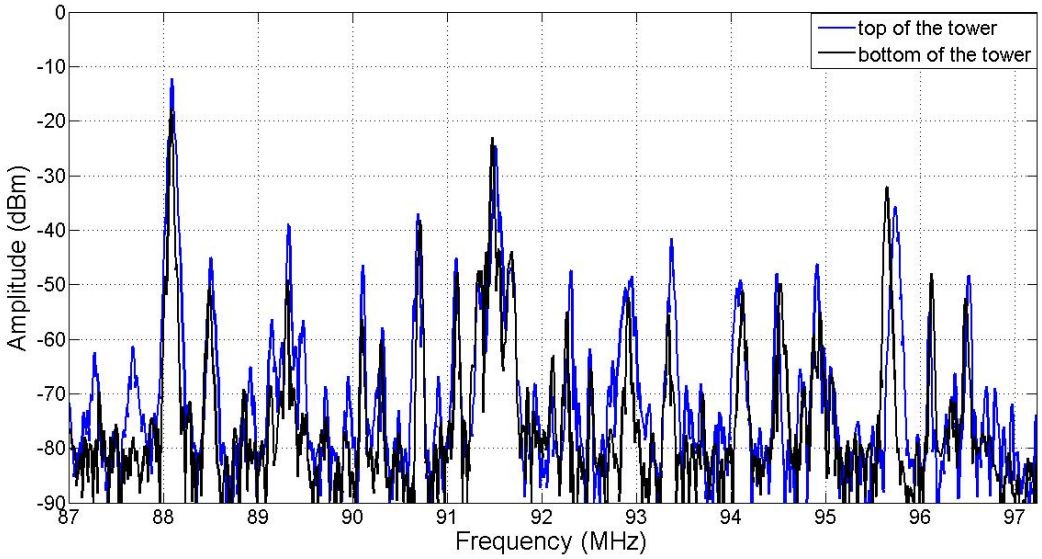

Figure 5.46: Comparison of frequency spectrums (87-97 MHz) at the top and bottom of watch tower.

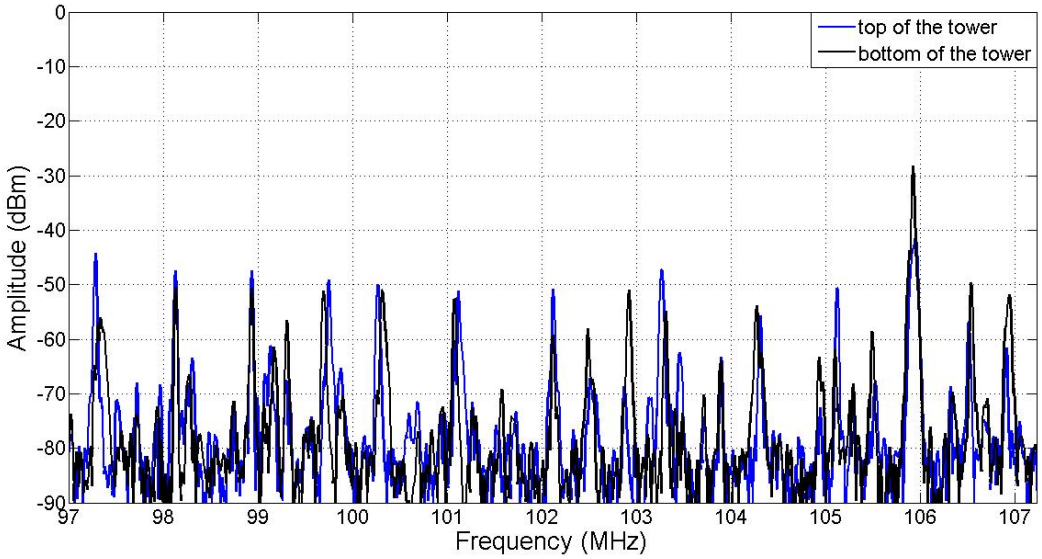

Figure 5.47: Comparison of frequency spectrums (97-107 MHz) at the top and bottom of watch tower.

Chapter 6

Closure

6.1 Conclusions

This dissertation proposed an alternative and backup navigation system for UAVs in the case of a GPS outage. The navigation system exploits SOP to estimate the position of the receiver. The proposed method utilizes FM band radio transmitters as SOP and employs triangulation for measuring AoAs and localization. The objective of the proposed technique is to provide position estimates comparable to GPS in accuracy and update rate. Simulations have been performed to analyze the effect of different parameters, such as N_s, SNR, baseline separation (d), and true AoAs on the accuracy of AoA estimation. Moreover, a closed form equation has been derived to predict the standard deviation of AoA based on the aforementioned parameters. The proposed method introduces dAoAs instead of AoAs for triangulation and thus enables the solution to be independent of the receiving antenna orientation. The simulation provides a position estimation with an error of less than 10 m. Furthermore, the maximum range between the Tx and the Rx has been calculated. Besides, the minimum required SNR for the proposed technique has been derived from Friis Transmission equation. Moreover, the error in position estimate by the proposed method has been mapped on a 50 km times 50 km grid to find the effect of geometrical combination formed by the Tx stations and the Rx. Besides, the theory, working principle, and simulation results of the

proposed technique has been presented and discussed extensively.

The proposed method has been verified by measurements conducted in multiple sites. The first measurement was conducted on top of the roof of Eaton Hall located at the University of Kansas, Lawrence, KS, USA. The received signals were recorded as a time series data with a digital storage oscilloscope and then post-processed in a remote station using signal processing software, such as MATLAB. However, accurate measurement results could not be obtained due to the presence of pre-existing scatterers at the same site. The second measurement was conducted on top of the watch tower at Wells Overlook County Park at Lawrence, KS. The measurement was conducted for 1000 snapshots using an SDR card. The description, configuration, and method of defining the SDR card with GNU radio companion flowgraph has been explained with step by step procedures. A comparison of accuracy between the measurement results obtained with averaging phase differences, AoAs, and position estimated has been presented. It was found that the averaging of phase differences between the received signals resulted in the most accurate position estimate of all. A localization with reduced uncertainty was obtained by filtering the phase difference measurement results that resided outside of σ. The measurement result obtained by averaging phase differences at the two receiving sensors provided a position estimate error of 16.4 m with an update rate of 10 Hz.

This dissertation proposes an algorithm to achieve finer position estimate accuracy by exploiting supertowers. supertower is a tower that hosts more than one SOP transmitters. The concept of supertower could not be verified at the watch tower in Overlook Park due to unavailability of Tx signals with required SNR. Therefore, the Blue Valley Park was selected as the potential site for verifying supertower concept. A detailed descrption of obtaining finer position estimate accuracy utilizing supertowers has been presented along with measurement results. It was shown that the utilization of all the supertowers provided the least error of 12 m in localization.

6.2 Future Work

The accuracy of the measurement suffered from low SNR and multipath. The low SNR was due to the ambient noise that elevated the noise floor by 41 dB. Multipath was another parameter that corrupted the measurement.

The direct path between the Tx and the Rx can be separated from multipath signal in the time domain. The signal from an FM transmitter can be spectrally isolated and then the signals from the two Rx antennas can be cross-correlated. The peak of this cross-correlation will represent the direct path and will possess the smallest lag time. On the contrary, the multipath signals will contain reduced correlation coefficients and will exhibit greater lag times. Therefore, multipath signal needs to be cancelled or suppressed in the time domain and then the signal processing can be applied to find the AoA of the transmitter. However, the study of eliminating multipath effect from the measured results was out of scope of this dissertation.

Bibliography

[1] X. Liu, P. Chen, X. Tong, S. Liu, Z. Hong, L. Li, and K. Luan, "UAV based low-altitude aerial photogrammetric application in mine areas measurement," *Second International Workshop on Earth Observation and Remote Sensing Applications (EORSA)*, June, 2012, pp. 240-242.

[2] J. T. K. Ping, A. E. Ling, T. J. Quan, and C. Y. Dat, "Generic Unmanned Aerial Vehicle (UAV) for civilian application - a feasibility assessment and market survey on civilian application for aerial imaging," *IEEE Conference on Sustainable Utilization and Development in Engineering and Technology (STUDENT)*, Oct, 2012, pp. 289-294.

[3] A. M. Samad, N. Kamarulzaman, M. A. Hamdani, T. A. Mastor, and K. A. Hashim, "The potential of Unmanned Aerial Vehicle (UAV) for civilian and mapping application," *IEEE 3rd International Conference on System Engineering and Technology (ICSET)*, Aug. 2013, pp. 313-318.

[4] J. Everaerts, "The use of Unmanned Aerial Vehicles (UAVs) for remote sensing and mapping," *The International Archives of the Photogrammetry, Remote Sensing and Spatial Information Sciences*, vol. XXXVII, part B1, pp. 1187-1192, 2008.

[5] A. Rango, A. Laliberte, J. E. Herrick, C. Winters, K. Havstad, C. Steele, and D. Browning, "Unmanned Aerial Vehicle (UAV) based remote sensing for rangeland assessment, monitoring, and management," *Journal of Applied Remote Sensing*, vol. 3, 033542, pp. 1-15, 2009.

[6] P. Malone, H. Apgar, S. Stukes, and S. Sterk, "Unmanned Aerial Vehicles unique cost estimating requirements," *IEEE Aerospace Conference*, March, 2009, pp. 1-8.

[7] N. Mohamed and J. A. Jaroodi, "Service-oriented middleware for collaborative UAVs," *IEEE 14th International Conference on Information Reuse and Integration (IRI)*, Aug. 2013, pp. 185-192.

[8] "Exclusive: Iran hijacked US drone, says Iranian engineer (Video)", The Christian Science Monitor (www.csmonitor.com), December 15, 2011.

[9] "UAV Crash in Korea Linked To GPS Jamming", http://www.ainonline.com, June 1, 2012.

[10] M. A. Enright and C. N. Kurby, "A signals of opportunity based cooperative navigation network," *IEEE National Aerospace and Electronics Conference (NAECON)*, July, 2009, pp. 213-218.

[11] D. B. Mcmillon, "An analysis of position probability distribution of trilateration and triangulation for extremely deep space navigation," *Research Experience for Undergraduates (REU)*, Dept. of Mathematics, University of Michigan, July 13, 2011.

[12] W. J. Ecker, *Loran-C User Handbook*, Commandant publication P16562.5, ch. 1.

[13] J. A. V. Allen, "Basic principles of celestial navigation," *American Journal of Physics*, vol. 72, no. 11, pp. 1418-1424, 2004.

[14] G. Kaplan, "Determining the position and motion of a vessel from celestial observations," *Navigation*, vol. 42, no. 4, pp. 631-648, 1995.

[15] Y. T. Chan and K. C. Ho, "A simple and efficient estimator for hyperbolic location," *IEEE Transactions on Signal Processing*, vol. 42, no. 8, pp. 1905-1915, 1994.

[16] M. Zillick, D. Legenstein, M. Ayromlou, and M. Vincze, "Robust object tracking for robot manipulation and navigation," *International Archives of Photogrammetry and Remote Sensing*, vol. XXXIII, part. B5, pp. 951-958, 2000.

[17] K. A. Fisher, "The Navigation Potential of Signals of Opportunity-Based Time Difference on Arrival Measurements", Ph.D. thesis, Dept. of Electrical Engineering, Air Force Institute of Technology, 2005.

[18] J. Cornwall et. al., *Non-GPS Methods of Geolocations*, The MITRE Corporation, Report to the Defense Advanced Research Projects Agency (DARPA), McLean, VA, January, 2002.

[19] A. D. King, "Inertial navigation - past, present, and future," *IEE Colloquium on Airborne Navigation Systems Workshop* (Digest No. 1997/169), 1997, pp. 3/1-3/9.

[20] C. C. Foster and G. H. Elkaim, "Extension of a two-step calibration methodology to include non-orthogonal sensor axes," *IEEE Transactions on Aerospace and Electronic Systems*, vol. 44, no. 3, pp. 1070-1078, 2008.

[21] M. Barczyk, M. Jost, D. R. Kastelan, A. F. Lynch, and K. D. Listmann, "An experimental validation of magnetometer integration into a GPS aided helicopter UAV navigation system," *American Control Conference*, 2010, pp. 4439-4444.

[22] S. D. L. Parra and J. Angel, "Low cost navigation system for UAVs," *Aerospace Science and Technology*, vol. 9, no. 6, pp. 504-516, 2005.

[23] C.-S. Yoo and L.-K. Ahn, "Low cost GPS/INS sensor fusion system for UAV navigation," *The 22nd Digital Avionics Systems Conference*, 2003, vol. 2, pp. 8.A.1-8.1.-9.

[24] A. Ramanandan, "High accuracy sensor aided Inertial Navigation System," PhD dissertation, Dept. of Electrical Engineering, 2011.

[25] J. S. Jang and D. Liccardo, "Small UAV automation using MEMS," *IEEE Aerospace and Electronic Systems Magazine*, vol. 22, issue 5, pp. 30-34, 2007.

[26] L. Zouaghi, A. Alexopolous, M. Koslowski, A. Kandil, and E. Badreddin, "An integrated distributed monitoring for mission-based systems : On the example of an autonomous un-

manned helicopter," *6th IEEE International Conference on Intelligent Systems*, Sept. 2012, pp. 415-420.

[27] V. I. Kortunov, I. Yu. Dybska, G. A. Proskura, and A. S. Kravchuk, "Integrated mini INS based on MEMS sensors for UAV control," *IEEE Aerospace and Electronic Systems Magazine*, vol. 24, no. 1, pp. 41-43, 2009.

[28] A. G. Quinchia and C. Ferrer, "A low-cost GPS and INS integrated system based on a FPGA platform," *2011 International Conference on Localization and GNSS*, 2011, pp. 152-157.

[29] V. Kharchenko, V. Kondratyuk, S. Llnytska, O. Kutsenko, and V. Larin, "Urgent problems of UAV navigation system development and practical implementation," *2013 IEEE International Conference on Actual Problems of Unmanned Air Vehicles Developments*, 2013, pp. 157-160.

[30] E. D. Kaplan and J. H. Christopher, *Understanding GPS*, second ed., Artech house, London, Boston, 2006, ch. 1-4.

[31] A. Angrisano, "GNSS/INS Integration Methods", Ph. D. Dissertation, Dept. of Electrical Engineering, University of Calgary, 2010.

[32] S. Pace, G. P. Frost, I. Lachow, D. R. Frelinger, D. Fossum, D. Wassem, M. M. Pinto,"The global positioning system assessing national policies," *GPS History, Chronology, and Budgets*, Appendix A and Appendix B, 1995.

[33] G. Ambrosino, M. Ariola, U. Ciniglio, F. Corraro, E. D.-Lellis, and A. Pironti, "Path generation and tracking in 3-D for UAVs," *IEEE Transactions on Control Systems Technology*, vol. 17, no. 4, pp. 980-988, 2009.

[34] D. Y. Hsu, "Relations between dilutions of precision and volume of the tetrahedron formed by four satellites," *IEEE Position Location and Navigation Symposium*, 1994, pp. 669-676.

[35] J. Sunghun and K. B. Ariyur, "Robustness for large scale UAV autonomous operation," *2011 IEEE International Systems Conference*, 2011, pp. 309-314.

[36] J. M.-Hilberg and T. Jacob, "High accuracy navigation and landing system using GPS/IMU system integration," *IEEE Aerospace and Electronic Systems Magazine*, vol. 9, no. 7, pp. 11-17, 1994.

[37] R. E. Kalman, "A new approach to linear filtering and prediction problems," *Transactions of the ASME-Journal of Basic Engineering*, 82 (series D), pp. 35-45, 1960.

[38] H. Long, Z. Qu, X. Fan, and S. Liu, "Distributed extended Kalman filter based on Consensus filter for wireless sensor network," *10th World Congress on Intelligent Control and Automation*, July, 2012, pp. 4315-4319.

[39] L. Chunbo, S. I. Mcclean, G. Parr, L. Teacy, and R. D.-Nardi, "UAV position estimation and collision avoidance using the extended Kalman filter," *IEEE Transactions on Vehicular Technology*, vol. 62, no. 6, pp. 2749-2762, 2013.

[40] E. Petritoli, T. Giagnacova, F. Leccese, "Lightweight GNSS/IRS integrated navigation system for UAV vehicles," *2014 IEEE Metrology for Aerospace (MetroAeroSpace)*, 29-30 May, 2014, pp. 56-61.

[41] C. Lukianto and H. Sternberg, "Overview and evaluation of current indoor navigation techniques and implementation studies," *FIG Working Week 2011*, May 2011, pp. 1-14.

[42] Z. Tao and W. Lei, "SINS and GPS integrated navigation system of a small unmanned aerial vehicle," *FBIE '08 International Seminar on Future BioMedical Information Engineering*, 18th December, 2008, pp. 465-468.

[43] Y. Jiong, Z. Lei, D. Jiangping, S. Rong et. al.,"GPS/SINS/BARO integrated navigation system for UAV," *2010 International Forum on Information Technology and Applications (IFITA)*, 16-18 July, 2010, pp. 19-25.

[44] B. B. Mohr and D. L. Fitzpatrick, "Micro air vehicle navigation system," *IEEE Aerospace and Electronic Systems Magazine*, vol. 23, no. 4, pp. 19-24, 2008.

[45] X. Lei, J. Liang, S. Wang, and T. Wang, "An integrated navigation system for A small UAV using low-cost sensors," *International Conference on Information and Automation, 2008 (ICIA 2008)*, 20-23 June, 2008, pp. 765-769.

[46] H. Du, J. Cheng, and B. Wang, "Design of adaptive Kalman filter algorithm in integrated navigation system for land vehicles," *2013 IEEE International Conference on Mechatronics and Automation (ICMA)*, 4-7 Aug, 2013, pp. 1492-1496.

[47] Q. Yaohong and T. Qichuan, "Multi UAV cooperative positioning based on delaunay triangulation," *2010 International Conference on Computational Aspects of Social Networks*, 2010, pp. 401-404.

[48] R. Thamma, "Estimating position and orientation of an UAV with ultra sound and RF sensing," *Technology Interface Journal/Winter Special Issue*, vol. 10, no. 2, 2009.

[49] J. H. Clements, "Recursive maximum likelyhood estimation of aircraft position using multiple range and bearing measurements," *1996 IEEE Position Location and Navigation Symposium*, 1996, pp. 199-204.

[50] R. B. Flint and E. R. Hollm, "VOR evolutionary system improvements in the United States," *IEEE Transactions on Aerospace and Navigational Electronics*, vol. 12, no. 1, pp. 46-56, 1965.

[51] R. H. Mcfarland, "VOR error tolerance, stability, and accuracy," *IEEE Transactions on Aerospace and Electronic Systems*, vol. AES-3, no. 3, p. 578, 1967.

[52] A. S. Palatnick, "'Wide aperture digital VOR," *IEEE Transactions on Aerospace and Electronic Systems*, vol. AES-14, no. 6, pp. 853-865, 1978.

[53] J. R. Fountain, "Digital terrain system," *IEE Colloquium on Airborne Navigation Systems Workshop* (Digest 1997/169), 1997, pp. 4/1-4/6.

[54] J. P. Golden, "Terrain contour matching (TERCOM) : A cruise missile guidance aid," *SPIE Image Processing for Missile Guidance*, vol. 38, 1980, pp. 10-18.

[55] J. J. Rodriguez and J. K. Aggarwal, "Matching aerial images to 3-D terrain maps," *IEEE Transactions on Pattern Analysis and Machine Intelligence*, vol. 12, no. 12, pp. 1138-1149, 1990.

[56] J. Zhang, Y. Wu, W. Liu, and X. Chen, "Novel approach to position and orientation estimation in vision-based navigation," *IEEE Transactions on Aerospace and Electronic Systems*, vol. 46, no. 2, April, 2010.

[57] A. R. Jimenez, F. Zampella, and F. Seco, "Light-matching : A new signal of opportunity for pedestrian indoor navigation," *2013 International Conference on Indoor Positioning and Indoor Navigation*, 2013, pp. 1-10.

[58] M. K. Mohamed, S. Patra, and A. Lanzon, "Designing simple indoor navigation system for UAVs," *2011 19th Mediterranean Conference on Control and Automation*, 20-23 June, 2011, pp. 1223-1228.

[59] F. Weng, J. Cui, S. K. Phang, B. M. Chen, and T. H. Lee, "A mono camera and scanning laser range finder based UAV indoor navigation system," *2013 International Conference on Unmanned Aircraft Systems*, 2013, pp. 694-701.

[60] T. Krajnik, M. Nitsche, S. Pedre, L. Preucil et. al., "A simple visual navigation system for an UAV," *2012 9th International Multi-Conference on Systems, Signals and Devices (SSD)*, 20-23 March, 2012, pp. 1-6.

[61] J. Kim and S. Sukkarieh, "Autonomous airborne navigation in unknown terrain environments," *IEEE Transactions on Aerospace and Electronic Systems*, vol. 40, pp. 1031-1045, 2004.

[62] Z. Chen and J. Samarabandu, "Using multi-view geometry within extended Kalman filter framework for simultaneous localization and map-building," *IEEE International Conference on Mechanics and Automation*, 2005, pp. 695-670.

[63] H. D.-Whyte and T. Bailey, "Simultaneous Localization and Mapping : Part I," *IEEE Robotics Magazine*, 2006, pp. 99-108.

[64] J. Zhang, W. Liu, and Y. Wu, "Novel technique for vision-based UAV navigation," *IEEE Transactions on Aerospace and Electronic Systems*, vol. 47, no. 4, pp. 2731-2741, 2011.

[65] Y. Kim, D. Lee, H. Bang, "Vision-only UAV navigation aided by terrain elevation map," *2012 12th International Conference on Control, Automation and Systems (ICCAS)*, 17-21 Oct, 2012, pp. 1729-1733.

[66] L. Jian and L. X.-Min, "Vision-based navigation and obstacle detection for UAV," *2011 International Conference on Electronics, Communications and Control (ICECC)*, 2011, 9-11 Sept, 2011, pp. 1771-1774.

[67] D.-Y. Gu., C.-F. Zhu, J. Guo, S.-X. Li, and H.-X. Chang, "Vision-aided UAV navigation using GIS data," *2010 IEEE International Conference on Vehicular Electronics and Safety (ICVES)*, 2010, pp. 78-82.

[68] G. Conte and P. Doherty, "An integrated UAV navigation system based on Aerial Image matching," *2008 IEEE Aerospace Conference*, 2008, pp. 1-10.

[69] Z. C. Hao, C. J. Bin, S. C. Lei, and X. J. Hua, "An UAV navigation aided with computer vision," *The 26th Chinese Control and Decision Conference*, 2014, pp. 5297-5301.

[70] Z. Zhang, B. Sun, K. Sun, and W. Tang, "A new image matching algorithm based on multi-scale segmentation applied for UAV navigation," *2010 2nd International Conference on Information Science and Engineering (ICISE)*, 4-6 Dec, 2010, pp. 3447-3450.

[71] W. Ding, J. Wang, and A. Almagbile, "Adaptive filter design for UAV navigation with GPS INS optic flow integration," *2010 International Conference on Electrical and Control Engineering (ICECE)*, 25-27 June, 2010, pp. 4623-4626.

[72] J. Q. Cui, X. Dong, P. Liu, B. M. Chen, and T. H. Lee, "Autonomous navigation of UAV in forest," *2014 International Conference on Unmanned Aircraft Systems (ICUAS)*, 2014, pp. 726-733.

[73] R. M. Faragher and R. K. Harle, "SmartSlam - an efficient smartphone indoor positioning system exploiting machine learning and opportunistic sensing," *26th International Technical Meeting of the Satellite Division of the Institute of Navigation, ION GNSS+*, 2013.

[74] R. Faragher, C. Sarno, and M. Newman, "Opportunistic radio SLAM indoor navigation using Smartphone sensors," *IEEE/ION Plans 2012*, April 24-26, 2012, pp. 120-128.

[75] C. G. Bartone, "A terrestrial positioning and timing system (TPTS)," *2012 IEEE/ION Position Location and Navigation Symposium*, 2012, pp. 1175-1182.

[76] G. Wang, H. Chen, Y. Li, and M. Jin, "On received-signal-strength based localization with unknown transmit power and path loss exponent," *IEEE Wireless Communication Letters*, vol. 1, no. 5, pp. 536-539, 2012.

[77] Q. Kong, X. Yang, and X. Xie, "A novel localization algorithm based on received signal strength ratio," *4th International Conference on Wireless Communications, Networking, and Mobile Computing, 2008 (WiCOM '08)*, Oct. 2008, pp. 1-6.

[78] G. Ding, J. Zhang, L. Zhang, and Z. Tan, "Overview of received signal strength based fingerprinting localization in indoor wireless LAN environments," *IEEE 5th Internation Sym-*

posium on Microwave, Antenna, Propagation, and EMC Technologies for Wireless Communications (MAPE), Oct. 2013, pp. 160-164.

[79] X. Luo, W. J. O'Brein, and C. L. Julien, "Comparative evaluation of Received Signal-Strength Index (RSSI) based indoor localization techniques for construction jobsites," *Advanced Engineering Informatics*, vol. 25, no. 2, pp. 355-363, 2011.

[80] L. A. Merry, R. M. Faragher, and S. Scheding, "Comparison of opportunistic signals for localisation," *7th IFAC Symposium on Intelligent Autonomous Vehicles*, 2010, pp. 109-114.

[81] H. I. Ahmed, I. Memon, Y. Du, and W. Xie, "Estimation of Time Difference of Arrival (TDOA) for the source radiates BPSK signal", *International Journal of Xomputer Science Issues (IJCSI)*, vol. 10, no. 2, pp. 164-171, 2013.

[82] A. Bensky, *Wireless Positioning Technologies and Applications*, Artech house, 2008, ch. 7.

[83] R. M. Faragher, "Radio navigation," U.S. Patent 8644850 B2, Oct. 4, 2010.

[84] R. M. Faragher, "Navigation systems," U.S. Patent 20120191340 A1, Oct. 4, 2010.

[85] B. W. Remondi, "Global positioning system carrier phase : description and use," *Journal of Geodesy*, vol. 59, no. 4, pp. 361-377, 1985.

[86] Y. Khmou, S. Safi, and M. Frikel, "Comparative study between several direction of arrival estimation methods," *Journals of Telecommunications and Information Technology*, vol. 1, pp. 41-48, 2014.

[87] A. Vesa and A. Iozsa, "Direction-of-arrival estimation for uniform sensor arrays," *9th International Symposium on Electronics and Telecommunications (ISETC)*, Nov. 2010, pp. 249-252.

[88] M. S. Vijay and U. L. Bombale, "An overview of smart antenna and a survey on direction of arrival estimation algorithms for smart antenna," *IOSR Journal of Electronics and Communications Engineering (IOSR-JECE)*, ISSN : 2278-2834, ISBN : 2278-8735, pp. 1-6.

[89] R. Muhamed, "Directional of arrival estimation using antenna arrays", MS Thesis, Dept. of Electrical Engineering, Virginia Polytechnic Institute and State University, 1996.

[90] L. C. Godara, "Limitations and capabilities of directions-of-arrival estimation techniques using an array of antennas : a mobile communications perspective," *IEEE International Symposium on Phased Array Systems and Technology*, Oct. 1996, pp. 327-333.

[91] R. O. Schmidt, "Multiple emitter location and signal parameter estimation," *IEEE Transactions on Antennas and Propagations*, vol. 34, no. 3, pp. 276-280, 1986.

[92] R. Roy and T. Kailath, "ESPIRIT-Estimation of signal parameters via rotational invariance techniques," *IEEE Transactions on Acoustics, Speech and Signal Processing*, vol. 37, no. 7, pp. 984-995, 1989.

[93] A. Ess, K. Schindler, B. Leibe, and L. V. Gool, "Object detection and tracking for autonomous navigation in dynamic environments," *International Journal of Robotic Research*, vol. 29, no. 4, pp. 1707-1725, 2010.

[94] J. Wu and Z. Yang, "Spacecraft navigation based on X-ray pulsar observation simulator," *International Conference on Electronics and Optpelectronics*, 2011, vol. 2, pp. 391-394.

[95] S. K. Jordan and J. L. Center, "Establishing requirements for gravity surveys for very accurate inertial navigation," *Navigation*, vol. 33, pp. 90-108, 1986.

[96] H.-C. Chen, T.-H. Lin, H. T. Kung, C.-K. Lin, and Y. Gwon, "Determining RF angle of arrival using COTS antenna arrays : A field evaluation," *Military Communications Conference*, 2012, pp. 1-6.

[97] W. Read, "Review of conventional tactical radio direction finding systems," Defense Research Establishment, Ottowa, Canada, Tech. Note, DREO-TN-89-12, May, 1989.

[98] R. A. W. Watt and J. F. Herd, "An instantaneous direct-reading radiogoniometer," *Journal of the Institution of Electrical Engineers*, vol. 64, no. 353, pp. 611-617, 1926.

[99] M. Zakharov, "Designing a multichannel sense-and-avoid radar for small UAVs," Information and Telecommunication Technology Center (ITTC), University of Kansas, Kansas, USA, Tech. Report, ITTC-FY2014-TR-70093-02, Feb., 2014.

[100] Ettus Research, "*USRP B210 (Board Only)*" [online]. Available: http://www.ettus.com/content/files/b200-b210_spec_sheet.pdf [May 15, 2015].

[101] C. A. Balanis, *Antenna Theory: Analysis and Design*, 2nd ed., Hoboken, NJ: Wiley, 2005, ch. 2.

[102] Federal Communication Commission, *Application For an FM Broadcast Station License*,Washington D.C., Approved by OMB 3060-0506.

[103] Federal Communications Commission, *In the Matter of Amendment of Section 75.316(a) of the Commission's Rules*, Washington D.C., FCC 93-306, June 21, 1993.

[104] *www.http://zipsignal.v-soft.com*, retrieved on May 10, 2015.

[105] Linx Technologies, "*Ant-1.4-CW-HWR-SMA*" [online]. Available: http://www.linxtechnologies.com/resources/data-guides/ant-1.4-cw-hwr.pdf [May 10, 2015].

[106] Keysight Technologies, "*DSO-X 3024A Oscilloscope*" [online]. Available: http://www.keysight.com/en/pd-1946679-pn-DSOX3024A/oscilloscope-200-mhz-4-channels?cc=USlc=eng [May 10, 2015].

[107] Mini Circuits, "*Co-axial Power Splitter/Combiner*" [online]. Available: http://www.minicircuits.com/pdfs/ZX10-2-12+.pdf[May 16, 2015].

[108] G. Godby, "Using GNU radio for signal phase measurement," College of Engineering, Michigan State University, MI, USA, ECE 480 Senior Design, May, 2014.

[109] M. J. Paradie and J. Pernic, "Airborne VHF environment noise measurements," *1996 Tactical Communications Conference*, 1996, pp. 389-395.